# Design and Implementation of Modern Controls for Drive and Suspension of a High Speed Double Conical Bearingless Motor on a Real-Time System

**Entwurf und Implementierung von modernen Regelungen für Antrieb und Lagerung von einem hochtouringen doppelkonischen lagerlosen Motor auf einem Echtzeitsystem**
Master-Thesis of Panagiotis Mouratidis
April 2014

TECHNISCHE
UNIVERSITÄT
DARMSTADT

Institut für
Elektrische
Energiewandlung

Panagiotis Mouratidis

| | |
|---|---|
| Matrikelnummer: | 1604201 |
| Studiengang: | Elektrotechnik und Informationstechnik |
| Studienrichtung: | Electrical Power Engineering |
| Master-Thesis 19: | Design and Implementation of Modern Controls for Drive and Suspension of a High Speed Double Conical Bearingless Motor on a Real-Time System |
| Eingereicht: | 28. April 2014 |
| Betreuer: | M.Sc. Gael Messager<br>Prof. Dr.-Ing. habil. Dr. h.c. Andreas Binder |

Institut für Elektrische Energiewandlung
Fachbereich Elektrotechnik und Informationstechnik
Technische Universität Darmstadt
Landgraf-Georg-Str. 4
64283 Darmstadt

# Ehrenwörtliche Erklärung

Hiermit versichere ich, die vorliegende Master-Thesis ohne Hilfe Dritter nur mit den angegebenen Quellen und Hilfsmitteln angefertigt zu haben. Alle Stellen, die aus Quellen entnommen wurden, sind als solche kenntlich gemacht. Diese Arbeit hat in gleicher oder ähnlicher Form noch keiner Prüfungsbehörde vorgelegen.

Darmstadt, den 28. April 2014

(Panagiotis Mouratidis)

# Acknowledgments

This work represents the results of the six-month Master's thesis project carried out at the Institute of Electrical Energy Conversion in Darmstadt University of Technology. I am very pleased to thank all those who contributed directly or indirectly to this work.

First of all, I would like to thank the head of the institute Prof. Dr.-Ing. habil. Dr. h.c. Andreas Binder and my supervisor M.Sc. Gael Messager for giving me the opportunity to work with the very interesting subject of bearingless motors.

Especially, I would like to thank Gael Messager for introducing me to the basics of magnetic levitation and showing me the way to cope with the motor prototype on the test bench. The several discussions we had during this project certainly improved my insight and helped me overcome various difficulties. I greatly appreciate his patience and the time devoted to answer my questions as well as to edit and review this work. I hope that his support and guidance is reflected in this work.

Additionally, I would like to thank the members of the Institute workshop who were always helpful when improvements or modifications on the tench bench were needed. Their support was essential in this project.

Special thanks to my friends and colleagues in TU Darmstadt for the stimulating discussions and the friendly atmosphere throughout this time.

Last but not least, I would like to thank my family for all the support providing to me the last years. Without them, this work would not have been possible.

# Abstract

In this work, modern control approaches for drive and suspension of a high speed double conical bearingless motor are designed. Firstly, the air gap flux density and the forces acting on the rotor are analytically calculated. Subsequently, an elaborate model of the magnetically levitated rotor is developed, which considers the non-collocation of position sensors and levitation windings as well as the presence of angular motion. Three different control approaches are designed and simulated. The first approach comprises a state controller augmented with integral action, with which the closed loop dynamics are freely defined after pole placement. The other two approaches concern Linear Quadratic Gaussian and Model Predictive control. The pole placement control approach is tested successfully on the test bench with the real motor. Sinusoidal disturbance forces, with the rotational frequency, can cause large rotor orbits and may drive the inverters to their limits. For this reason, two synchronous filtering control strategies are developed. Using Imbalance Force Compensation, the rotor can be driven with low orbits at relatively low speed and using Imbalance Force Rejection, the rotor can be driven with low levitation currents at high speed. The control performance is evaluated by measurements and the measured frequency response of the closed loop system is presented.

# Kurzfassung

In dieser Arbeit wird der Entwurf von modernen Regelungen für Antrieb und Lagerung von einem hochtourigen doppelkonischen lagerlosen Motor besprochen. Zunächst werden die Luftspaltflussdichte und die auf den Rotor wirkenden Kräfte analytisch berechnet und anschließend wird ein ausführliches Modell des magnetisch schwebenden Läufers entwickelt, das die Positionsunterschiede von Lagesensoren und Schwebewicklungen, sowie die Existenz von Winkelbewegungen enthält. Anhand dieses Modells werden drei unterschiedliche Regelungen ausgelegt und simuliert. Der erste Ansatz umfasst einen mit Integralanteil erweiterten Zustandsregler, mit dem die Dynamik des geschlossenen Regelkreises frei nach Polvorgabe bestimmt wird. Die anderen Ansätze sind lineare-quadratische Gaußsche und modellbasierte prädiktive Regelungen. Die Regelung durch Polvorgabe wird erfolgreich auf dem Prüfstand am echten Motor getestet. Sinusförmige Störkräfte mit der Drehfrequenz können große Rotorumlaufbahnen verursachen und die Wechselrichter an ihre Grenzen treiben. Aus diesem Grund werden zwei Regelstrategien mit synchroner Filterung entwickelt. Bei niedriger Geschwindigkeit wird der Rotor durch Unwuchtkraftkompensation mit kleinen Exzentrizitäten angetrieben, und bei hohen Drehzahlen wird er durch Unwuchtkraftunterdrückung mit niedrigen Schwebeströmen angetrieben. Die Leistungsfähigkeit des Reglers wird durch Messungen ausgewertet, und die gemessene Frequenzantwort des geschlossenen Regelkreises wird dargestellt.

# Contents

**Glossary** **xvi**

**1. Introduction** **1**
- 1.1. Motivation for Modern Control . . . 1
- 1.2. Double Conical Bearingless Motor Prototype . . . 2

**2. Motor Mathematical Model** **5**
- 2.1. Air Gap Field Calculation . . . 5
- 2.2. Forces Acting on the Rotor . . . 7
- 2.3. Linearization at the Operating Point . . . 12
- 2.4. Model of the Magnetically Levitated Rotor . . . 14

**3. Control Design** **19**
- 3.1. Pole Placement . . . 19
- 3.2. State Observer . . . 26
- 3.3. Linear Quadratic Gaussian Control . . . 27
- 3.4. Model Predictive Control . . . 30
- 3.5. Imbalance Forces and Synchronous Filtering . . . 32

**4. Simulation** **37**
- 4.1. Closed Loop Control Structure . . . 37
- 4.2. Closed Loop Control Evaluation . . . 38

**5. Implementation** **41**
- 5.1. Feedback Signal Conditioning . . . 41
- 5.2. Position Sensor Calibration . . . 42
- 5.3. Control Performance . . . 43

**6. Conclusion** **51**
- 6.1. Accomplishments . . . 51
- 6.2. Future Work . . . 52

**Appendix A. Motor Parameters** **53**

**Appendix B. Matlab files** **55**
- B.1. Developed Matlab Functions . . . 55
- B.2. Matlab Scripts . . . 55
- B.3. Simulink Models . . . 56
- B.4. Measurement Data Files . . . 56

**Appendix C. Additional measurements** **57**

**Bibliography** **59**

# List of Figures

1.1. Axial cross-section of the CBM with rotor-2 [3] . . . . . . . . . . 2
1.2. Axial cross-section of rotor-1 and rotor-2 [3] . . . . . . . . . . 3
1.3. Parts of rotor-2 [3] . . . . . . . . . . 3
1.4. Manufactured rotor [3] . . . . . . . . . . 3

2.1. The levitating double conical bearingless rotor . . . . . . . . . . 14

3.1. Control design with static prefilter . . . . . . . . . . 21
3.2. Control design with integral action . . . . . . . . . . 23
3.3. Full order state observer . . . . . . . . . . 26
3.4. Control design with integral action and state observer . . . . . . . . . . 27
3.5. Linear Quadratic Gaussian Control . . . . . . . . . . 29
3.6. Basic structure of Model Predictive Control . . . . . . . . . . 31
3.7. Additional mass $m_\mathrm{e}$ causes the displacement of the rotor's center of mass by the eccentricity $e_\mathrm{r}$ and the generation of the centrifugal force $F_\mathrm{c}$ . . . . . . . . . . 32
3.8. Modulation block for synchronous filtering [26] . . . . . . . . . . 34
3.9. Synchronous notch filter . . . . . . . . . . 34
3.10. Synchronous resonator . . . . . . . . . . 35
3.11. Synchronous filtering in the closed loop . . . . . . . . . . 35

4.1. Simulation block diagram . . . . . . . . . . 37
4.2. Initial condition and disturbance response for $y_\mathrm{DE}$ and $I_{2\mathrm{d}_\mathrm{DE}}$ at zero speed . . . . . . . . . . 38
4.3. Simulated IFC application at 5000 rpm . . . . . . . . . . 39
4.4. Simulated IFR application at 9000 rpm . . . . . . . . . . 39

5.1. Overview of the control process . . . . . . . . . . 41
5.2. Closed loop system for frequency response measurement . . . . . . . . . . 43
5.3. Common mode plant frequency response on the $x$-$z$-plane $G_{\mathrm{pCx}}(j\omega)$ . . . . . . . . . . 45
5.4. Common mode closed loop frequency response on the $x$-$z$-plane $G_{\mathrm{wCx}}(j\omega)$ . . . . . . . . . . 45
5.5. Common mode sensitivity frequency response on the $x$-$z$-plane $G_{\mathrm{sCx}}(j\omega)$ . . . . . . . . . . 46
5.6. Application of IFC at 4000 rpm: **Top**: position synchronous component vanishes; **Bottom**: levitation current synchronous component decreases . . . . . . . . . . 48
5.7. Application of IFR at 6000 rpm: **Top**: position synchronous component decreases; **Bottom**: levitation current synchronous component vanishes . . . . . . . . . . 48
5.8. Measured rotor orbits at 18000 rpm under IFR: **Top**: horizontal and vertical displacement at DE; **Bottom**: horizontal and vertical displacement at NDE . . . . . . . . . . 49
5.9. Measured levitation currents at 18000 rpm under IFR: **Top**: levitation currents for the DE; **Bottom**: levitation currents for the NDE with increased $I_{2\mathrm{q}_\mathrm{NDE}}$ effort due to the noisy position sensor feedback $y_\mathrm{sNDE}$ . . . . . . . . . . 49

C.1. Differential mode plant frequency response on the $x$-$z$-plane $G_{\mathrm{pDx}}(j\omega)$ . . . . . . . . . . 57
C.2. Differential mode closed loop frequency response on the $x$-$z$-plane $G_{\mathrm{wDx}}(j\omega)$ . . . . . . . . . . 57
C.3. Differential mode sensitivity frequency response on the $x$-$z$-plane $G_{\mathrm{sDx}}(j\omega)$ . . . . . . . . . . 58

# List of Tables

2.1. Flux density amplitudes at $\hat{I}_1 = \hat{I}_2 = 10\,\mathrm{A}$ . . . . . . . . . . 7

3.1. Closed loop pole placement and the initial plant poles . . . . . . . . . . 25
3.2. Reduced order observer pole placement . . . . . . . . . . 27

A.1. Stator parameters . . . . . . . . . . 53
A.2. Levitation and driving winding parameters . . . . . . . . . . 53
A.3. Rotor parameters . . . . . . . . . . 53

# Glossary

The following list contains the most important symbols and subscripts as well as the abbreviations used in this work. The notation are in accordance with DIN EN ISO 80000-2 and DIN EN 60027-4. Additionally, the symbols will be explained the first time used in text.

## Notation

| | |
|---|---|
| $s$ | scalar |
| $\boldsymbol{b}$ | vector |
| $\boldsymbol{M}$ | matrix, tensor |
| $\boldsymbol{M}^{\mathsf{T}}$ | transpose |
| $\hat{u}$ | peak value, estimation |
| $\tilde{y}$ | prediction |
| $\bar{x}$ | arithmetic mean |
| $x, y, z$ | cartesian coordinates |
| $\rho, \varphi, z$ | cylindrical coordinates |
| $a, b, c$ | three-phase system labels |
| $\mathrm{diag}()$ | diagonal matrix |

## Symbols

| | | |
|---|---|---|
| $B$ | Magnetic flux density | T |
| $d$ | Diameter | m |
| $E$ | Electric field strength | $\mathrm{V\,m^{-1}}$ |
| $f$ | Frequency | Hz |
| $F$ | Force | N |
| $g$ | Gravitational acceleration | $\mathrm{m\,s^{-2}}$ |
| $h$ | Height | m |
| $h_{\mathrm{M}}$ | PM Height | m |
| $H$ | Magnetic field strength | $\mathrm{A\,m^{-1}}$ |
| $I$ | Current | A |
| $J$ | Moment of inertia | $\mathrm{kg\,m^2}$ |
| $k$ | Coefficient | |
| $k_{\mathrm{w}}$ | Winding factor | - |
| $l$ | Length | m |
| $m$ | Number of phases | - |
| $m$ | Mass | kg |
| $M$ | Torque | N m |
| $n$ | Speed | rpm |
| $N$ | Number of turns per phase | - |
| $p$ | Number of pole pairs | - |
| $q$ | Number of slots per pole and phase | - |
| $r$ | Radius | m |

| | | |
|---|---|---|
| $r_{\mathrm{si}}$ | Stator inner radius | m |
| $S$ | Surface | $\mathrm{m}^2$ |
| $t$ | Time | s |
| $T$ | Period; Time constant | s |
| $U$ | Voltage | V |
| $v$ | Velocity | $\mathrm{m\,s^{-1}}$ |
| $\alpha$ | Rotor mechanical angle | rad |
| $\gamma$ | Cone angle | rad |
| $\delta$ | Air gap | m |
| $\delta_0$ | Mechanical air gap | m |
| $\delta_{\mathrm{e}}$ | Effective air gap | m |
| $\epsilon_0$ | Permittivity of free space | $\mathrm{A\,s\,V^{-1}\,m^{-1}}$ |
| $\mu_0$ | Permeability of free space | $\mathrm{V\,s\,A^{-1}\,m^{-1}}$ |
| $\mu_{\mathrm{r}}$ | Relative permeability | - |
| $\sigma$ | Standard deviation | |
| $\varphi$ | Phase angle | rad |
| $\omega$ | Angular speed | $\mathrm{rad\,s^{-1}}$ |

## Subscripts

| | |
|---|---|
| 0 | related to rotor |
| 1 | related to driving winding |
| 2 | related to levitation winding |
| a | augmented |
| B | bandage |
| C | common mode |
| CB | coercivity for zero magnetic flux density |
| d | direct component; discrete |
| D | differential mode |
| DE | drive end |
| e | effective; estimator |
| f | force |
| Fe | iron |
| i | current; inner; integral |
| max | maximum |
| min | minimum |
| M | magnet; torque |
| n | normal component |
| NDE | non drive end |
| o | outer |
| q | quadrature component |
| r | rotor; radial component |
| R | remanence |
| s | stator; stiffness; sensor; sampling |
| t | tangential component |
| z | axial component |
| w | winding |
| $\delta$ | air gap |

## Acronyms

| | |
|---|---|
| **AMB** | Active Magnetic Bearing |
| **CARE** | Continuous-time Algebraic Riccati Equation |
| **CBM** | Conical Bearingless Motor |
| **DE** | Drive End |
| **DARE** | Discrete-time Algebraic Riccati Equation |
| **FFT** | Fast Fourier Transform |
| **FMS** | Full Modal Synthesis |
| **FOC** | Field Oriented Control |
| **FPGA** | Field Programmable Gate Array |
| **IFC** | Imbalance Force Compensation |
| **IFR** | Imbalance Force Rejection |
| **IIR** | Infinite Impulse Response |
| **LAN** | Local Area Network |
| **LTI** | Linear Time Invariant |
| **LQE** | Linear Quadratic Estimator |
| **LQG** | Linear Quadratic Gaussian |
| **LQR** | Linear Quadratic Regulator |
| **MIMO** | Multiple Input Multiple Output |
| **MPC** | Model Predictive Control |
| **NDE** | Non Drive End |
| **OP** | Operating Point |
| **PCI** | Peripheral Component Interconnect |
| **PI** | Proportional Integral |
| **PID** | Proportional Integral Derivative |
| **PM** | Permanent Magnet |
| **PMSM** | Permanent Magnet Synchronous Motor |
| **QP** | Quadratic Programming |
| **RTAI** | Real Time Application Interface |
| **SISO** | Single Input Single Output |
| **ZOH** | Zero Order Hold |

# 1 Introduction

The double conical bearingless high-speed permanent magnet motor, from now on *Conical Bearingless Motor* (CBM), is a prototype designed and manufactured in the Institute of Electrical Energy Conversion of Darmstadt University of Technology. The term bearingless denotes that the machine is not suspended by mechanical or magnetic bearings. Although the machine has additional windings for the rotor suspension, these lie on the same stator region as the driving windings. This design is advantageous because it reduces the needed machine length in comparison with *Active Magnetic Bearings* (AMBs). Although the CBM is not a typical AMB system, the basic principles of AMB are also applied here. An introduction to the AMB technology with recommendations for basic and advanced control structures is given in [1]. Another work more relevant to the bearingless motors is available in [2].

The machine design, manufacture, and commissioning is explained in [3]. Additionally, an introduction to the principles of the bearingless drives is also given in [3]. However, the control implemented in this first work was based in a system that was not flexible to modifications. A system based on the Linux *Real Time Application Interface* (RTAI), which gives more opportunities for rapid control prototyping was implemented in [4]. The current control loop for the CBM is implemented using *Proportional Integral* (PI) controllers within a *Field Programmable Gate Array* (FPGA) [4]. The underlying current control loop is designed to be much faster than the mechanical dynamics, so that the CBM including the inverters can be considered as a current-controlled system. This simplifies the design of the motion controller.

An improved motion control structure is however still needed. For *Multiple Input Multiple Output* (MIMO) systems, as the CBM, a control based on a state space representation is a more appropriate approach. In this work, three different control methods using a state space model of the CBM are designed and simulated in Matlab-Simulink. The first approach is based on pole placement, the second on *Linear Quadratic Gaussian* (LQG) and the third on *Model Predictive Control* (MPC). The pole placement control approach will be finally implemented and tested on the real motor.

## 1.1 Motivation for Modern Control

The term modern control refers to control design methods that appeared later in time than the so called classical control. An example of classical control approach is the use of the root locus to select the gains of a *Proportional Integral Derivative* (PID) controller. Optimal control and predictive control are examples of modern control approaches. However, the term modern does not imply that these methods are emerging or better than the classical control methods. Generally, certain control methods are better suited for certain applications.

All the control approaches handled in this work are based on a state space representation of the CBM. An introduction to the state space control design is given in [5]. The main advantage of the state space control is that, not only the system input-output, but also the inner system states are taken into account. A state feedback controller provides more design freedom than an output feedback controller, since the inner state information is missing from the latter. Furthermore, controllers for MIMO systems can be designed more conveniently in state space. The CBM is a MIMO system with cross couplings between its inputs-outputs. Systematic approaches to decouple MIMO systems in state space are given in [6, 7].

## 1.2 Double Conical Bearingless Motor Prototype

The CBM equipped with the second rotor prototype is displayed in Figure 1.1. Both rotor prototypes can be seen in Figure 1.2. The rotor-1 has a conical back iron and thus a lower *Permanent Magnet* (PM) height, whereas rotor-2 has a cylindrical back iron and consequently, a higher PM height. The components of rotor-2 can be seen in Figure 1.3. The rotor is composed by a rigid steel shaft, conical PMs and measurement surfaces for the position sensors. The carbon fiber bandages ensure that the PMs, which are glued on the rotor steel shaft, can sustain the centrifugal forces applied at high angular speeds. The measurement surfaces are used as targets for the eddy current position sensors, which are mounted on the stator. The manufactured rotor can be observed in Figure 1.4.

The mounting of the PMs to the rotor back iron is an important construction issue. An eccentric mounting leads to an unsymmetrical PM field and therefore to a rotating single sided magnetic pull, trying to displace the rotor from the stator bore center. This phenomenon was explained in [3] and it was assessed that the rotor-2 PMs were eccentric mounted due to difficulties on the gluing process. The latter was also verified by measurements and comparison with the performance of rotor-1.

In this work, only rotor-2 is tested; the idea is that rotor-2 is more challenging for testing because of its aforementioned deficiency . A control strategy that works satisfactorily for rotor-2 will be applied easier to rotor-1. The CBM design parameters for both rotors are presented in Appendix A. Furthermore, the design parameters are registered for each rotor in the Matlab scripts `motor1` and `motor2` (Appendix B).

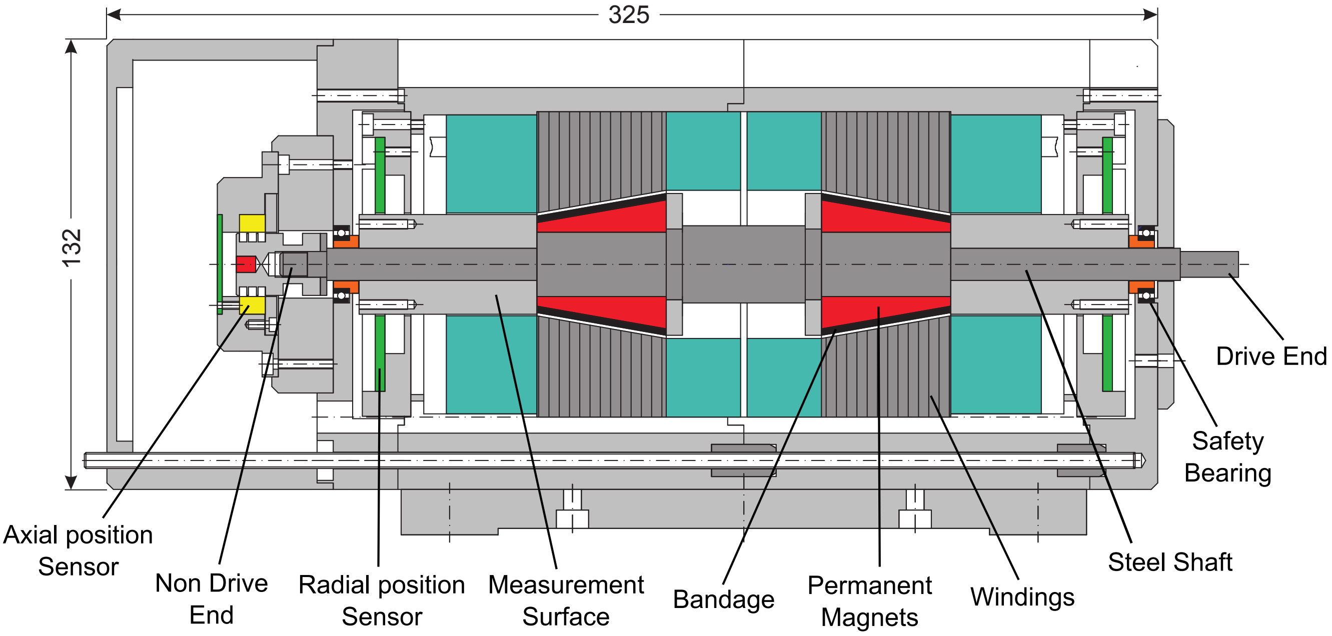

**Figure 1.1.:** Axial cross-section of the CBM with rotor-2 [3]

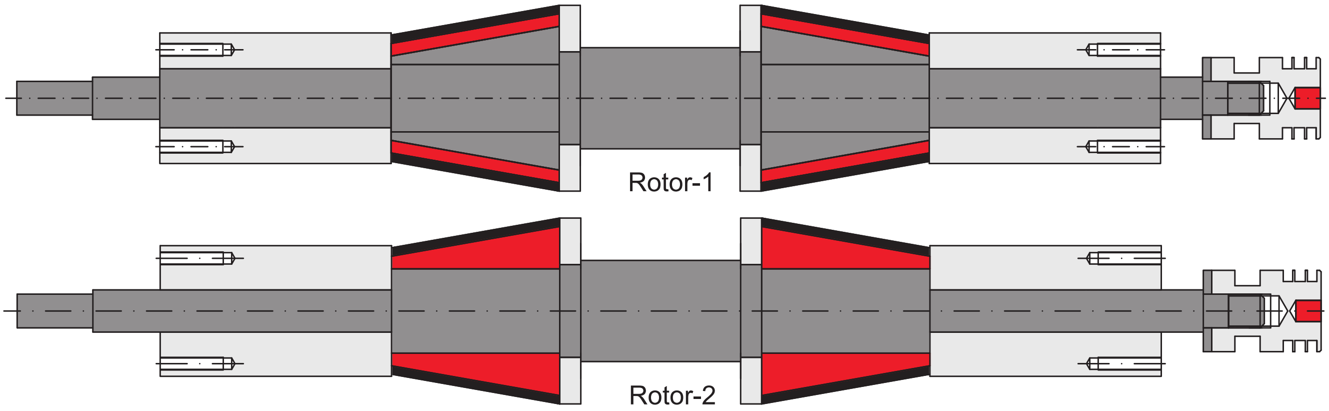
Rotor-1
Rotor-2

**Figure 1.2.:** Axial cross-section of rotor-1 and rotor-2 [3]

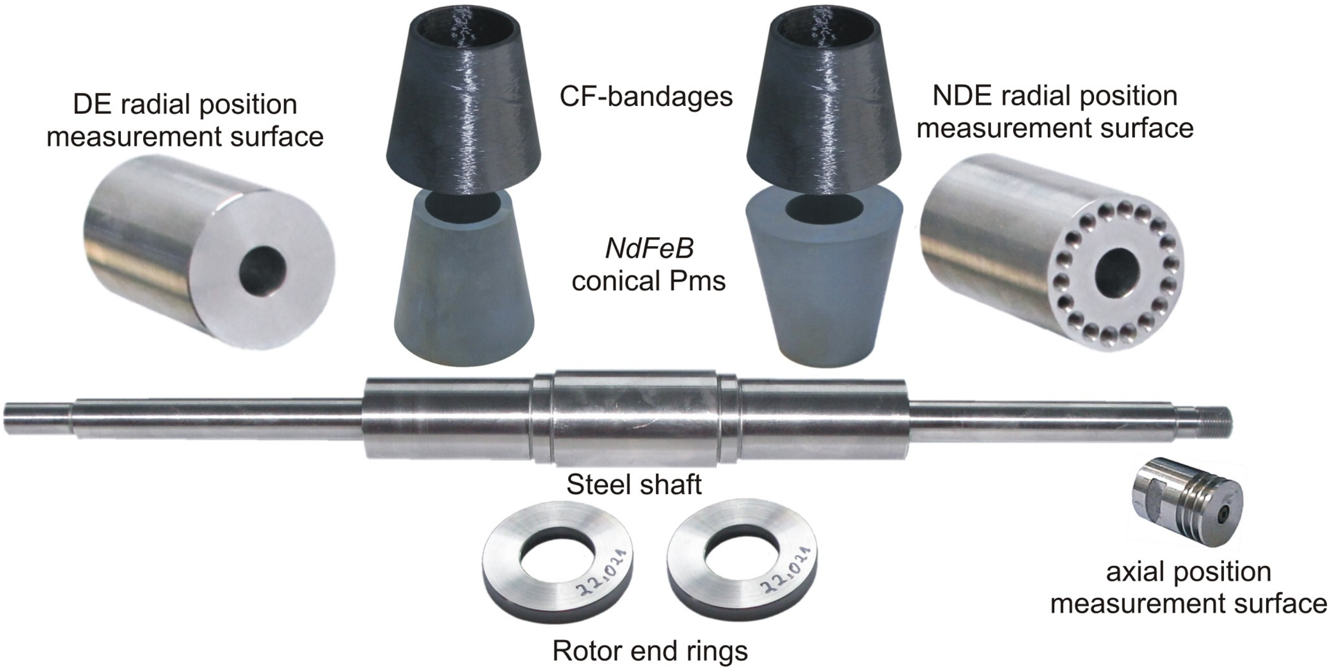
DE radial position measurement surface
CF-bandages
NDE radial position measurement surface
*NdFeB* conical Pms
Steel shaft
axial position measurement surface
Rotor end rings

**Figure 1.3.:** Parts of rotor-2 [3]

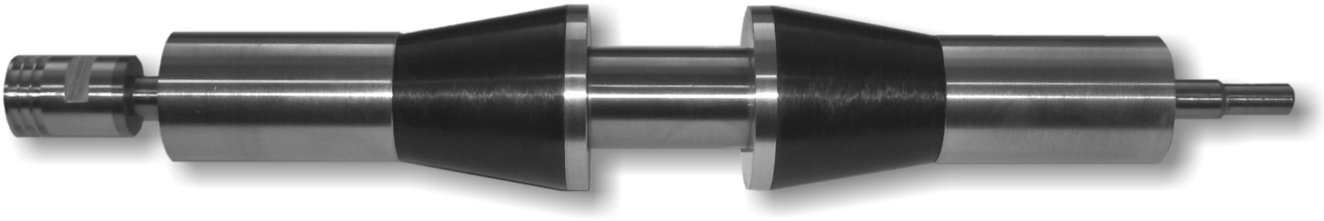

**Figure 1.4.:** Manufactured rotor [3]

# 2 Motor Mathematical Model

In this chapter, the mathematical model of the motor is derived. Mathematical models of the CBM are already presented in [3, 4]. In [3] a detailed analytical calculation of the magnetic fields is presented, whereas in [4] the influence of the axial displacement to the other axes of the CBM is considered. In the present work, a primitive motor model with simplified magnetic field equations is presented. The present modeling aims to give a better understanding of the parameters influencing the force generation and provide a satisfactory model for the control design. An accurate calculation of the force coefficients is out of the scope of this work, this can be later done using parameter identification techniques. Due to the inherent instability of the bearingless motor levitation, a closed-loop controller should be firstly designed and implemented before parameter identification is applied.

The aim of the modeling is to find out the motion equations that govern the rotor levitation and rotation. To derive the motion equations, the air gap magnetic fields are firstly derived and then the forces acting on the rotor are calculated.

## 2.1 Air Gap Field Calculation

Three different sources generate magnetic fields in the air gap; the driving winding, the levitation winding and the rotor PMs. The rotor PMs have conical shape and are parallel magnetized [3], so that a sinusoidal magnetic field along the rotor mechanical angle $\alpha$ is produced. For a low saturated *Permanent Magnet Synchronous Motor* (PMSM), the flux lines in the air gap are almost perpendicular to the stator bore [3]. Therefore, to simplify the motor model, only the PM field which is normal to the stator conical surface is further considered. Considering a perfect sinusoidal PM field distribution with flux density amplitude $\hat{B}_{0n}$, electrical frequency $\omega_0$ and $p_0$ pole pairs, the flux density of the rotating PM field can be expressed by (2.1).

$$B_{0n}(\alpha, t) = \hat{B}_{0n} \cos(p_0\alpha - \omega_0 t - \varphi_0) \tag{2.1}$$

The amplitude of the PM flux density can be approximated by (2.2), similar to the PMSM case presented in [8], where $B_\mathrm{R}$ is the remanence magnetic flux density, $\mu_\mathrm{rM}$ the relative permeability and $h_\mathrm{M}$ the height of the PMs. Furthermore, $h_\mathrm{B}$ denotes the height of the bandage attached on the PMs and $\delta_0$ the nominal mechanical air gap.

$$\hat{B}_{0n} = \frac{B_\mathrm{R}}{1 + \frac{\mu_\mathrm{rM}}{h_\mathrm{M}}(h_\mathrm{B} + \delta_0)} \tag{2.2}$$

Two rotor prototypes are manufactured for the CBM, (see Section 1.2). The first rotor has a conical back iron, while the second rotor has a cylindrical one. The height of the PMs of rotor-1 is constant, while that of rotor-2 is variable depending on the axial position. For this reason, the mean value of the PM height along the $z$-axis (2.3) will be used in equation (2.2).

$$\bar{h}_\mathrm{M} = \frac{1}{l_\mathrm{Fe}} \int_0^{l_\mathrm{Fe}} h_\mathrm{M}(z)\,\mathrm{d}z \tag{2.3}$$

The mean PM height can be calculated for both rotors using (2.4), where $h_{\mathrm{M}\min}$ is the minimum magnet height, $\gamma_{\mathrm{r_M}}$ the rotor PM cone angle and $\gamma_{\mathrm{r_{Fe}}}$ the rotor back iron cone angle.

$$\bar{h}_{\mathrm{M}} = \frac{1}{l_{\mathrm{Fe}}} \int_0^{l_{\mathrm{Fe}}} \left[h_{\mathrm{M\,min}} + z\tan\left(\gamma_{\mathrm{r_M}} - \gamma_{\mathrm{r_{Fe}}}\right)\right] \mathrm{d}z = h_{\mathrm{M\,min}} + \frac{1}{2} l_{\mathrm{Fe}} \tan\left(\gamma_{\mathrm{r_M}} - \gamma_{\mathrm{r_{Fe}}}\right) \tag{2.4}$$

The currents flowing in the stator windings will also generate magnetic fields. A two dimensional approach is used for the calculation of the stator fields, i.e. the stator fields are composed by a tangential and a normal to the stator surface component. The tangential field is defined so that it has 90° phase lead from the normal field. The number of pole pairs is $p_1$ for the driving and $p_2$ for the levitation winding. Considering a perfect sinusoidal spatial distribution of the stator windings and balanced sinusoidal current injection over time with equal amplitude for each phase, the flux densities of the stator rotating fields can be expressed by (2.5).

$$\begin{aligned}
B_{1n}(\alpha,t) &= \hat{B}_{1n}\cos(p_1\alpha - \omega_1 t - \varphi_1) \\
B_{1t}(\alpha,t) &= \hat{B}_{1t}\cos(p_1\alpha - \omega_1 t + \frac{\pi}{2} - \varphi_1) \\
B_{2n}(\alpha,t) &= \hat{B}_{2n}\cos(p_2\alpha - \omega_2 t - \varphi_2) \\
B_{2t}(\alpha,t) &= \hat{B}_{2t}\cos(p_2\alpha - \omega_2 t + \frac{\pi}{2} - \varphi_2)
\end{aligned} \tag{2.5}$$

The flux density amplitudes are given in (2.6), where $m$ is the number of phases, $N_{\mathrm{s}}$ the number of turns per phase, $k_{\mathrm{w}}$ the winding factor, $p$ the number of pole pairs, $\delta_{\mathrm{e}}$ the effective air gap, $\bar{r}_{\mathrm{si}}$ the mean stator inner radius and $\hat{I}$ the current amplitude [8]. The flux density amplitudes can be expressed by a coefficient $k_{\mathrm{B}}$ in T/A times the current amplitude (2.6).

$$\begin{aligned}
\hat{B}_{1n} &= \frac{\mu_0 m_1 N_{\mathrm{s1}} k_{\mathrm{w1}} \hat{I}_1}{\delta_{\mathrm{e}} \pi p_1} = k_{\mathrm{B1n}} \hat{I}_1 \\
\hat{B}_{1t} &= \frac{\mu_0 m_1 N_{\mathrm{s1}} k_{\mathrm{w1}} \hat{I}_1}{\pi \bar{r}_{\mathrm{si}}} = k_{\mathrm{B1t}} \hat{I}_1 \\
\hat{B}_{2n} &= \frac{\mu_0 m_2 N_{\mathrm{s2}} k_{\mathrm{w2}} \hat{I}_2}{\delta_{\mathrm{e}} \pi p_2} = k_{\mathrm{B2n}} \hat{I}_2 \\
\hat{B}_{2t} &= \frac{\mu_0 m_2 N_{\mathrm{s2}} k_{\mathrm{w2}} \hat{I}_2}{\pi \bar{r}_{\mathrm{si}}} = k_{\mathrm{B2t}} \hat{I}_2
\end{aligned} \tag{2.6}$$

The mean stator inner radius is given in (2.7), where $l_{\mathrm{Fe}}$ is the iron length of the stator cone, $r_{\mathrm{si\,min}}$ the minimum radius of the stator bore and $\gamma_{\mathrm{s}}$ the stator cone angle.

$$\bar{r}_{\mathrm{si}} = \frac{1}{l_{\mathrm{Fe}}} \int_0^{l_{\mathrm{Fe}}} r_{\mathrm{si}}(z)\,\mathrm{d}z = \frac{1}{l_{\mathrm{Fe}}} \int_0^{l_{\mathrm{Fe}}} (r_{\mathrm{si\,min}} + z\tan\gamma_{\mathrm{s}})\,\mathrm{d}z = r_{\mathrm{si\,min}} + \frac{1}{2} l_{\mathrm{Fe}} \tan\gamma_{\mathrm{s}} \tag{2.7}$$

Since the permeability of the PM and the bandage are close to the vacuum permeability, the effective air gap is defined as the sum of the mechanical air gap, the rotor bandage height and the mean PM height (2.8).

$$\delta_{\mathrm{e}} = \delta_0 + h_{\mathrm{B}} + \bar{h}_{\mathrm{M}} \tag{2.8}$$

The winding factor of the fundamental is given in (2.9), where $q$ is the number of slots per pole and phase [8].

$$k_{\mathrm{w}} = \frac{\sin(\frac{\pi}{2m})}{q\sin(\frac{\pi}{2mq})} \tag{2.9}$$

Following the law of superposition, the air gap flux density can be expressed as the sum of flux densities on each coordinate (2.10).

$$\begin{aligned} B_{\delta n}(\alpha,t) &= B_{0n}(\alpha,t)+B_{1n}(\alpha,t)+B_{2n}(\alpha,t) \\ B_{\delta t}(\alpha,t) &= B_{1t}(\alpha,t)+B_{2t}(\alpha,t) \end{aligned} \tag{2.10}$$

Considering a common cone angle for the rotor and stator, i.e. $\gamma = \gamma_{\mathrm{s}} = \gamma_{\mathrm{r_M}}$, the air gap field can be transformed in cylindrical coordinates (2.11).

$$\boldsymbol{B}_{\delta}(\alpha,t) = B_{\delta n}(\alpha,t)\cos\gamma\boldsymbol{e}_{\rho} + B_{\delta t}(\alpha,t)\boldsymbol{e}_{\varphi} + B_{\delta n}(\alpha,t)\sin\gamma\boldsymbol{e}_{z} \tag{2.11}$$

Estimating the flux density magnitudes is helpful in order to simplify the motor model in the next steps. Taking the levitation and driving currents close to their maximum values, i.e. $\hat{I}_1 = \hat{I}_2 = 10\,\mathrm{A}$, and using the motor parameters given in Appendix B, the flux density amplitudes are calculated and presented in Table 2.1. The PM flux density is calculated with the values of $B_{\mathrm{R}}$ and $H_{\mathrm{CB}}$ obtained after linear interpolation for a temperature of 70 °C using the data of Table A.3.

**Table 2.1.:** Flux density amplitudes at $\hat{I}_1 = \hat{I}_2 = 10\,\mathrm{A}$

| **Flux Density** | **Amplitude / T** | |
|---|---|---|
| | Rotor-1 | Rotor-2 |
| $B_{0n}$ | 0.549 | 0.758 |
| $B_{1n}$ | 0.058 | 0.037 |
| $B_{1t}$ | 0.018 | 0.018 |
| $B_{2n}$ | 0.020 | 0.013 |
| $B_{2t}$ | 0.012 | 0.012 |

It can be observed in Table 2.1 that rotor-1 has a lower PM flux density due to the shorter PM height, but higher winding flux densities due to the shorter effective air gap. The tangential flux densities are the same for both rotors as they are independent of the PM height. Furthermore, the PM flux density even in the worst case of rotor-1 is about 10 times higher than the normal component of the driving winding flux density and 30 times higher than the tangential. Consequently, it can be assumed that the PM field dominates in the air gap, creating an air gap field that is almost perpendicular to the stator surface.

According to [2], if the PM height equals the length of the mechanical air gap, the radial force generation on the rotor is optimized. Looking at the rotor-1 design parameters in Table A.3, considering an extended air gap that includes the fiber bandage height, it becomes obvious that the optimization criterion is fulfilled. However, according to equation (2.2), it turns that a relative big air gap with respect to the PM height, leads to a reduced air gap magnetic flux density. If the optimization criterion is fulfilled, i.e. $h_{\mathrm{M}} = h_{\mathrm{B}} + \delta_0$, it follows that $\hat{B}_{0n} \approx 0.5 B_{\mathrm{R}}$. That is, only half of the PMs remanence magnetization is exploited in the air gap field.

## 2.2 Forces Acting on the Rotor

Starting with the Lorentz force law (2.12) for a point charge moving with velocity $v$ inside an Electromagnetic field, the convenient form of (2.13) can be derived, where $\boldsymbol{f}$ is the *force per volume*, $\boldsymbol{S}$ the *Poynting vector* and $\boldsymbol{T}$ the so called *Maxwell stress tensor* [9]. That is, the divergence of the Maxwell stress tensor gives the force per unit volume plus a term containing the Poynting vector $\boldsymbol{S}$.

$$\boldsymbol{F} = q(\boldsymbol{E} + v \times \boldsymbol{B}) \tag{2.12}$$

$$f = \nabla \cdot \boldsymbol{T} - \epsilon_0 \mu_0 \frac{\partial \boldsymbol{S}}{\partial t} \tag{2.13}$$

Using the divergence theorem and considering that in the static case the Poynting vector is independent of time, equation (2.14) is derived, where $\boldsymbol{F}$ denotes the force applied on the charges surrounded by the closed surface $S$.

$$\boldsymbol{F} = \oint_S \boldsymbol{T} \cdot \mathrm{d}\boldsymbol{S} \tag{2.14}$$

The components of the Maxwell stress tensor are given in (2.15) without proof. The analytical derivation can be found in [9].

$$T_{ij} = \epsilon_0 (E_i E_j - \frac{1}{2}\delta_{ij} E^2) + \frac{1}{\mu_0}(B_i B_j - \frac{1}{2}\delta_{ij} B^2) \tag{2.15}$$

The indices $i, j$ correspond to the chosen coordinates, e.g. $x, y, z$ for Cartesian or $\rho, \varphi, z$ for cylindrical coordinates. The *Kronecker delta* $\delta_{ij}$ equals unity if the indices are same and zero if the indices are different. Therefore, for the three dimensional space the stress tensor has all together nine components. Physically, the components of the Maxwell stress tensor represent force per unit area, the so called *stress*. That is, $T_{ij}$ is the stress in the $i$th dimension applied on a surface element oriented in the $j$th dimension. The diagonal elements (e.g. $T_{xx}, T_{yy}, T_{zz}$ for Cartesian coordinates) are normal stresses, and the off-diagonal elements (e.g $T_{xy}, T_{xz}$) are *shears*.

In case of electric machinery the electrostatic forces are negligible compared to the magnetostatic forces, so that only the second summand of (2.15) is further considered. Moreover, the cylindrical coordinates are advantageous for the study of electric machinery, therefore, the Maxwell stress tensor is conveniently expressed in cylindrical coordinates by (2.16).

$$\boldsymbol{T} = \frac{1}{2\mu_0} \begin{pmatrix} B_\rho^2 - B_\varphi^2 - B_z^2 & 2B_\rho B_\varphi & 2B_\rho B_z \\ 2B_\rho B_\varphi & B_\varphi^2 - B_\rho^2 - B_z^2 & 2B_\varphi B_z \\ 2B_\rho B_z & 2B_\varphi B_z & B_z^2 - B_\rho^2 - B_\varphi^2 \end{pmatrix} \tag{2.16}$$

The vector normal to the conical surface $\boldsymbol{n}$ is expressed in cylindrical coordinates by (2.17). According to Cauchy's stress theorem [10], the *stress vector* $\boldsymbol{t}$ on a surface element $\mathrm{d}S$ with normal $\boldsymbol{n}$ is related with the stress tensor by (2.18).

$$\boldsymbol{n} = \cos\gamma \boldsymbol{e}_\rho + 0\boldsymbol{e}_\varphi + \sin\gamma \boldsymbol{e}_z \tag{2.17}$$

$$\boldsymbol{t} = \boldsymbol{T} \cdot \boldsymbol{n} \tag{2.18}$$

Placing the air gap field components calculated in (2.11) in the stress tensor and then applying (2.18) on the conical surface with normal $\boldsymbol{n}$, the stress vector $\boldsymbol{t}$ (2.19) is calculated.

$$\boldsymbol{t} = \frac{1}{2\mu_0}\left[\left(B_{\delta n}^2 - B_{\delta t}^2\right)\cos\gamma \boldsymbol{e}_\rho + 2B_{\delta n} B_{\delta t} \boldsymbol{e}_\varphi + \left(B_{\delta n}^2 - B_{\delta t}^2\right)\sin\gamma \boldsymbol{e}_z\right] \tag{2.19}$$

The tangential component of the air gap field is much lower than the normal one (see Table 2.1), hence ${B_\delta}_n^2 \gg {B_\delta}_t^2$ holds. Consequently, the stress vector is simplified to equation (2.20).

$$\boldsymbol{t} = \frac{1}{2\mu_0}\left[B_{\delta n}^2 \cos\gamma \boldsymbol{e}_\rho + 2B_{\delta n}B_{\delta t}\boldsymbol{e}_\varphi + B_{\delta n}^2 \sin\gamma \boldsymbol{e}_z\right] \tag{2.20}$$

In order to calculate the forces applied to the rotor, the closed surface where the integration of (2.14) takes place should be first selected. Any surface that encloses the rotor cone inside the air gap can be selected for this purpose. However, the stator surface is selected because the calculated magnetic fields are more accurate near that place. For example, the PM flux lines penetrate perpendicular to the stator surface, which is in accordance with the simplification done that the PM field contains only a normal component. The top and bottom sides of the rotor cone are not penetrated by flux lines and therefore neglected from the integration.

The metric coefficient for the differential cone length along the $z$-axis is $h_z = 1/\cos\gamma$. Since the stator cone radius is not constant along the $z$-axis, the differential conical surface is expressed by (2.21).

$$\mathrm{d}\boldsymbol{S} = \frac{r_{\mathrm{si}}(z)}{\cos\gamma}\,\mathrm{d}\varphi\,\mathrm{d}z\boldsymbol{n} \tag{2.21}$$

Integrating along the stator iron stack and using the mean stator radius defined in (2.7), the stator conical surface is calculated in (2.22).

$$S_{\mathrm{s}} = \int_0^{2\pi}\int_0^{l_{\mathrm{Fe}}} \frac{r_{\mathrm{si}}(z)}{\cos\gamma}\,\mathrm{d}\varphi\,\mathrm{d}z = 2\pi\bar{r}_{\mathrm{si}}\frac{l_{\mathrm{Fe}}}{\cos\gamma} \tag{2.22}$$

Integrating the tangential component of the stress vector over the stator surface, the tangential force $F_\varphi$ acting on the rotor cone is calculated in (2.23).

$$F_\varphi = \frac{1}{\mu_0}\oint_S B_{\delta n}B_{\delta t}\,\mathrm{d}S \tag{2.23}$$

From now on, a common electrical frequency is considered for all the air gap fields, i.e. the synchronous frequency $\omega_{\mathrm{s}} = \omega_0 = \omega_1 = \omega_2$. The latter simplifies the force calculations. Moreover, it is noticed that the driving winding and the rotor have the same number of pole pairs, i.e. $p_0 = p_1 = 1$, whereas the levitation winding has $p_2 = 2$. Considering that only the tangential component of the driving winding with the PM field generates tangential forces, the relationship (2.24) is derived. The other field pairs coming from the product $B_{\delta n}B_{\delta t}$ do not generate any tangential force because they have different number of pole pairs.

$$F_\varphi = \frac{1}{2\mu_0}S_{\mathrm{s}}\hat{B}_{0n}\hat{B}_{1t}\sin(\varphi_1 - \varphi_0) \tag{2.24}$$

The electromagnetic torque can be then approximated by (2.25), assuming that the tangential force acts on the mean radius of the stator bore.

$$M = F_\varphi \bar{r}_{\mathrm{si}} \tag{2.25}$$

Driving the motor with the principle of *Field Oriented Control* (FOC), it becomes possible to control the current amplitude $\hat{I}_1$ and the phase angle $(\varphi_1 - \varphi_0)$. Having as goal to yield maximum torque with minimum losses, the normal of the driving field should be oriented so that it has 90° phase shift from the PM field. The current giving a stator field perpendicular to the rotor field and so parallel to the rotor $q$-axis is named $q$-current, while the current giving a field parallel to the rotor $d$-axis is named $d$-current.

The relationships of the $dq$-currents are presented in (2.26), where $\hat{I}$ is the current amplitude and $\varphi$ the phase angle between the stator and rotor flux densities.

$$\begin{aligned} I_{\mathrm{d}} &= \hat{I}\cos\varphi \\ I_{\mathrm{q}} &= \hat{I}\sin\varphi \end{aligned} \tag{2.26}$$

Defining the torque-current coefficient $k_{\mathrm{M}}$ in Nm/A (2.27), the torque is expressed as a linear function of the $q$-current (2.28). It has to be noted that the torque calculated in (2.28) is the result of only one conical motor; the net torque equals the sum of the torques generated by each conical motor.

$$k_{\mathrm{M}} = \frac{1}{2\mu_0} S_{\mathrm{s}} \bar{r}_{\mathrm{si}} k_{\mathrm{B1t}} \hat{B}_{0n} \tag{2.27}$$

$$M = k_{\mathrm{M}} I_{1\mathrm{q}} \tag{2.28}$$

Integrating along the $z$-axis, the axial force per cone is derived in (2.29). Expanding the square $B^2_{\delta n}$, it is noticed that the field product pairs having different number of pole pairs do not generate any force. After calculations the axial force can be expressed by (2.30).

$$F_z = \frac{1}{2\mu_0} \oint\limits_S B^2_{\delta n} \sin\gamma \, \mathrm{d}S \tag{2.29}$$

$$F_z = \frac{1}{2\mu_0} S_{\mathrm{s}} \sin\gamma \left[ \hat{B}^2_{0n} + \hat{B}^2_{1n} + \hat{B}^2_{2n} + 2\hat{B}_{0n}\hat{B}_{1n}\cos(\varphi_1 - \varphi_0) \right] \tag{2.30}$$

This force is applied only to one of the conical motors. The net axial force applied on the rotor equals the difference of the axial forces applied on each conical motor.

In case the rotor center lies exactly on the stator middle and the currents $I_1, I_2$ flowing in each conical motor are the same, the two axial forces are equal and cancel each other. However, the rotor has a play of about 400 µm in axial direction, which means that for small axial displacements, forces will be generated due to the different flux densities in the *Drive End* (DE) and *Non Drive End* (NDE). It is evident that the axial displacement should be controllable, otherwise the rotor will stack to the DE or NDE. The last summand of (2.30) contains the current $I_{1\mathrm{d}} = \hat{I}_1 \cos(\varphi_1 - \varphi_0)$, which is controllable by FOC. The terms $\hat{B}^2_{1n}, \hat{B}^2_{2n}$ are not linear functions of the $dq$-currents, since they depend on the square of the current amplitudes $\hat{I}_1, \hat{I}_2$. However, they take much lower values than the term $\hat{B}^2_{0n}$, as it is shown in Table 2.1. Consequently, they can be considered as disturbances and neglected for the motor modeling. Defining the force-current coefficient $k_{\mathrm{iz}}$ in (2.31), the net axial force can be expressed by (2.32)

$$k_{\mathrm{iz}} = \frac{1}{2\mu_0} S_{\mathrm{s}} \sin\gamma \, k_{\mathrm{B1n}} \hat{B}_{0n} \tag{2.31}$$

$$F_{z\mathrm{net}} = k_{\mathrm{iz}} \left( I_{1\mathrm{d}_{\mathrm{DE}}} - I_{1\mathrm{dDE}} \right) + \frac{1}{2\mu_0} S_{\mathrm{s}} \sin\gamma \left( \hat{B}^2_{0n,\mathrm{DE}} - \hat{B}^2_{0n,\mathrm{NDE}} \right) \tag{2.32}$$

The forces acting on the $x$ and $y$ axes of the Cartesian coordinate system, which is placed on the same origin as the cylindrical system used to define the Maxwell stress tensor, are of interest, because they can be controlled by FOC. The transformation to the Cartesian coordinate system is possible using the transformation matrix given in (2.33).

$$\begin{pmatrix} \boldsymbol{e}_x \\ \boldsymbol{e}_y \end{pmatrix} = \begin{pmatrix} \cos\alpha & -\sin\alpha \\ \sin\alpha & \cos\alpha \end{pmatrix} \begin{pmatrix} \boldsymbol{e}_\rho \\ \boldsymbol{e}_\varphi \end{pmatrix} \tag{2.33}$$

Then, the stress vector calculated in (2.20) can be expressed in Cartesian coordinates (2.34).

$$\boldsymbol{t} = \frac{1}{2\mu_0}[(B_{\delta n}^2 \cos\gamma \cos\alpha - 2B_{\delta n}B_{\delta t}\sin\alpha)\boldsymbol{e}_x + (B_{\delta n}^2 \cos\gamma \sin\alpha + 2B_{\delta n}B_{\delta t}\cos\alpha)\boldsymbol{e}_y + B_{\delta n}^2 \sin\gamma \boldsymbol{e}_z] \tag{2.34}$$

Integrating again over the stator surface, the forces $F_x$ and $F_y$ are derived in (2.35) and (2.36) respectively. It should be noted that the presence of $\sin\alpha$ and $\cos\alpha$ in the integrals makes only the field pairs having a pole pair difference of ±1 to generate forces. In other words, only the pairs of the levitation field with the PM field or driving field generate forces. The pole pair requirement of $p_2 = p_1 \pm 1$ is a basic design principle followed in most of the bearingless motors. More information about the influence of pole pair combinations can be found in [11].

$$F_x = \frac{S_\text{s}}{4\mu_0}[\hat{B}_{0n}(\hat{B}_{2n}\cos\gamma + \hat{B}_{2t})\cos(\varphi_2 - \varphi_0) + (\hat{B}_{1n}\hat{B}_{2n}\cos\gamma + \hat{B}_{1n}\hat{B}_{2t} - \hat{B}_{2n}\hat{B}_{1t})\cos(\varphi_2 - \varphi_1)] \tag{2.35}$$

$$F_y = \frac{S_\text{s}}{4\mu_0}[\hat{B}_{0n}(\hat{B}_{2n}\sin\gamma + \hat{B}_{2t})\cos(\varphi_2 - \varphi_0) + (\hat{B}_{1n}\hat{B}_{2n}\cos\gamma + \hat{B}_{1n}\hat{B}_{2t} - \hat{B}_{2n}\hat{B}_{1t})\sin(\varphi_2 - \varphi_1)] \tag{2.36}$$

The superposition of $F_x$ and $F_y$ creates a radial force. For this reason, $F_x$ and $F_y$ will be referred as radial forces. It can be observed in (2.35) and (2.36) that the forces contain a first part that is controllable by the currents $I_\text{2d}, I_\text{2q}$ and a second part that is not controllable by FOC. To simplify the radial force equations, the force-current coefficient $k_\text{ir}$ and the force-coupling coefficient $k_\text{r12}$ are defined in (2.37) and (2.38) respectively.

$$k_\text{ir} = \frac{S_\text{s}}{4\mu_0}(k_\text{B2n}\cos\gamma + k_\text{B2t})\hat{B}_{0n} \tag{2.37}$$

$$k_\text{r12} = \frac{S_\text{s}}{4\mu_0}(k_\text{B1n}k_\text{B2n}\cos\gamma + k_\text{B1n}k_\text{B2t} - k_\text{B2n}k_\text{B1t}) \tag{2.38}$$

The radial forces can be now expressed in dependence of the driving and levitation currents by (2.39).

$$\begin{aligned} F_x &= k_\text{ir}I_\text{2d} + k_\text{r12}I_1I_2\cos(\varphi_2 - \varphi_1) \\ F_y &= k_\text{ir}I_\text{2q} + k_\text{r12}I_1I_2\sin(\varphi_2 - \varphi_1) \end{aligned} \tag{2.39}$$

Expanding $\cos(\varphi_2 - \varphi_1)$ and $\sin(\varphi_2 - \varphi_1)$, the radial forces can be equivalently expressed using only $dq$-currents (2.40).

$$\begin{aligned} F_x &= k_\text{ir}I_\text{2d} + k_\text{r12}\left(I_\text{1d}I_\text{2d} + I_\text{1q}I_\text{2q}\right) \\ F_y &= k_\text{ir}I_\text{2q} + k_\text{r12}\left(I_\text{1q}I_\text{2d} - I_\text{1d}I_\text{2q}\right) \end{aligned} \tag{2.40}$$

Significant changes in the magnetic field distribution are caused due to the change of the mechanical air gap. If the rotor moves slightly towards one stator side, the air gap becomes smaller on that side and consequently the magnetic flux density is intensified pulling the rotor further towards it. This phenomenon is often called *negative stiffness* because it is directly opposite to the positive stiffness of a conventional suspension system, where the force opposes the displacement. The negative stiffness is the cause of the inherent instability in bearingless motors and AMBs [1]. For small rotor radial displacements $r$ with respect to the effective air gap $\delta_\mathrm{e}$, i.e. $\delta_\mathrm{e} \gg r$, the radial pulling force $F_r$ can be approximated proportional to the radial rotor displacement. According to [12], for machines with more than two poles, the radial pulling force can be approximated by (2.41), where $\hat{B}_\delta$ is the amplitude of the sinusoidal air gap field, $S_\mathrm{s}$ the active stator surface, $\delta_\mathrm{e}$ the effective air gap and $r$ the rotor radial displacement with respect to the center of the stator bore.

$$F_r = \frac{S_\mathrm{s}\hat{B}_\delta^2}{4\mu_0\delta_\mathrm{e}} r \tag{2.41}$$

In the special case of a two-pole machine, the radial pulling force is only 50 % of (2.41). Considering that the two-pole PM field dominates in the air gap of the CBM, the force-displacement coefficient or *negative stiffness* in N/m for the CBM is defined by (2.42).

$$k_\mathrm{sr} = -\frac{S_\mathrm{s}\hat{B}_{0n}^2}{8\mu_0\delta_\mathrm{e}} \tag{2.42}$$

## 2.3 Linearization at the Operating Point

The motor will be considered as a *Linear Time Invariant* (LTI) system for the control design. The CBM can be linearized around its *Operating Point* (OP) to approximate a LTI system. The OP for the CBM is selected on the idle state (rest position), where the rotor center of mass levitates on the origin of the coordinate system. At the OP the radial and axial forces applied on the rotor ideally cancel each other. In order to levitate the rotor on the OP a bias-current should flow in the suspension winding. In the following, the axial force acting on the rotor is linearized and the bias-current needed for the motor levitation at OP is calculated.

Axial forces caused by the PM field are acting on the rotor cones. If the rotor stays exactly at $z = 0$ these forces have opposing directions and cancel each other. However, even small discrepancies form this position would create an axial force because the air gap changes and so does the magnetic field. For the DE cone, the PM flux density amplitude in dependence of the axial displacement $z$ is given in (2.43). The flux density amplitude of the NDE has a plus sign before $z$ because a positive displacement increases its air gap (2.44).

$$\hat{B}_{0n,\mathrm{DE}}(z) = \frac{B_\mathrm{R}}{1 + \frac{\mu_\mathrm{rM}}{h_\mathrm{M}}(h_\mathrm{B} + \delta_0 - z\sin\gamma)} \tag{2.43}$$

$$\hat{B}_{0n,\mathrm{NDE}}(z) = \frac{B_\mathrm{R}}{1 + \frac{\mu_\mathrm{rM}}{h_\mathrm{M}}(h_\mathrm{B} + \delta_0 + z\sin\gamma)} \tag{2.44}$$

For notation purposes, let $y_\mathrm{DE} = \hat{B}_{0n,\mathrm{DE}}(z)$ and $y_\mathrm{NDE} = \hat{B}_{0n,\mathrm{NDE}}(z)$. The derivative of the PM field for the DE is calculated in (2.45).

$$\frac{\mathrm{d}y_\mathrm{DE}}{\mathrm{d}z} = \sin\gamma \frac{\mu_\mathrm{rM}}{h_\mathrm{M}} \frac{B_\mathrm{R}}{\left[1 + \frac{\mu_\mathrm{rM}}{h_\mathrm{M}}(h_\mathrm{B} + \delta_0 - z\sin\gamma)\right]^2} \tag{2.45}$$

Similarly, the derivative of of the square of the PM field for the DE is calculated in (2.47).

$$\frac{\mathrm{d}y_{\mathrm{DE}}^2}{\mathrm{d}z} = 2y_{\mathrm{DE}}\frac{\mathrm{d}y_{\mathrm{DE}}}{\mathrm{d}z} \tag{2.46}$$

$$\frac{\mathrm{d}y_{\mathrm{DE}}^2}{\mathrm{d}z} = 2\sin\gamma\frac{\mu_{\mathrm{rM}}}{h_{\mathrm{M}}}\frac{B_{\mathrm{R}}^2}{\left[1+\frac{\mu_{\mathrm{rM}}}{h_{\mathrm{M}}}\left(h_{\mathrm{B}}+\delta_0-z\sin\gamma\right)\right]^3} \tag{2.47}$$

Following the same methodology for the NDE, the derivatives at $z = 0$ are calculated in (2.48).

$$\left.\frac{\mathrm{d}y_{\mathrm{DE}}^2}{\mathrm{d}z}\right|_{z=0} = -\left.\frac{\mathrm{d}y_{\mathrm{NDE}}^2}{\mathrm{d}z}\right|_{z=0} = 2\sin\gamma\frac{\mu_{\mathrm{rM}}}{h_{\mathrm{M}}}\frac{B_{\mathrm{R}}^2}{\left[1+\frac{\mu_{\mathrm{rM}}}{h_{\mathrm{M}}}\left(h_{\mathrm{B}}+\delta_0\right)\right]^3} \tag{2.48}$$

The axial force-displacement coefficient or *axial stiffness* can be expressed by (2.49) so that equation (2.32) is linearized at $z = 0$ (2.50).

$$k_{\mathrm{sz}} = -\frac{S_{\mathrm{s}}\sin\gamma}{2\mu_0}\left(\left.\frac{\mathrm{d}y_{\mathrm{DE}}^2}{\mathrm{d}z}\right|_{z=0} - \left.\frac{\mathrm{d}y_{\mathrm{NDE}}^2}{\mathrm{d}z}\right|_{z=0}\right) = -2\frac{S_{\mathrm{s}}\sin^2\gamma}{\mu_0}\frac{\mu_{\mathrm{rM}}}{h_{\mathrm{M}}}\frac{B_{\mathrm{R}}^2}{\left[1+\frac{\mu_{\mathrm{rM}}}{h_{\mathrm{M}}}\left(h_{\mathrm{B}}+\delta_0\right)\right]^3} \tag{2.49}$$

$$F_{z\,\mathrm{net}} = k_{\mathrm{iz}}\left(I_{1\mathrm{d}_{\mathrm{DE}}} - I_{1\mathrm{dDE}}\right) - k_{\mathrm{sz}}z \tag{2.50}$$

According to the PM field calculated in Table 2.1 for rotor-2, an axial stiffness of about −15 N/mm is calculated. That is, for an axial displacement of 0.2 mm an axial force of about 3 N is obtained. Due to the generation of non-negligible forces the axial stiffness is considered to the further modeling.

Considering that each conical motor should hold half the rotor weight, the $q$-current per cone required to hold the rotor at the OP, the so called *bias current*, is given in (2.51), where $m_{\mathrm{r}}$ is the rotor mass and $g$ the gravitational acceleration.

$$I_{2\mathrm{q,bias}} \approx \frac{m_{\mathrm{r}}g}{2k_{\mathrm{ir}}} \tag{2.51}$$

According to the PM fields calculated in Table 2.1, the bias current is about 3.2 A for rotor-1 and 2.9 A for rotor-2.

The initial $q$-current per cone required to raise the rotor from a remote position $y_{\mathrm{rem}}$ to the OP is given in (2.52).

$$I_{2\mathrm{q,init}} \approx I_{2\mathrm{q,bias}} - \frac{k_{\mathrm{sr}}}{k_{\mathrm{ir}}}y_{\mathrm{rem}} \tag{2.52}$$

The most remote rotor position is about 150 µm, therefore a current of about 5.6 A is required to bring rotor-2 to the OP.

This short evaluation shows that the required levitation currents lie well inside the current range of the inverter, i.e. ±10 A. In this work, the most important motor coefficients are calculated by the Matlab function `calcmot` (see Appendix B).

## 2.4 Model of the Magnetically Levitated Rotor

The levitating double conical rotor is displayed in Figure 2.1. The model of the CBM described in this chapter was inspired by the rigid rotor model with magnetic bearings presented in [1]. The so called *center of mass coordinates* are used, i.e. the rotor position is described by the displacement of the rotor center of mass with respect to an inertially fixed coordinate system. The selection of the center of mass coordinates simplifies the resulting differential equations [1]. A more thorough presentation of rotor dynamics and mechanical modeling, including magnetically levitated rotors, can be found in [13]. Before describing the model, some definitions and the basic conditions under which the model is valid are presented:

- The rotor is rigid.
- The rotor nominal position is defined so that the clearances between the the stator and the rotor are maxima.
- Deviations from the nominal position are small in relation to the rotor dimensions.
- The rotor system of principal axes is defined as $S\text{-}x_0y_0z_0$, where $S$ denotes the rotor center of mass.
- The origin $O$ of the inertially fixed coordinate system $O\text{-}xyz$ is defined so that it coincides with the rotor center of mass $S$, when the rotor is at its nominal position.
- The rotor position is defined as the displacement of its center of mass $S$ with respect to the inertially fixed coordinate system $O$.

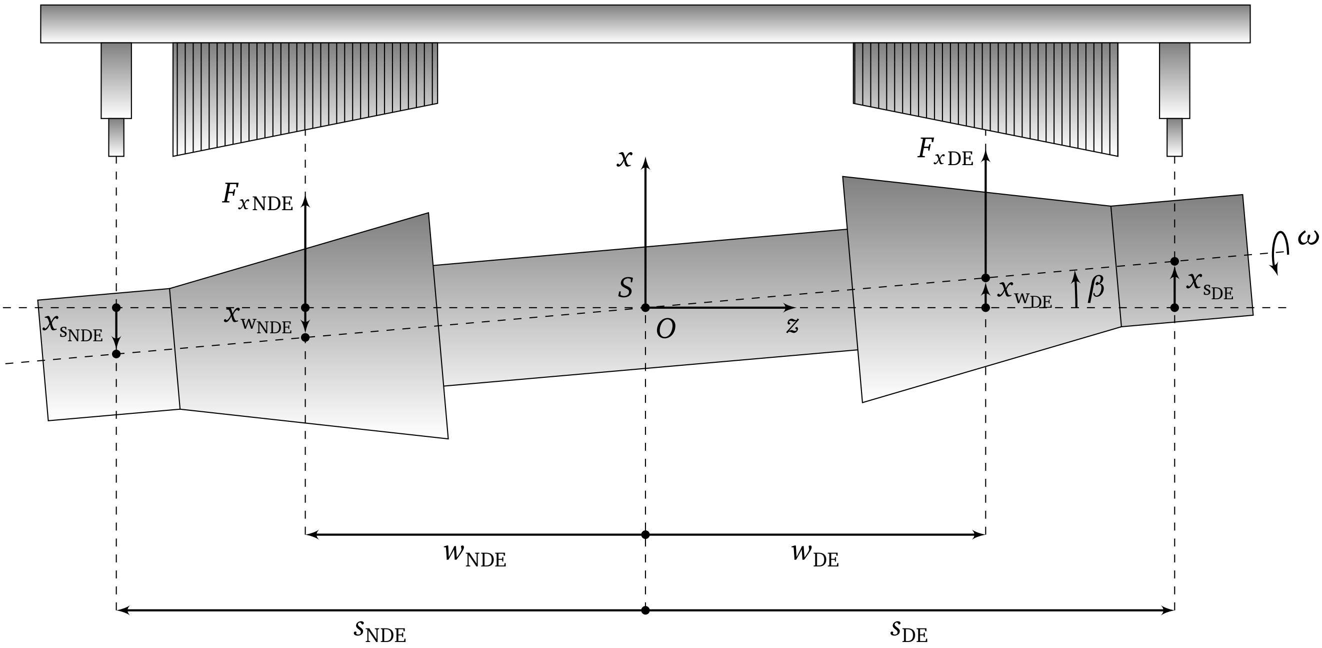

**Figure 2.1.:** The levitating double conical bearingless rotor

Since the forces are applied to the cones and the displacements are measured at the sensor planes (see Figure 2.1), coordinate transformations are required. Considering four planes parallel to the $x$-$y$-plane passing from the middle of each sensor and winding, the distances $s_{\text{DE}}, s_{\text{NDE}}, w_{\text{DE}}, w_{\text{NDE}}$ are defined as the axial displacements of these planes from the $x$-$y$-plane. If the motor is symmetrically designed, which corresponds to the depiction of Figure 2.1, it holds $w_{\text{DE}} = -w_{\text{NDE}}$ and $s_{\text{DE}} = -s_{\text{NDE}}$.

Let $\boldsymbol{q}$ be a vector, where $x, y$ denote the displacements of the center of mass from the origin and $\alpha, \beta$ denote the *Euler angles* representing the orientation of the rotor system of principal axes with respect to the fixed reference frame $O$-$xyz$ (2.53). The $y$-axis is not depicted in Figure 2.1, but due to the rotor symmetry about the $z$-axis, the $x$-$z$-plane can be considered equivalent to the $y$-$z$-plane. Although in Figure 2.1 the center of mass coincides with the geometric center of the rotor in order to simplify the depiction, generally it can be arbitrarily placed inside or outside the rotor dimensions. Effort is given during the rotor design and manufacturing that the center of mass coincides with the rotor geometric center. However, due to imperfections in the rotor construction, a small displacement of the center of mass from the rotational axis is always present, even if rotor balancing is applied. Besides, if one rotor end is permanently loaded (usually different accessories can be screwed to the rotor drive end) the center of mass will be shifted towards this side. The displacement of the center of mass causes the so called *mass imbalance*, which will be discussed in Section 3.5.

The radial displacements $x_{\mathrm{w_{DE}}}, x_{\mathrm{w_{NDE}}}, y_{\mathrm{w_{DE}}}, y_{\mathrm{w_{NDE}}}$ at the winding planes with respect to the origin can be expressed by the vector $\boldsymbol{q}_{\mathrm{w}}$. Similarly the displacements at the sensor planes are expressed by the vector $\boldsymbol{q}_{\mathrm{s}}$ (2.53).

$$\boldsymbol{q} = \begin{pmatrix} \beta \\ x \\ -\alpha \\ y \end{pmatrix} \qquad \boldsymbol{q}_{\mathrm{w}} = \begin{pmatrix} x_{\mathrm{wDE}} \\ x_{\mathrm{wNDE}} \\ y_{\mathrm{wDE}} \\ y_{\mathrm{wNDE}} \end{pmatrix} \qquad \boldsymbol{q}_{\mathrm{s}} = \begin{pmatrix} x_{\mathrm{sDE}} \\ x_{\mathrm{sNDE}} \\ y_{\mathrm{sDE}} \\ y_{\mathrm{sNDE}} \end{pmatrix} \tag{2.53}$$

Using the transformation matrices $\boldsymbol{B}_{\mathrm{w}}$ and $\boldsymbol{C}_{\mathrm{s}}$ (2.54), the displacements at the winding and sensor planes can be transformed to displacements of the center of mass or vice versa (2.55).

$$\boldsymbol{B}_{\mathrm{w}} = \begin{pmatrix} w_{\mathrm{DE}} & 1 & 0 & 0 \\ w_{\mathrm{NDE}} & 1 & 0 & 0 \\ 0 & 0 & w_{\mathrm{DE}} & 1 \\ 0 & 0 & w_{\mathrm{NDE}} & 1 \end{pmatrix} \qquad \boldsymbol{C}_{\mathrm{s}} = \begin{pmatrix} s_{\mathrm{DE}} & 1 & 0 & 0 \\ s_{\mathrm{NDE}} & 1 & 0 & 0 \\ 0 & 0 & s_{\mathrm{DE}} & 1 \\ 0 & 0 & s_{\mathrm{NDE}} & 1 \end{pmatrix} \tag{2.54}$$

$$\begin{aligned} \boldsymbol{q}_{\mathrm{w}} &= \boldsymbol{B}_{\mathrm{w}}\boldsymbol{q} \\ \boldsymbol{q}_{\mathrm{s}} &= \boldsymbol{C}_{\mathrm{s}}\boldsymbol{q} \end{aligned} \tag{2.55}$$

A combination of forces coming from the levitation currents and the inherited negative stiffness of the magnetic levitation are applied to the rotor. Assuming that the radial forces act at the winding planes, the force vector $\boldsymbol{f}$ is defined in (2.56). The corresponding currents are defined by the vector $\boldsymbol{i}$ in (2.57). Assuming a common negative stiffness $k_{\mathrm{sr}}$ and force-current coefficient $k_{\mathrm{ir}}$ for both conical motors, the radial forces applied to the rotor can be expressed by (2.58).

$$\boldsymbol{f} = \begin{pmatrix} F_{x\mathrm{DE}} & F_{x\mathrm{NDE}} & F_{y_{\mathrm{DE}}} & F_{y_{\mathrm{NDE}}} \end{pmatrix}^{\mathsf{T}} \tag{2.56}$$

$$\boldsymbol{i} = \begin{pmatrix} I_{2\mathrm{dDE}} & I_{2\mathrm{dNDE}} & I_{2\mathrm{q_{DE}}} & I_{2\mathrm{q_{NDE}}} \end{pmatrix}^{\mathsf{T}} \tag{2.57}$$

$$\boldsymbol{f} = -k_{\mathrm{sr}}\boldsymbol{q}_{\mathrm{w}} + k_{\mathrm{ir}}\boldsymbol{i} \tag{2.58}$$

To obtain the motion equations for the levitating rotor, three more matrices are defined in (2.59). The inertia matrix $\boldsymbol{M}$ is a diagonal matrix containing the rotor inertia $m_{\mathrm{r}}$ and the transverse moments of inertia $J_x$, $J_y$ with respect to the rotor system of principal axes. The gyroscopic matrix $\boldsymbol{G}$ is skew symmetric, where $J_z$ denotes the polar moment of inertia with respect to the rotor system of principal axes and $\omega$ the rotor angular velocity. The input matrix $\boldsymbol{B}_{\mathrm{f}}$ transforms the forces acting on the winding planes to forces and moment of forces with respect to the center of mass. Using these matrices the system of motion equations for the levitating rotor is expressed in (2.60).

$$\boldsymbol{M}=\begin{pmatrix} J_x & 0 & 0 & 0 \\ 0 & m_\mathrm{r} & 0 & 0 \\ 0 & 0 & J_y & 0 \\ 0 & 0 & 0 & m_\mathrm{r} \end{pmatrix} \quad \boldsymbol{G}=\begin{pmatrix} 0 & J_z\omega & 0 & 0 \\ 0 & 0 & 0 & 0 \\ -J_z\omega & 0 & 0 & 0 \\ 0 & 0 & 0 & 0 \end{pmatrix} \quad \boldsymbol{B}_\mathrm{f}=\begin{pmatrix} w_\mathrm{DE} & w_\mathrm{NDE} & 0 & 0 \\ 1 & 1 & 0 & 0 \\ 0 & 0 & w_\mathrm{DE} & w_\mathrm{NDE} \\ 0 & 0 & 1 & 1 \end{pmatrix} \tag{2.59}$$

$$\boldsymbol{M}\ddot{\boldsymbol{q}}+\boldsymbol{G}\dot{\boldsymbol{q}}=\boldsymbol{B}_\mathrm{f}\boldsymbol{f} \tag{2.60}$$

Decomposing the force vector using (2.58) and (2.55), the relationship (2.61) is obtained. It is evident that $\boldsymbol{B}_\mathrm{f}$ is the transpose of $\boldsymbol{B}_\mathrm{w}$. Defining the product of the aforementioned matrices as $\boldsymbol{B}_\mathrm{s}$, equation (2.62) is obtained.

$$\boldsymbol{M}\ddot{\boldsymbol{q}}+\boldsymbol{G}\dot{\boldsymbol{q}}=-k_\mathrm{sr}\boldsymbol{B}_\mathrm{f}\boldsymbol{B}_\mathrm{w}\boldsymbol{q}+k_\mathrm{ir}\boldsymbol{B}_\mathrm{f}\boldsymbol{i} \tag{2.61}$$

$$\boldsymbol{B}_\mathrm{s}=\boldsymbol{B}_\mathrm{f}\boldsymbol{B}_\mathrm{w}=\boldsymbol{B}_\mathrm{f}\boldsymbol{B}_\mathrm{f}^\mathsf{T}=\begin{pmatrix} w_\mathrm{DE}^2+w_\mathrm{NDE}^2 & w_\mathrm{DE}+w_\mathrm{NDE} & 0 & 0 \\ w_\mathrm{DE}+w_\mathrm{NDE} & 2 & 0 & 0 \\ 0 & 0 & w_\mathrm{DE}^2+w_\mathrm{NDE}^2 & w_\mathrm{DE}+w_\mathrm{NDE} \\ 0 & 0 & w_\mathrm{DE}+w_\mathrm{NDE} & 2 \end{pmatrix} \tag{2.62}$$

The system of motion equations can be now brought to the form (2.63). It can be observed that the gyroscopic effect is responsible for the coupling between the $x$-$z$ and $y$-$z$ planes. The gyroscopic effect is not negligible and does influence the system response; more details can be found in [1]. If the gyroscopic matrix is kept in the representation, the system becomes time variant, because the angular speed changes with time. Even if the speed is added as a state to the system, as it will be later done, the product $\omega\dot{\boldsymbol{q}}$ would make the system non-linear. In order to obtain a LTI system, so that linear control can be applied, a special treatment of the gyroscopic coupling should be applied. A straightforward solution is to assume a time invariant gyroscopic matrix selecting a constant angular speed $\omega$. The selection can be done for any speed between 0 rpm and the motor maximum speed. If $\omega=0$ rpm is selected, the resulting system is simplified as the gyroscopic matrix vanishes. The latter selection would be sufficient to approximate a system with low gyroscopic coupling at low angular speed.

$$\boldsymbol{M}\ddot{\boldsymbol{q}}+\boldsymbol{G}\dot{\boldsymbol{q}}+k_\mathrm{sr}\boldsymbol{B}_\mathrm{s}\boldsymbol{q}=k_\mathrm{ir}\boldsymbol{B}_\mathrm{f}\boldsymbol{i} \tag{2.63}$$

Having an LTI system of motion equations, it is straightforward to convert it to the state space representation of (2.64), where $\boldsymbol{u}$ denotes the *input vector*, $\boldsymbol{x}$ the *state vector*, $\boldsymbol{y}$ the *output vector*, $\boldsymbol{A}$ the *state matrix*, $\boldsymbol{B}$ the *input matrix* and $\boldsymbol{C}$ the *output matrix*.

$$\begin{aligned}\dot{\boldsymbol{x}}&=\boldsymbol{A}\boldsymbol{x}+\boldsymbol{B}\boldsymbol{u}\\ \boldsymbol{y}&=\boldsymbol{C}\boldsymbol{x}\end{aligned} \tag{2.64}$$

Defining the current vector $\boldsymbol{i}$ as the input vector and the vector $\boldsymbol{q}$ as the state vector, the state space matrices for the CBM are obtained (2.65).

$$\boldsymbol{A}=\begin{pmatrix} 0 & \boldsymbol{I} \\ -k_\mathrm{sr}\boldsymbol{M}^{-1}\boldsymbol{B}_\mathrm{s} & \boldsymbol{M}^{-1}\boldsymbol{G} \end{pmatrix} \quad \boldsymbol{B}=\begin{pmatrix} 0 \\ k_\mathrm{ir}\boldsymbol{M}^{-1}\boldsymbol{B}_\mathrm{f} \end{pmatrix} \quad \boldsymbol{C}=\begin{pmatrix} \boldsymbol{C}_\mathrm{s} & 0 \end{pmatrix} \tag{2.65}$$

The eigenvalues of matrix $\boldsymbol{A}$ determine the system stability. As long as $k_\mathrm{sr}<0$, the system is unstable so that only a positive stiffness can stabilize the system. In case of positive stiffness $k_\mathrm{s}>0$, the eigenvalues of matrix $\boldsymbol{A}$ characterize the rotor natural vibrations [1]. If the motor is symmetrically designed, i.e. it holds $w_{\mathrm{DE}} = -w_{\mathrm{NDE}}$, the angular and translational vibrations are decoupled. In this particular case, the translational natural frequency for both the $x$-$z$ and $y$-$z$ planes is given by (2.66).

$$\omega_{\mathrm{T}} = \sqrt{\frac{2k_{\mathrm{s}}}{m_{\mathrm{r}}}} \tag{2.66}$$

For a non-rotating rotor, the gyroscopic effect is not present and the angular vibrations on the $x$-$z$ and $y$-$z$ planes are decoupled. In this particular case, the angular natural frequency on the $y$-$z$-plane is given by (2.67). The angular natural frequency for the $x$-$z$-plane can be equivalently calculated considering the corresponding transverse moment of inertia $J_y$.

$$\omega_{\mathrm{A}} = \sqrt{\frac{2k_{\mathrm{s}}w_{\mathrm{DE}}^2}{J_x}} \tag{2.67}$$

Due to the gyroscopic coupling, the angular natural frequencies do not remain constant with increasing speed. In contrast, the translational natural frequency is not affected by the speed change. The latter has significant consequences for the control design. The different natural frequencies of the angular and translational motions impose different dynamics. For this reason, it would be advantageous to control the angular and translational motion independently. An approach for independent control of the angular and translation motion, which is based on four PID controllers, is presented in [1]. The pole placement control approach presented in Section 3.1 also succeeds to decouple the control of the angular and translation motion. From now on, the pure translational motion will be referred also as common motion or common mode, whereas the pure angular motion will be referred also as differential motion or differential mode. In this context, the term *mode* is not related with the resonance, but only with the motion pattern.

Apart from the radial motion, the rotor can move axially and rotate around the $z$-axis. The next step is to augment the state space system with the axial and rotational equations of motion. It should be noted that in order to add the new states to the existing state space system of radial motion, all possible couplings between the radial, axial and rotational motion are neglected. Considering that the driving windings for each cone are supplied by the same $I_{1\mathrm{q}}$ and opposite $I_{1\mathrm{d}}$ (2.68), the axial and the rotational equations can be expressed by (2.69) and (2.70) respectively.

$$\begin{aligned} I_{1\mathrm{d}} &= I_{1\mathrm{dDE}} = -I_{1\mathrm{dNDE}} \\ I_{1\mathrm{q}} &= I_{1\mathrm{q}_{\mathrm{DE}}} = I_{1\mathrm{q}_{\mathrm{NDE}}} \end{aligned} \tag{2.68}$$

$$m_{\mathrm{r}}\ddot{z} = 2k_{\mathrm{iz}}I_{1\mathrm{q}} + k_{\mathrm{sz}}z \tag{2.69}$$

$$J_z\dot{\omega} = 2k_{\mathrm{M}}I_{1\mathrm{d}} \tag{2.70}$$

Doing the augmentation, a state space representation with six inputs, eleven states and six outputs is obtained. The state vector $\boldsymbol{x}$, input vector $\boldsymbol{u}$ and output vector $\boldsymbol{y}$ are given in (2.71). In this work, the Matlab function `ssmot` was used to generate the state space representation from the given CBM design parameters.

$$\boldsymbol{u} = \begin{pmatrix} I_{2\mathrm{dDE}} \\ I_{2\mathrm{dNDE}} \\ I_{2\mathrm{qDE}} \\ I_{2\mathrm{qNDE}} \\ I_{1\mathrm{d}} \\ I_{1\mathrm{q}} \end{pmatrix} \qquad \boldsymbol{x} = \begin{pmatrix} \beta \\ x \\ \alpha \\ y \\ z \\ \omega \\ \dot{\beta} \\ \dot{x} \\ \dot{\alpha} \\ \dot{y} \\ \dot{z} \end{pmatrix} \qquad \boldsymbol{y} = \begin{pmatrix} x_{\mathrm{sDE}} \\ x_{\mathrm{sNDE}} \\ y_{\mathrm{sDE}} \\ y_{\mathrm{sNDE}} \\ z \\ \omega \end{pmatrix} \tag{2.71}$$

Deriving the differential equations of the CBM and representing them in state space concludes the system modeling task and opens the way for the control design. Different control approaches for the CBM will be investigated in the following chapters.

# 3 Control Design

In this chapter, three different control approaches for the CBM are presented. Firstly, the *pole placement* approach is described and ways to obtain a full state feedback are given. Secondly, an optimal control approach, the so called *Linear Quadratic Gaussian* (LQG) control is investigated. Finally, the feasibility to drive and suspend the motor using *Model Predictive Control* (MPC) is examined.

## 3.1 Pole Placement

The main advantage of the pole placement approach is that the poles of the closed loop can be freely placed on the open left half of the complex plane. That has a considerable advantage over the root locus method, where the poles can be placed only on specific paths in order to select the proportional gain of the PI or PID controller. The further the left the poles are placed, the faster the system dynamics become. However, placing the poles far to the left, turns to be very demanding for the actuators. Since every actuator has physical limits, e.g. an inverter has a current limit, placing the closed loop poles far to the left drives the actuator to its limits. Hence, the poles should be placed so that the desired dynamics for the application are fulfilled. Necessary condition for the pole placement is the existence of a full state feedback. A full state feedback means that all the system states must be available and fed back to the controller, which is often either not possible by measurements or very costly. However, the later issue can be solved by an observer which estimates the system states using the system inputs and measured outputs. A necessary condition to estimate all the system states is that the system is fully observable.

A closed loop control with an observer providing full state feedback does not guarantee steady state tracking. This is always the case because of the disturbances applied to the real system and the inaccuracies of the system parameters used for the control design. A sufficient way to heal both issues is to augment the controller with integral action. The option to use a disturbance observer would make the system dynamics less predictable in case of an inaccurate system model. As mentioned in [5], a state controller with integral action leads to a structural modification of the control law that increases control robustness against plant uncertainties.

In order to place the system poles, the so called *Full Modal Synthesis* (FMS) method is used [6]. Using the FMS, not only the eigenvalues of the closed loop system can be freely selected but also the effect of the eigenvalues to each state can be influenced using the so called *parameter vectors*. This extra freedom gives a significant advantage, e.g. the possibility to completely decouple the system. The option to use the built-in Matlab function `place`, was assessed insufficient. Although `place` uses the extra freedom to increase the control robustness, it is unclear how the eigenvalues affect the states and consequently the outputs.

In the following, a short description of the FMS method is given. A more detailed presentation of the method can be found in [5, 6]. Let a differential equation or *state equation* of the form (3.1), where $\boldsymbol{u}$ denotes the *input vector*, $\boldsymbol{x}$ the *state vector*, $\boldsymbol{A}$ the *state matrix* and $\boldsymbol{B}$ the *input matrix*. The number of states is $n$ and the number of inputs $m$. Consequently, $\boldsymbol{A}$ is square matrix of order $n$ and $\boldsymbol{B}$ a $n \times m$ matrix. Let $\boldsymbol{K}$ be a $m \times n$ *control matrix* or *state feedback matrix* such that the full state feedback of (3.2) is the input to the state equation (3.1). The closed loop state equation can be then transformed to (3.3).

$$\dot{\boldsymbol{x}} = \boldsymbol{A}\boldsymbol{x} + \boldsymbol{B}\boldsymbol{u} \tag{3.1}$$

$$\boldsymbol{u} = -\boldsymbol{K}\boldsymbol{x} \tag{3.2}$$

$$\dot{x} = (\boldsymbol{A} - \boldsymbol{BK})\boldsymbol{x} \tag{3.3}$$

It is claimed that the closed-loop system of (3.3) has $n$ distinct eigenvalues denoted as $\lambda_1, \dots \lambda_i \dots, \lambda_n$ and their corresponding eigenvectors $v_i$. Trying to calculate the control matrix only by the desired eigenvalues, it becomes clear that the system of (3.4) is underdetermined. This freedom can be exploited defining the *parameter vectors* in (3.5).

$$(\boldsymbol{A} - \boldsymbol{BK} - \lambda_i \boldsymbol{I}) v_i = 0, \qquad i = 1 \dots n \tag{3.4}$$

$$\boldsymbol{p}_i = \boldsymbol{K} v_i, \qquad i = 1 \dots n \tag{3.5}$$

Using the recently defined parameter vectors, equation (3.4) can be transformed to (3.6). Given that the matrix $\boldsymbol{A} - \lambda_i \boldsymbol{I}$ is invertible, equation (3.6) is transformed to (3.7). As (3.5) and (3.7) must hold for every $i$, the relationship (3.8) is made up. Given that the eigenvectors $v_i$ are linearly independent, equation (3.9) is obtained. That is, selecting $n$ parameter vectors $\boldsymbol{p}_1, \dots, \boldsymbol{p}_n$ and eigenvalues $\lambda_1, \dots \lambda_n$, the control matrix $\boldsymbol{K}$ is strictly defined by (3.9) together with (3.7).

$$(\boldsymbol{A} - \lambda_i \boldsymbol{I}) v_i = \boldsymbol{B}\boldsymbol{p}_i, \qquad i = 1 \dots n \tag{3.6}$$

$$v_i = (\boldsymbol{A} - \lambda_i \boldsymbol{I})^{-1} \boldsymbol{B}\boldsymbol{p}_i, \qquad i = 1 \dots n \tag{3.7}$$

$$[\boldsymbol{p}_1, \dots, \boldsymbol{p}_n] = \boldsymbol{K}[v_1, \dots v_n] \tag{3.8}$$

$$\boldsymbol{K} = [\boldsymbol{p}_1, \dots, \boldsymbol{p}_n][v_1, \dots v_n]^{-1} \tag{3.9}$$

Selecting properly the parameter vectors, the design freedom can be exploited to influence the effect of the closed loop eigenvalues to each state. For example in case it is required that the eigenvalue $\lambda_1$ affects only the state $x_2$ then the parameter vector $\boldsymbol{p}_2$ must be selected so that the eigenvector given by (3.7) has only one non zero component, i.e. $v_2 = [0, 1 \dots 0]^\mathsf{T}$.

The only requirement for the selection of the parameter vectors is that the resulting closed loop eigenvectors are linearly independent so that the eigenvector matrix of (3.8) is invertible. Furthermore, the selected closed loop eigenvalues should not coincide with the plant eigenvalues so that the inversion of (3.7) is valid. However, the latter condition is not necessary as it is proven in [5]. That is, it is possible to select closed loop eigenvalues being the same as the plant eigenvalues. The method doing that is not presented here but it can be found in [5].

Although the parameter vectors introduce an extra freedom to the control design their selection is rather time consuming and non-intuitive. An automatic selection of the parameter vectors so that the closed loop fulfills additional requirements seems more appropriate. A method that uses the extra design freedom to decouple the input-output of the system, the so called *Decoupling with Full Modal Synthesis*, is presented in [6, 7]. Before describing the method, it should be noted that a state space system can be represented in *Laplace domain*. Further details for the Laplace transformation of state space systems can be found in [14, 5]. Applying the Laplace transformation to (3.1) (taking as initial condition $\boldsymbol{x}_0 = \boldsymbol{0}$) and then inverting the matrix $(s\boldsymbol{I} - \boldsymbol{A})$, the equation (3.10) is derived. Multiplying with the output matrix $C$, the output is expressed in dependence of the input (3.11), i.e. the so called *transfer matrix* is derived in (3.12).

$$\boldsymbol{x}(s) = (s\boldsymbol{I} - \boldsymbol{A})^{-1}\boldsymbol{B}\boldsymbol{u}(s) \tag{3.10}$$

$$\boldsymbol{y}(s) = \boldsymbol{C}(s\boldsymbol{I} - \boldsymbol{A})^{-1}\boldsymbol{B}\boldsymbol{u}(s) \tag{3.11}$$

$$\boldsymbol{G}(s) = \boldsymbol{C}(s\boldsymbol{I} - \boldsymbol{A})^{-1}\boldsymbol{B} \tag{3.12}$$

Let a closed loop system be in accordance with the block diagram of Figure 3.1. The reference is denoted by the vector $\boldsymbol{r}$, the output by $\boldsymbol{y}$ and the plant input by $\boldsymbol{u}$. The matrices $\boldsymbol{A}, \boldsymbol{B}, \boldsymbol{C}$ denote the plant input, state and output matrices respectively and the matrix $\boldsymbol{K}$ denotes the state feedback matrix. The matrix $\boldsymbol{F}$ is a static prefilter aiming to provide steady state tracking. The transfer matrix of the closed loop depicted in Figure 3.1 is given in (3.13). As long as the prefilter provides steady state tracking, the relationship (3.14) must hold. Therefore, the prefilter should be selected so that it equals the inverse of the transfer matrix at $s = 0$ (3.15). More details about the prefilter design can be found in [5].

$$\boldsymbol{G}_{\mathrm{w}}(s) = \boldsymbol{C}(s\boldsymbol{I} - \boldsymbol{A} + \boldsymbol{B}\boldsymbol{K})^{-1}\boldsymbol{B}\boldsymbol{F} \tag{3.13}$$

$$\boldsymbol{G}_{\mathrm{w}}(0) = \boldsymbol{I} \tag{3.14}$$

$$\boldsymbol{F} = (\boldsymbol{C}(\boldsymbol{B}\boldsymbol{K} - \boldsymbol{A})^{-1}\boldsymbol{B})^{-1} \tag{3.15}$$

It has to be noted that the prefilter provides steady state tracking only if the plant model is identical with the real plant and no external disturbances are applied to the system. It is obvious that this is never true for real systems, so that the usefulness of the prefilter for steady state tracking is limited and is usually replaced by an integrator. However, keeping the prefilter to the system after adding an integrator can improve the closed loop response to a step reference. This type of control is usually called *Two-Degree-of-Freedom* control [5].

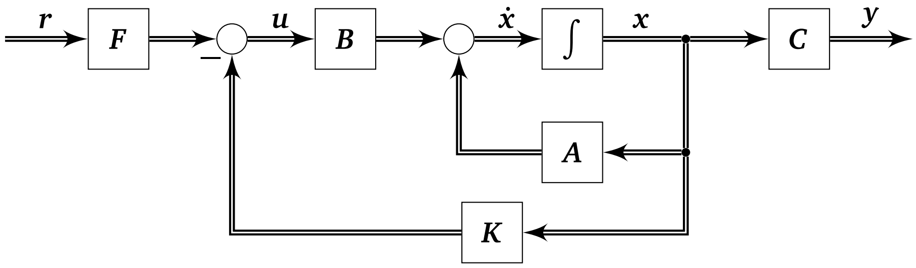

**Figure 3.1.:** Control design with static prefilter

Let the transfer matrix of a closed loop state space system be as that defined in (3.13). As long as the dynamic matrix of the closed loop $(\boldsymbol{A} - \boldsymbol{B}\boldsymbol{K})$ is not defective (i.e. the matrix is diagonalizable), it can be transformed to the modal form (3.16), where $\boldsymbol{V}$ is the eigenvector matrix, $\boldsymbol{W}$ the inverse eigenvector matrix and $\boldsymbol{\Lambda}$ the diagonal eigenvalue matrix. The transfer function matrix can be then written as in (3.18), which enables the transfer function matrix to be expressed in the summation form of (3.19), where $n$ denotes the system order, $v_i$ the columns of the eigenvector matrix $\boldsymbol{V}$ and $\boldsymbol{w}_i^{\mathsf{T}}$ the rows of the inverse eigenvector matrix $\boldsymbol{W}$.

$$(\boldsymbol{A} - \boldsymbol{B}\boldsymbol{K}) = \boldsymbol{V}\boldsymbol{\Lambda}\boldsymbol{W} \tag{3.16}$$

$$\boldsymbol{W} = \boldsymbol{V}^{-1} \tag{3.17}$$

$$\boldsymbol{G}_{\mathrm{w}}(s) = \boldsymbol{C}\boldsymbol{V}(s\boldsymbol{I} - \boldsymbol{\Lambda})^{-1}\boldsymbol{W}\boldsymbol{B}\boldsymbol{F} \tag{3.18}$$

$$\boldsymbol{G}_{\mathrm{w}}(s) = \sum_{i=1}^{n} \frac{\boldsymbol{C}\,\boldsymbol{v}_i\boldsymbol{w}_i^{\mathsf{T}}\boldsymbol{B}\boldsymbol{F}}{s - \lambda_i} \tag{3.19}$$

It can be observed in (3.19) that the term $\boldsymbol{C}\,\boldsymbol{v}_i$ represents a $m \times 1$ column vector, while the term $\boldsymbol{w}_i^{\mathsf{T}}\boldsymbol{B}\boldsymbol{F}$ a $1 \times m$ row vector (because $\boldsymbol{C}$ is a $m \times n$ matrix and $\boldsymbol{F}$ a $m \times m$ matrix). This type of vector multiplication is called *outer product*. In case of an equal number of elements for the row and column vectors, the outer product is an $m \times m$ square matrix. If the column vector $\boldsymbol{C}\,\boldsymbol{v}_i$ contains only one non-zero component at the index $j$, the eigenvalue $\lambda_i$ will affect only the output $y_j$. That is, if $\boldsymbol{e}_j$ is defined as a $m \times 1$ unit vector with the unity at the $j$th component, then (3.20) should hold. In the same way, the relationship (3.21) must hold so that the eigenvalue $\lambda_i$ is influenced only by the input $u_j$. Hence, an input-output decoupling is possible, if the relationship (3.22) holds for every eigenvalue $\lambda_i$ assigned to the $j$th input-output. The decoupling will produce an input-output transfer matrix as that given in (3.23).

$$\boldsymbol{C}\,\boldsymbol{v}_i = \boldsymbol{e}_j, \qquad i = 1 \ldots n, \qquad j = 1 \ldots m \tag{3.20}$$

$$\boldsymbol{w}_i^{\mathsf{T}}\boldsymbol{B}\boldsymbol{F} = \boldsymbol{e}_j{}^{\mathsf{T}}, \qquad i = 1 \ldots n, \qquad j = 1 \ldots m \tag{3.21}$$

$$\boldsymbol{C}\,\boldsymbol{v}_i\boldsymbol{w}_i^{\mathsf{T}}\boldsymbol{B}\boldsymbol{F} = \boldsymbol{e}_j\boldsymbol{e}_j^{\mathsf{T}}, \qquad i = 1 \ldots n, \qquad j = 1 \ldots m \tag{3.22}$$

$$\begin{pmatrix} g_{11}(s) & & 0 \\ & \ddots & \\ 0 & & g_{mm}(s) \end{pmatrix} \tag{3.23}$$

Combining the condition (3.20) with equation (3.7), the relationship (3.24) is obtained. Equation (3.26) defines how the parameter vectors should be calculated to decouple the output dynamics. Regarding the input decoupling, it is proven in [6] that a prefilter as given in (3.15) is sufficient. It should be noted that the described steps give only an overview of the method. For further details, such as how many eigenvalues should be assigned to each input-output and what is the influence of system zeros, it is advised to follow the complete method presentation in [7].

$$\boldsymbol{C}(\boldsymbol{A} - \lambda_i\boldsymbol{I})^{-1}\boldsymbol{B}\boldsymbol{p}_i = \boldsymbol{C}\,\boldsymbol{v}_i = \boldsymbol{e}_j, \qquad i = 1 \ldots n, \qquad j = 1 \ldots m \tag{3.24}$$

$$\boldsymbol{p}_i = (\boldsymbol{C}(\boldsymbol{A} - \lambda_i\boldsymbol{I})^{-1}\boldsymbol{B})^{-1}\boldsymbol{e}_j, \qquad i = 1 \ldots n, \qquad j = 1 \ldots m \tag{3.25}$$

$$\boldsymbol{p}_i = \boldsymbol{G}(\lambda_i)^{-1}\boldsymbol{e}_j, \qquad i = 1 \ldots n, \qquad j = 1 \ldots m \tag{3.26}$$

As already mentioned, a control design without integral action will provide steady state tracking, only in case the real plant is identical with the plant model and no disturbances are applied. The augmented with integral action control structure can be seen in Figure 3.2. The vector $\dot{\boldsymbol{x}}_{\mathrm{i}}$ denotes the integrator

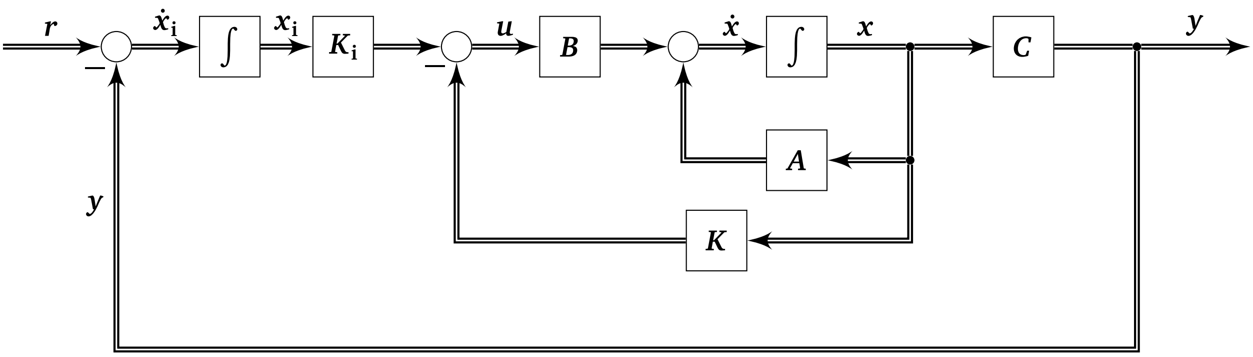

**Figure 3.2.:** Control design with integral action

input and the matrix $K_i$ the integral action matrix. The difference between this block diagram and that of (3.1) is the addition of an input-output comparison succeeding by an integrator and the removal of the prefilter.

A question arises for the augmented with $m$ integral states control structure; how should the pole placement be done? The answer to this problem can be found in [5, 15, 14, 16]. In the last two references the control structure with integral action is called servomechanism. The idea is to augment the open loop system, which initially contains only the plant, with the integral states $x_i$. Doing so, the state space representation of the new open loop system can be described by (3.27).

$$\begin{aligned} \begin{pmatrix} \dot{x} \\ \dot{x}_i \end{pmatrix} &= \begin{pmatrix} A & 0 \\ -C & 0 \end{pmatrix} \begin{pmatrix} x \\ x_i \end{pmatrix} + \begin{pmatrix} B \\ 0 \end{pmatrix} u \\ y &= \begin{pmatrix} C & 0 \end{pmatrix} \begin{pmatrix} x \\ x_i \end{pmatrix} \end{aligned} \tag{3.27}$$

Defining the new state vector as in (3.28) and the augmented system matrices as in (3.29), the new system can be described by the state space representation of (3.30).

$$x_a = \begin{pmatrix} x \\ x_i \end{pmatrix} \tag{3.28}$$

$$A_a = \begin{pmatrix} A & 0 \\ -C & 0 \end{pmatrix} \qquad B_a = \begin{pmatrix} B \\ 0 \end{pmatrix} \qquad C_a = \begin{pmatrix} C & 0 \end{pmatrix} \tag{3.29}$$

$$\begin{aligned} \dot{x}_a &= A_a x_a + B_a u \\ y &= C_a x_a \end{aligned} \tag{3.30}$$

Then, the feedback law of the augmented system can be written as in (3.31), where $K_c$ denotes the combined control matrix given in (3.32).

$$u = -Kx + K_i x_i = -K_c x_a \tag{3.31}$$

$$K_c = \begin{pmatrix} K & -K_i \end{pmatrix} \tag{3.32}$$

It can be seen in Figure 3.2 that the error defined by the reference-output comparison is expressed by (3.33). It follows that the closed loop state space system can be brought to the form (3.34).

$$\dot{\boldsymbol{x}}_{\mathrm{i}} = \boldsymbol{r} - \boldsymbol{y} = \boldsymbol{r} - \boldsymbol{C}\boldsymbol{x} \tag{3.33}$$

$$\begin{aligned} \dot{\boldsymbol{x}}_{\mathrm{a}} &= (\boldsymbol{A}_{\mathrm{a}} - \boldsymbol{B}_{\mathrm{a}}\boldsymbol{K}_{\mathrm{c}})\boldsymbol{x}_{\mathrm{a}} + \begin{pmatrix} 0 \\ \boldsymbol{I} \end{pmatrix} \boldsymbol{r} \\ \boldsymbol{y} &= \boldsymbol{C}_{\mathrm{a}}\boldsymbol{x}_{\mathrm{a}} \end{aligned} \tag{3.34}$$

Another way to express the closed loop system using directly the plant matrices is given in (3.35).

$$\begin{aligned} \begin{pmatrix} \dot{\boldsymbol{x}} \\ \dot{\boldsymbol{x}}_{\mathrm{i}} \end{pmatrix} &= \begin{pmatrix} \boldsymbol{A} - \boldsymbol{B}\boldsymbol{K} & \boldsymbol{B}\boldsymbol{K}_{\mathrm{i}} \\ -\boldsymbol{C} & 0 \end{pmatrix} \begin{pmatrix} \boldsymbol{x} \\ \boldsymbol{x}_{\mathrm{i}} \end{pmatrix} + \begin{pmatrix} 0 \\ \boldsymbol{I} \end{pmatrix} \boldsymbol{r} \\ \boldsymbol{y} &= \begin{pmatrix} \boldsymbol{C} & 0 \end{pmatrix} \begin{pmatrix} \boldsymbol{x} \\ \boldsymbol{x}_{\mathrm{i}} \end{pmatrix} \end{aligned} \tag{3.35}$$

It is now evident that the dynamics of the augmented system are defined by the matrix $(\boldsymbol{A}_{\mathrm{a}} - \boldsymbol{B}_{\mathrm{a}}\boldsymbol{K}_{\mathrm{c}})$. The already described method of full modal synthesis can be then used to place the poles, so that the state feedback matrix $\boldsymbol{K}_{\mathbf{c}}$ is calculated. However, due to the $m$ additional states $\boldsymbol{x}_{\mathrm{i}}$ of the augmented open loop system, $m$ extra eigenvalues must be placed.

As already mentioned doing the pole placement with FMS, not only the eigenvalues of the closed loop should be selected, but also the corresponding eigenvectors. The goal in the present control design is that each eigenvalue affects a single type of motion. For the CBM, it means that the dynamics of the rotational, axial, common and differential motions are decoupled. The decoupling method presented before decouples the system regarding to its inputs-outputs. To decouple the motions, an extra step should be done. The output matrix $C$ should be transformed so that each motion can be independently observed. This requires that the output matrix has full rank. Then a transformation matrix $T_{\mathrm{m}}$ can be found so that the new output matrix can be expressed by (3.36) and the states corresponding to each motion are expressed by (3.37). Consequently, the decoupling method described before can be applied. It has to be noted that the input of the augmented system does not affect the decoupling, since it passes through the same path as the integrator states.

$$\boldsymbol{C}_{\mathrm{m}} = \boldsymbol{T}_{\mathrm{m}}\boldsymbol{C} \tag{3.36}$$

$$\boldsymbol{x}_{\mathrm{m}} = \boldsymbol{T}_{\mathrm{m}}\boldsymbol{C}\boldsymbol{x} = \boldsymbol{C}_{\mathrm{m}}\boldsymbol{y} \tag{3.37}$$

Finally the eigenvalues for each motion should be defined. A selection of eigenvalues is presented in Table 3.1. The selection of Table 3.1 is based on the natural stiffness pole placement as presented in [1]. That is, for the common and differential motion (see Section 2.4), the amplitude of the closed loop eigenvalues is selected so that is close to the dominant stable eigenvalue of the open loop. This type of pole placement exhibits an increased robustness in presence of plant uncertainties [1]. The third pole for the axial common and differential motion, which in fact is the result of the integral action, is placed further to the left so that the complex conjugate pair defining the natural stiffness can be still considered as the dominant pole pair. Altogether eleven poles are placed because the common and differential motion takes place on both the $x$-$z$ and $y$-$z$ planes which are considered symmetrical. However, in case of specific motor operational requirements, a different placement can be done. Generally, high force and precision applications such as machine tooling will require a pole placement that goes further left from the $j$-axis, whereas for applications supporting low loads, such as high speed pumps, the poles can be placed closer to the $j$-axis. It should be noted that in order to place the poles further to the left, an adequate actuator is required. Otherwise, such a pole placement will drive the actuator to its limits. However, as it will be shown later, to drive the motor at high speed, the pole placement is less important

**Table 3.1.:** Closed loop pole placement and the initial plant poles

| **Motion** | **Poles in rad/s** | |
|---|---|---|
| | **Closed loop** | **Open loop** |
| Common | $-217 \pm j125, -500$ | $\pm 235$ |
| Differential | $-156 \pm j90, -360$ | $\pm 164$ |
| Axial | $-87 \pm j50, -200$ | $\pm 117$ |
| Rotation | $-9 \pm j2$ | 0 |

than the *synchronous filtering*. It can be said that if the main requirement is to operate the motor with low load at high speed, a pole placement stabilizing the closed loop system is usually sufficient.

Although the motor dynamics are described by differential equations, which means equation that are continuous in time, the controller sees the motor as a discrete plant. That is, the controller works under a predefined sampling period, inside which it must read the sensor feedback, calculate the next reference and send it to the output. Inside one sampling period, nothing changes in the controller input-output, though the plant states do not remain the same. The latter imposes limitations to the control design, e.g. the designed closed loop dynamics must be slower than the sampling frequency. It is evident that the controller cannot control faster dynamics than that it can observe, i.e. measure with the sensors. Therefore, the sampling frequency of the controller is usually the first thing defined in a closed loop controller. The sampling frequency for the position and speed control was set to $f_\mathrm{s} = 15\,625\,\mathrm{Hz}$. Considering that the designed closed loop dynamics are around 50 Hz, with no obvious aim to go higher, the sampling frequency is more than adequate. In the literature a ratio between the sampling frequency and the closed loop cutoff frequency not lower than 6 is recommended [17]. As long as the controller sees a discrete plant, the plant should be discretized for the control design. A continuous state space plant model can be brought to the discrete form (3.38), assuming *Zero Order Hold* (ZOH) with sampling period $T_\mathrm{s}$ for the input $\boldsymbol{u}$ [17].

$$\begin{aligned} \boldsymbol{x}[k+1] &= \boldsymbol{A}_\mathrm{d}\boldsymbol{x}[k] + \boldsymbol{B}_\mathrm{d}\boldsymbol{u}[k] \\ \boldsymbol{y}[k] &= \boldsymbol{C}_\mathrm{d}\boldsymbol{x}[k] \end{aligned} \tag{3.38}$$

The matrices $\boldsymbol{A}_\mathrm{d}$ and $\boldsymbol{B}_\mathrm{d}$ are defined by (3.39), whereas the output matrix remains the same, i.e. $\boldsymbol{C}_\mathrm{d} = \boldsymbol{C}$.

$$\begin{aligned} \boldsymbol{A}_\mathrm{d} &= \boldsymbol{e}^{\boldsymbol{A}T_\mathrm{s}} \\ \boldsymbol{B}_\mathrm{d} &= \int_0^{T_\mathrm{s}} \boldsymbol{e}^{\boldsymbol{A}\tau}\boldsymbol{B}\,\mathrm{d}\tau \end{aligned} \tag{3.39}$$

Having the plant model in discrete form, the desired closed loop eigenvalues should be mapped from the $s$-plane to the $z$-plane. The mapping is done by equation (3.40), where $\lambda_\mathrm{i}$ denote the desired eigenvalues at the $s$-plane and $z_\mathrm{i}$ the corresponding poles at the $z$-plane. Although the desired closed loop poles can be given directly at the $z$-plane, this would be less intuitive for the control design. Selecting the closed loop eigenvalues using the continuous plant, as done in Table 3.1, gives a better insight to the closed loop dynamics.

$$z_\mathrm{i} = e^{\lambda_\mathrm{i} T_\mathrm{s}}, \qquad i = 1 \ldots k \tag{3.40}$$

The FMS pole placement method already described remains unchanged for the discrete case. After the selection of the desired closed loop dynamics, the Matlab functions `fms` and `decfms` (Appendix B) can be used to calculate the state feedback matrix $\boldsymbol{K}$. However, in order to use the state feedback matrix, a full state feedback is required. Feasible ways to obtain a full state feedback will be later described.

## 3.2 State Observer

As already mentioned, the unconstrained selection of the closed loop system poles requires a full state feedback. The sensors installed in the CBM provide the information needed to calculate directly five states, i.e. the radial and axial displacements and the absolute rotor angular position. However, five states are not measured, i.e. the radial and axial velocities. In a fully observable system, an observer can be designed to estimate the non-measured states. In the literature the terms *Luenberger Observer* or *State Estimator* are used to described a state observer of the simplest form. The so-called *separation theorem* is proven in [14], which declares that as long as the plant model is identical with the real plant, the observer does not have any effect on the closed loop dynamics. That is, the closed loop dynamics are defined solely by the controller design and the observer dynamics solely by the observer pole placement. In practice the dynamics of the observer should always be faster than that of the closed loop. The latter means that the states should be estimated faster than the controller reacts. In reality the plant model has always imperfections, hence the separation theorem is valid only for simulations. This means that the observer will affect the closed loop pole placement. The influence it has depends on the accuracy of the plant model.

The principle of a *state observer* will be presented following the description given in [15]. The block diagram of a plant combined with a full state observer can be seen in Figure 3.2, where $\hat{\boldsymbol{x}}$ denotes the state estimate and $\hat{\boldsymbol{y}}$ the estimated output.

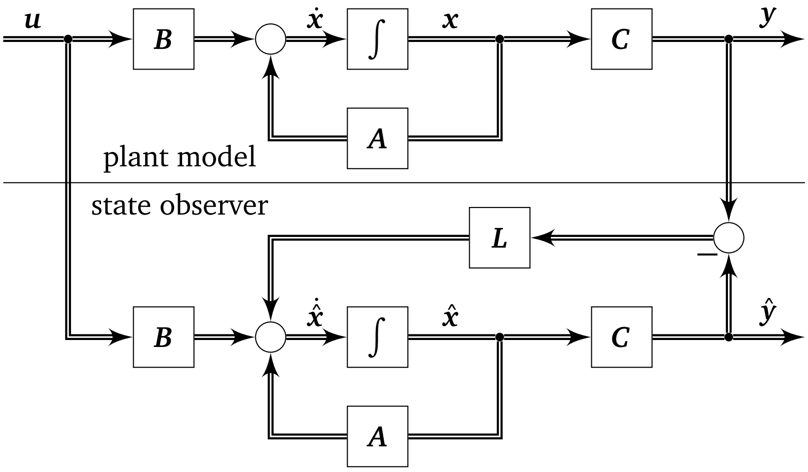

**Figure 3.3.:** Full order state observer

The differential equation that governs the state estimation is given in (3.41), where $\boldsymbol{L}$ denotes the *observer gain matrix*.

$$\dot{\hat{\boldsymbol{x}}} = (\boldsymbol{A} - \boldsymbol{L}\boldsymbol{C})\hat{\boldsymbol{x}} + \boldsymbol{B}\boldsymbol{u} + \boldsymbol{L}\boldsymbol{y} \tag{3.41}$$

As long as the eigenvalues of the matrix $\boldsymbol{A} - \boldsymbol{L}\boldsymbol{C}$ lie on the open left half of the complex plane, the observer is asymptotically stable. The asymptotic stability ensures that the state estimate vector will converge to the plant state vector for any initial state estimate. The eigenvalues of the matrix $\boldsymbol{A} - \boldsymbol{L}\boldsymbol{C}$ can be freely placed, using any pole placement method, e.g. `fms` or `place`. The discrete implementation of the state observer is quite similar to the continuous one already presented, more details can be found in [18, 19, 15].

A full state observer will try to estimate all the plant states, even the states that are directly measured. Often, only the non-measured states need to be estimated. For this reason, the so called *reduced order observer* is a common practice in real control applications. The complete derivation of a reduced order observer is not presented here, instead the reader is advised to see [15, 14]. Though, it is noticed that if the vector $\boldsymbol{x}_2$ denotes the non-measured states and vector $\boldsymbol{z}$ is an auxiliary state vector, the state space system given in (3.42) would describe the differential equations of the reduced order observer. Again $\boldsymbol{L}$ is the observer gain matrix, but this time the order of the dynamic matrix $\boldsymbol{M}$ is reduced, i.e. it equals the number of the non-measured states. The Matlab function `redobs` is developed to calculate the reduced order state observer for a given plant, (Appendix B).

$$\begin{aligned} \hat{\boldsymbol{x}}_2 &= \boldsymbol{z} + \boldsymbol{L}\boldsymbol{y} \\ \dot{\boldsymbol{z}} &= \boldsymbol{M}\hat{\boldsymbol{x}} + \boldsymbol{N}\boldsymbol{u} + \boldsymbol{P}\boldsymbol{y} \end{aligned} \tag{3.42}$$

Either a full state or a reduced order observer is used, the observer block diagram has two inputs, i.e. the plant input $\boldsymbol{u}$ and output $\boldsymbol{y}$, and one output, i.e. the state estimate $\hat{\boldsymbol{x}}$. Thus the closed loop block diagram of Figure 3.2 can be transformed to that of Figure 3.4, considering the plant as a block and adding a state observer.

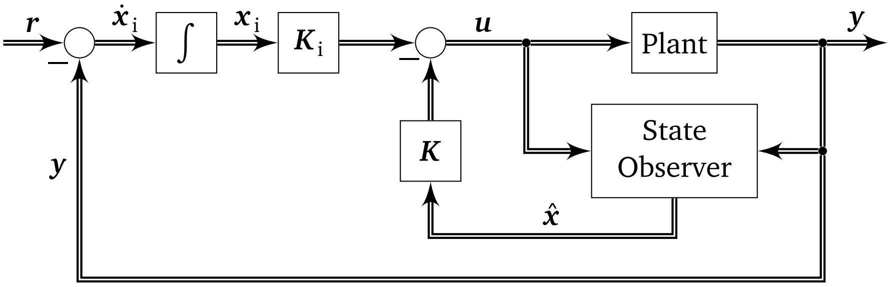

**Figure 3.4.:** Control design with integral action and state observer

In the present work, the observer poles are placed such that the observer dynamics are about ten times faster than that of the closed loop controller. The reduced order observer pole placement for each motion can be found in Table 3.2. Altogether, five observer poles are placed, because the common and differential motion takes place in both the $x$-$z$ and $y$-$z$ planes. That is, the order of the reduced order observer is five, whereas a full order state observer for the CBM would have order eleven.

**Table 3.2.:** Reduced order observer pole placement

| **Motion** | **Poles in rad/s** |
|---|---|
| Common | -5000 |
| Differential | -3600 |
| Axial | -2000 |

Placing the controller and state observer poles, a closed loop state controller is fully defined and ready to be simulated or directly tested to the real system. The simulation and implementation of the state controller will be discussed in the next chapters.

## 3.3 Linear Quadratic Gaussian Control

The LQG control belongs to the family of *optimal control* problems. Similarly to the pole placement, LQG is implemented using a full state feedback and an observer. The difference in LQG is that in order to calculate the state feedback matrix, an optimization method which evaluates a cost criterion is used. Furthermore, the state observer is also designed according to an optimization method that considers the process and measurement noise to obtain an optimal estimation, the so called *Kalman-Bucy Filter*. In the literature the terms *Linear Quadratic Regulator* (LQR) and *Linear Quadratic Estimator* (LQE) are also used to describe the optimal state feedback controller and the Kalman filter respectively. The literature dealing with optimal control is quite significant; most of the control theory textbooks include a chapter in optimal control. In this context, [15] gives an intuitive introduction to optimal control, stochastic processes and Kalman filtering. A more theoretical approach to linear quadratic control methods in conjunction with robustness is given in [20]. Additionally, a thorough presentation of optimal control including an insight to the quadratic weight selection is given in [21].

The linear quadratic problem for a continuous time state space system in its infinite horizon form can be described as the minimization of the the *cost functional* or *performance index* $J$ (3.43) for the selected state and input weight matrices $\boldsymbol{Q}$ and $\boldsymbol{R}$ respectively. The state and input weight matrices must be positive semi-definite and positive definite respectively.

$$J = \int_0^{\infty} \left(\boldsymbol{x}^{\mathsf{T}}\boldsymbol{Q}\boldsymbol{x} + \boldsymbol{u}^{\mathsf{T}}\boldsymbol{R}\boldsymbol{u}\right) \mathrm{d}\tau \tag{3.43}$$

The unique solution $\boldsymbol{P}$ of the *Continuous-time Algebraic Riccati Equation* (CARE) (3.44), leads to the calculation of the optimal state feedback matrix (3.45), which minimizes the cost functional $J$.

$$\boldsymbol{A}^{\mathsf{T}}\boldsymbol{P} + \boldsymbol{P}\boldsymbol{A} + \boldsymbol{Q} - \boldsymbol{P}\boldsymbol{B}\boldsymbol{R}^{-1}\boldsymbol{B}^{\mathsf{T}}\boldsymbol{P} = 0 \tag{3.44}$$

$$\boldsymbol{K} = \boldsymbol{R}^{-1}\boldsymbol{B}^{\mathsf{T}}\boldsymbol{P} \tag{3.45}$$

Since a digital controller sees a discrete plant, a corresponding performance index and Riccati equation should be defined for a discrete state space system. An infinite horizon LQR for a discrete state space system is defined so that it minimizes the performance index (3.46), using the optimal feedback matrix (3.47), where $\boldsymbol{P}$ is the unique solution of the *Discrete-time Algebraic Riccati Equation* (DARE) (3.48).

$$J = \sum_{k=0}^{\infty} \left(\boldsymbol{x}_{\mathrm{k}}{}^{\mathsf{T}}\boldsymbol{Q}\boldsymbol{x}_{\mathrm{k}} + \boldsymbol{u}_{\mathrm{k}}{}^{\mathsf{T}}\boldsymbol{R}\boldsymbol{u}_{\mathrm{k}}\right) \tag{3.46}$$

$$\boldsymbol{K} = \left(\boldsymbol{R} + \boldsymbol{B}^{\mathsf{T}}\boldsymbol{P}\boldsymbol{B}\right)^{-1}\boldsymbol{B}^{\mathsf{T}}\boldsymbol{P}\boldsymbol{A} \tag{3.47}$$

$$\boldsymbol{P} = \boldsymbol{Q} + \boldsymbol{A}^{\mathsf{T}}\left(\boldsymbol{P} - \boldsymbol{P}\boldsymbol{B}\left(\boldsymbol{R} + \boldsymbol{B}^{\mathsf{T}}\boldsymbol{P}\boldsymbol{B}\right)^{-1}\boldsymbol{B}^{\mathsf{T}}\boldsymbol{P}\right)\boldsymbol{A} \tag{3.48}$$

The continuous or discrete-time Riccati equation can be solved numerically in Matlab using the functions `care` and `dare`. Additionally Matlab offers the function `lqr`, which returns directly the optimal state feedback matrix. As already mentioned in the pole placement control design, a controller without integral action cannot provide steady state tracking to the real system. In order to provide steady state tracking, the system will be augmented with an integrator to each output. In this context, Matlab provides the function `lqi` which stands for *Linear Quadratic Integral* control. The `lqi` function does the system augmentation and calculates the optimal feedback matrix. If $m$ denotes the number of outputs, $m$ more quadratic weights should be provided due to the integral states.

Selecting the quadratic weights, the LQR design is completed. However, a full state feedback is still required. In fact the Luenberger observer already designed in the previous chapter could be used. Though, in order to achieve LQG control, an optimal observer should be designed. As the name implies, an optimal observer should provide an optimal observation minimizing a cost functional. The cost functional of the Kalman filter is related to the stochastic nature of the process and measurement noise. That is, for given process and measurement noise covariance matrices $\boldsymbol{Q}_{\mathrm{e}}$ and $\boldsymbol{R}_{\mathrm{e}}$ respectively, an optimal observer gain exists, so that the state estimation becomes optimum.

In order to describe the Kalman filter, a discrete time state space system including noise inputs is considered (3.49). The matrix $\boldsymbol{B}_\mathrm{w}$ aims mainly to scale the process noise vector $\boldsymbol{w}$, so that it is comparable with the system input vector $\boldsymbol{u}$. The sequences $\boldsymbol{w}[k]$ and $v[k]$ are uncorrelated, zero mean, white noise with covariances $\boldsymbol{Q}_\mathrm{e}$ and $\boldsymbol{R}_\mathrm{e}$ respectively.

$$\begin{aligned} \boldsymbol{x}[k+1] &= \boldsymbol{A}\boldsymbol{x}[k] + \boldsymbol{B}\boldsymbol{u}[k] + \boldsymbol{B}_\mathrm{w}\boldsymbol{w}[k] \\ \boldsymbol{y}[k] &= \boldsymbol{C}\boldsymbol{x}[k] + v[k] \end{aligned} \tag{3.49}$$

The state estimation time update of the *closed form discrete time Kalman filter* is described by equation (3.50). Following the proof given in [15], the optimal gain $\boldsymbol{L}$ is defined by (3.51), where $\boldsymbol{P}$ is the solution of the Riccatti equation (3.52). This time $\boldsymbol{P}$ is the solution of the system of coupled quadratic equations (3.51) and (3.52). In the literature the solution $\boldsymbol{P}$ (of the Kalman filter Riccati equation) is usually called *error covariance*.

$$\hat{\boldsymbol{x}}[k+1] = \boldsymbol{A}\hat{\boldsymbol{x}}[k] + \boldsymbol{B}\boldsymbol{u}[k] + \boldsymbol{L}(\boldsymbol{y}[k] - \boldsymbol{C}\hat{\boldsymbol{x}}[k]) \tag{3.50}$$

$$\boldsymbol{L} = \boldsymbol{A}\boldsymbol{P}\boldsymbol{C}^\mathsf{T}(\boldsymbol{C}\boldsymbol{P}\boldsymbol{C}^\mathsf{T} + \boldsymbol{R}_\mathrm{e})^{-1} \tag{3.51}$$

$$\boldsymbol{P} = \boldsymbol{A}\boldsymbol{P}\boldsymbol{A}^\mathsf{T} + \boldsymbol{B}_\mathrm{w}\boldsymbol{Q}_\mathrm{e}\boldsymbol{B}_\mathrm{w}^\mathsf{T} - \boldsymbol{L}\boldsymbol{C}\boldsymbol{P}\boldsymbol{A}^\mathsf{T} \tag{3.52}$$

Observing the state estimation update equation (3.50), it becomes clear that a discrete Kalman filter and a discrete state observer are of the same form. However, the calculated Kalman gain $\boldsymbol{L}$ is proven to be optimal, in case of process and measurement noise with covariance matrices $\boldsymbol{Q}_\mathrm{e}$ and $\boldsymbol{R}_\mathrm{e}$ respectively. It should be noticed that the presented Kalman filter is of the simplest static form. Time varying optimal observers can be also designed [21, 15].

Kalman filters with static gain $\boldsymbol{L}$ can be conveniently designed by the Matlab function `kalman`. Selecting the quadratic weights and the covariance matrices, the state feedback matrix and the Kalman filter are defined. The block diagram for the LQG control (Figure 3.5) is identical with that for pole placement (Figure 3.4), with the only difference that the Luenberger observer is replaced by a Kalman filter.

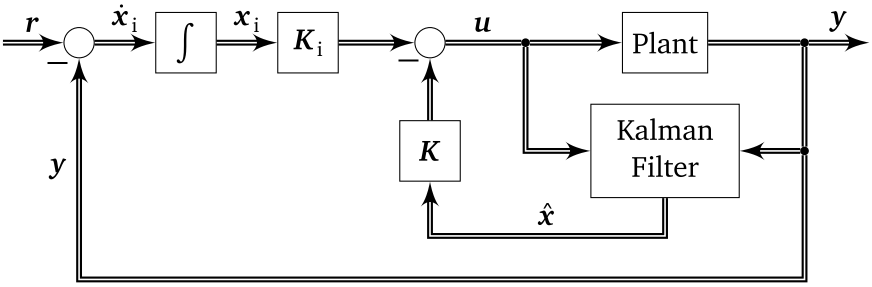

**Figure 3.5.:** Linear Quadratic Gaussian Control

The selection of the quadratic weights is unfortunately not as intuitive as the selection of the eigenvalues in pole placement. Trial and error is a common practice to select the weight matrices. Advices for an efficient weight selection process are given in [15, 21]. Hereafter the most important points for the weight selection are presented. As a general rule, if the dynamics of a state are too slow after simulation, the diagonal element of the weight matrix corresponding to this state should be increased. Furthermore, the weights corresponding to integrator states are selected high enough so that the input-output error converges faster to zero. Additionally, it is advised that the input weight matrix equals the identity matrix, so that the tuning can be done solely by the state weight matrix. Non-diagonal elements could be introduced to the state weight matrix in case of significant couplings between the states, otherwise they are generally undesirable because the generate artificial couplings between the states. Having as guide the aforementioned advices and performing some design iterations, it is concluded that a satisfactory response is obtained by the weight matrices:

$$\boldsymbol{Q} = \mathrm{diag}\begin{pmatrix} 1 & 1 & 1 & 1 & 1 & 0.0001 & 0 & 0 & 0 & 0 & 0 & 100 & 100 & 100 & 100 & 100 & 0.01 \end{pmatrix}$$
$$\boldsymbol{R} = \mathrm{diag}\begin{pmatrix} 1 & 1 & 1 & 1 & 1 & 1 \end{pmatrix}$$

It should be noted that the weight matrices correspond to the state and input vector as given in (2.71). The last $m$ weights of the $\boldsymbol{Q}$ matrix correspond to the integral states.

For the Kalman filter design the process and measurement noise covariance matrices should be selected. Capturing the converted in µm position sensor signals, an approximate maximum noise amplitude of $A \approx 0.3$ µm was observed for each sensor. Assuming *Gaussian white noise*, the standard deviation $\sigma$ is about one third of the observed maximum noise amplitude and the variance equals the square of the standard deviation (3.53).

$$\sigma^2 \approx \frac{A^2}{9} \tag{3.53}$$

The same procedure was applied to estimate the noise variance of the angular speed. Assuming no cross-correlation between the signals, the noise covariance matrix becomes diagonal. That is, each diagonal element equals the variance of each signal. Although the measurement noise covariance matrix was estimated observing the sensor signals, there is no such a straightforward method to estimate the process noise. The matrix $\boldsymbol{B}_w$ was selected equal to the plant input matrix $\boldsymbol{B}$ so that the process noise $\boldsymbol{w}$ and the plant input $\boldsymbol{u}$ share a common scaling. A first selection of the process noise covariance matrix can be now done, having in mind that the process noise corresponds to the input current. Finally, an adequate selection of the covariance matrices for the Kalman filter is done:

$$\boldsymbol{Q}_\mathrm{e} = \mathrm{diag}\begin{pmatrix} 0.1 & 0.1 & 0.1 & 0.1 & 0.1 & 0.1 \end{pmatrix}$$
$$\boldsymbol{R}_\mathrm{e} = \mathrm{diag}\begin{pmatrix} 0.01 & 0.01 & 0.01 & 0.01 & 0.01 & 0.3 \end{pmatrix}$$

## 3.4 Model Predictive Control

Model Predictive Control was initially introduced in the process industry, since the predictive algorithm needs extra computation effort, which fits better to processes with slow dynamics. That is, a slow process does not require a high sampling frequency so that the calculations have enough time to be executed inside one sampling period. The increasing power of modern electronics made MPC an attractive approach for processes with faster dynamics. The main difference between conventional control (PID Control) and predictive control is that the first one observes the current and remembers the past process variables, while the second one takes into account also the future process variables. The prediction of the future process variables becomes possible, using a process model. The length that the prediction lies in future is called *prediction horizon*. On one hand, the longer the prediction horizon lies in the future, the more optimal the controller response becomes since the cost functional is minimized. On the other hand, the longer the prediction horizon is, the more demanding the calculations become. However, there is a threshold after which the prediction is not useful for control action anymore.

An introduction to MPC is given in [22], a general treatment of Predictive Control is done in [23], whereas a detailed presentation of several MPC algorithms can be found in [24]. The optimization criterion for MPC is usually the minimization of a quadratic function. In case of an unconstrained quadratic optimization problem, the control design is reduced to the calculation of a state feedback. However, the most common control problems have input-output constraints. For control problems with constraints, a *Quadratic Programming* (QP) algorithm should be used. Finally, it has to be noted that the stability and robustness analysis of MPC structures with constraints is not a task that can be performed systematically, as done with conventional controllers.

A lot of different MPC algorithms are listed and some of them analyzed in [24]. The MPC algorithms differ in several points, e.g. optimization function, QP algorithm, state estimation, prediction model and disturbance model. In this work, the Matlab built-in algorithm based on a state space approach is used [25]. In the block diagram of Figure 3.6, which was inspired form the elemental MPC algorithm presented in [24], a basic structure of a MPC is displayed.

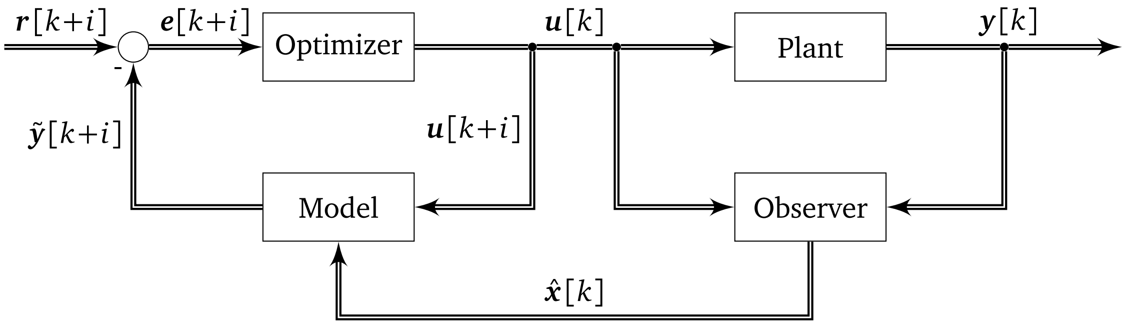

**Figure 3.6.:** Basic structure of Model Predictive Control

The discrete time MPC process of Figure 3.6 is described below in four main steps. The index $i$ denotes the future time steps and lies in the range $i = 0 \ldots P-1$, where $P$ is the prediction horizon, i.e the integer number of sampling periods for which the controller predicts the future plant outputs.

1. The model uses the estimated state $\hat{\boldsymbol{x}}[k]$ and the provided *future input* $\boldsymbol{u}[k+i]$ to generate the *predicted output* $\tilde{\boldsymbol{y}}[k+i]$.

2. The *future error* $\boldsymbol{e}[k+i] = \boldsymbol{r}[k+i] - \boldsymbol{y}[k+i]$, i.e. the difference between the *reference trajectory* and the predicted output, is calculated.

3. The optimizer uses the future error $\boldsymbol{e}[k+i]$, a cost function and eventually constraints to generate the future input $\boldsymbol{u}[k+i]$.

4. The future input sequence $\boldsymbol{u}[k+i]$ is fed to the model, whereas only the first input $\boldsymbol{u}[k]$ is fed to the plant.

Unfortunately there is a major problematic in the implementation of MPC for the CBM. Predictive control requires a sufficient long prediction horizon, such that the plant dynamics can be observed. As a rule of thumb a sampling period of about one fifth of the dominant time constant of the plant is selected. Then, a prediction horizon of 20-30 sampling periods is considered adequate, since it is approximately equal with the plant settling time [25]. However, for the control of the CBM the sampling period was set too low (the sampling frequency is about 300 times larger than the plant dominant frequency). Consequently, a prediction horizon of an unusual large number of sampling periods is required. It should be noted that simulating MPC for the CBM with a low sampling period of 64 µs and a prediction horizon of 30 sampling periods, the plant was sufficiently controlled. On one hand, a prediction horizon of 30 sampling periods with a time step of 64 µs is already ambitious for a real implementation (a large amount of calculations are required in a short time). On the other hand, the simulation would always give optimistic results for MPC as long as the plant model is identical with the real plant. In reality having a prediction horizon much shorter than the dominant plant time constant and a plant model with uncertainties, there is no guarantee that MPC can be successfully applied. Increasing the sampling period to a reasonable value for MPC opens the way for an implementation.

## 3.5 Imbalance Forces and Synchronous Filtering

As it was already mentioned in Section 2.4, a small displacement of the center of mass from the rotor geometric center is common in real rotors. This displacement is called *eccentricity* and is denoted by the vector $\boldsymbol{e}$. The displacement of the center of mass with respect to the geometric axis of symmetry is denoted by $e_\mathrm{r}$, whereas the inclination of the rotor principal axis with respect to the geometric axis of symmetry is denoted by $\epsilon_\mathrm{r}$. The distance $e_\mathrm{r}$ and the inclination $\epsilon_\mathrm{r}$ characterize the *static* and *dynamic imbalance* respectively [1]. If the rotor is forced to rotate with respect to its geometric axis of symmetry, the presence of static and dynamic imbalance will cause imbalance forces.

To visualize the effect of eccentricity, the simplified example of a rotor disk is presented in Figure 3.7. Initially the rotor mass is evenly distributed and the center of mass coincides with the rotor geometric center at $C$, but due to the attachment of the extra mass $m_\mathrm{e}$ on the rotor periphery the center of mass is displaced by the eccentricity $e_\mathrm{r}$ to $S$.

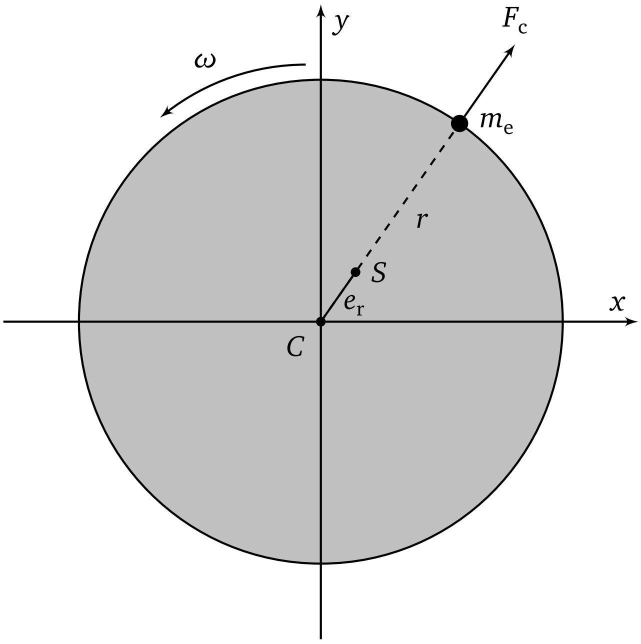

**Figure 3.7.:** Additional mass $m_\mathrm{e}$ causes the displacement of the rotor's center of mass by the eccentricity $e_\mathrm{r}$ and the generation of the centrifugal force $F_\mathrm{c}$

If the rotor is forced to rotate with respect to its geometric center $C$ a centrifugal force $F_\mathrm{c}$ will be applied on it. If $m_\mathrm{r}$ is the rotor mass and $\omega$ the rotational speed, the centrifugal force can be expressed by (3.54), where $e_\mathrm{r}$ is defined by (3.55) [13]. It has to be noted that if the rotor rotates with respect to its new center of mass $S$, no centrifugal force will be applied on it.

$$F_\mathrm{c} = m_\mathrm{r} e_\mathrm{r} \omega^2 \tag{3.54}$$

$$e_\mathrm{r} = \frac{m_\mathrm{e}}{m_\mathrm{r}} r \tag{3.55}$$

The direction of the centrifugal force depends on the eccentricity direction and rotates with the same angular speed as the rotor, i.e. the *synchronous frequency*. To avoid misunderstandings, it is noted that the defined synchronous frequency is the rotor mechanical frequency and not the electrical one. Consequently, the forces that can be observed on the $x$-$y$-plane adjusted vertically to the rotational axis are given by (3.56).

$$\begin{aligned} F_x &= F_c \cos(\omega t) \\ F_y &= F_c \sin(\omega t) \end{aligned} \tag{3.56}$$

In contrast to the rotor disk example, torques with respect to the $x$ and $y$ axes will be also present in a long rotor due to the presence of dynamic imbalance. These torques are also oscillating with synchronous frequency. In the literature, the imbalance forces acting on the rotor are often separated into a common mode component, due to the static imbalance and a differential mode component, due to the dynamic imbalance.

For a motor with conventional bearings, the imbalance forces would generate vibrations on the stator frame, mainly due to the mechanical coupling between the rotor and stator at the bearing planes. For a motor equipped with magnetic bearings or a bearingless motor, the synchronous forces would still generate vibrations on the stator frame due to the electromagnetic coupling between the rotor and stator. For bearingless motors, the radial forces applied to the rotor can be controlled by the levitation currents. Synchronous radial forces could be injected in order to compensate the imbalance forces, so that no vibrations are transferred to the stator. A different strategy could be to leave the imbalance forces completely uncompensated, so that the rotor is forced to rotate around its principal axis, given that the mechanical air gap is sufficiently large. In this work, the first strategy will be referred as *Imbalance Force Compensation* (IFC), whereas the second one as *Imbalance Force Rejection* (IFR).

The meaning of the terms IFC and IFR becomes clear, thinking what a conventional feedback controller does. A feedback controller with integral action cannot totally compensate for sinusoidal and in general periodic disturbances. The output oscillates with the disturbance frequency and a frequency dependent amplitude and phase. A way to follow the set point, with the already designed controller, would be to compensate the periodic disturbances, injecting the required control signals. The latter explains the term IFC; the control strategy is such that the levitation currents (control signals) generate such forces that exactly compensate the imbalance forces (periodic disturbances). In reality the controller reacts to the periodic disturbances, although it cannot reject them. If it is desirable that the control does not react at all to a periodic disturbance, the control signals should be forced to zero at the disturbance frequency. This explains the term IFR; the control strategy is such that the synchronous frequency corresponding to the imbalance forces (periodic disturbances) is rejected from the levitation currents (control signals). The rejection of the synchronous component of the levitation currents leaves the imbalance forces completely uncompensated and forces the rotor, provided that the air gap is sufficiently large, to rotate around its principal axis. As long as the rotor rotates around its principal axis, the cause of imbalance forces is eliminated. In other words, the imbalance forces are rejected. Both methods are extensively examined in the literature. A list of publications in the field of imbalance control is presented in [1].

The mass imbalance is not the only reason creating synchronous radial forces on a bearingless motor. Asymmetries of the air-gap field, e.g. due to a non-sinusoidal PM field distribution, will explicitly create synchronous radial forces. Additionally, asymmetries on the measuring surface of the radial position sensors will implicitly create synchronous radial forces due to the feedback control structure. The control strategies described above can handle not only the mass imbalance forces, but also any kind of synchronous disturbance forces. It is shown later that the IFC and IFR control strategies can be implemented designing filters that isolate the synchronous component of the process signals. The aforementioned reasons lead to select the more general term *synchronous filtering* to cover the described IFR and IFC control strategies applied to bearingless motors.

The filter design to achieve IFR and IFC was mainly inspired from [26], where the IFR problem is handled designing a generalized narrow-band *Notch Filter*. The proposed filter is based on the modulation block presented in Figure 3.8, where $\omega$ corresponds to the motor synchronous speed and $\boldsymbol{T}_{\mathrm{R}}$, $\boldsymbol{T}_{\mathrm{J}}$ are the so called parameter matrices which enable the filter tuning.

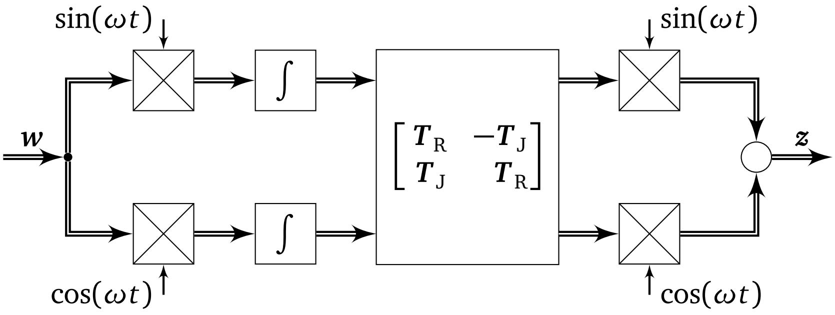
sin(ωt)
sin(ωt)
w
∫
∫
$\begin{bmatrix} \boldsymbol{T}_{\mathrm{R}} & -\boldsymbol{T}_{\mathrm{J}} \\ \boldsymbol{T}_{\mathrm{J}} & \boldsymbol{T}_{\mathrm{R}} \end{bmatrix}$
z
cos(ωt)
cos(ωt)

**Figure 3.8.:** Modulation block for synchronous filtering [26]

It is proven in [26] that this kind of modulation scheme has the input-output transfer matrix given in (3.57), so that $\boldsymbol{z}(s) = \boldsymbol{M}(s)\boldsymbol{w}(s)$ holds.

$$\boldsymbol{M}(s) = \frac{s\boldsymbol{T}_{\mathrm{R}} - \omega \boldsymbol{T}_{\mathrm{J}}}{s^2 + \omega^2} \tag{3.57}$$

Using the modulation block of Figure 3.8 the *Synchronous Notch Filter* of Figure 3.9, aiming to provide IFR, is designed. The transfer matrix of the synchronous notch filter is given in (3.59).

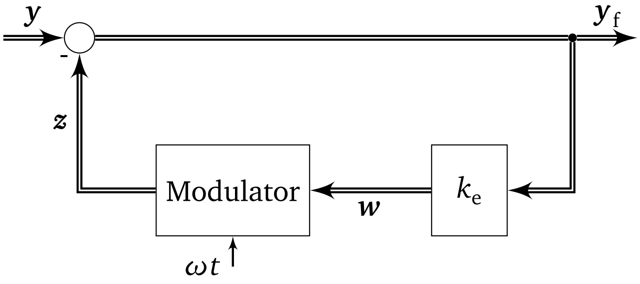

**Figure 3.9.:** Synchronous notch filter

$$N_{\mathrm{s}}(s) = (\boldsymbol{I} + k_{\mathrm{e}}\boldsymbol{M}(s))^{-1} \tag{3.58}$$

$$N_{\mathrm{s}}(s) = \left(s^2 + \omega^2\right)\left(s^2\boldsymbol{I} + sk_{\mathrm{e}}\boldsymbol{T}_{\mathrm{R}} + \omega^2\boldsymbol{I} - k_{\mathrm{e}}\omega\boldsymbol{T}_{\mathrm{J}}\right)^{-1} \tag{3.59}$$

The transfer matrix zeros at $s = \pm j\omega$, clarify the blocking characteristic of the notch filter at the synchronous frequency. The importance of the described notch filter, though, lies on the denominator. Selecting the parameter matrices $\boldsymbol{T}_{\mathrm{R}}$ and $\boldsymbol{T}_{\mathrm{J}}$, the poles of the notch filter can be freely placed. In [26] a method that evaluates the closed loop stability in conjunction with the selection of the parameter matrices is given. In order to implement the filter, some of the hints for the selection of the parameter matrices given in [26] are presented below. The parameter matrices can be used to phase shift the filter output, i.e. in the *Single Input Single Output* (SISO) case the angle $\angle(T_{\mathrm{R}} + jT_{\mathrm{J}})$ is related to the phase shift. Additionally, in the SISO case, the magnitude $|T_{\mathrm{R}} + jT_{\mathrm{J}}|$ as well as the coefficient $k_{\mathrm{e}}$ affect the convergence speed.

Reversing the feed-in and summation points, a *Synchronous Resonator* aiming to provide IFC can be designed, as shown in Figure 3.10.

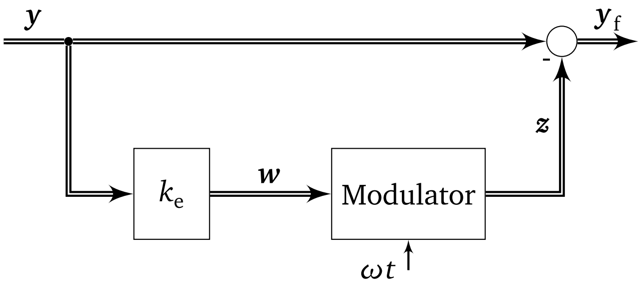

**Figure 3.10.:** Synchronous resonator

The synchronous resonator will amplify the synchronous component of the input $\boldsymbol{y}$ until it vanishes. That is, the controller will impose high current amplitudes at the synchronous frequency until the imbalance forces are completely compensated and therefore the output $y$ is free from any synchronous component. As the imbalance forces increase with the square of angular speed, this method is very demanding for the actuator and may drive it to its limits, before the motor reaches its nominal speed. The resonator transfer function is given in (3.61).

$$\boldsymbol{R}_s(s) = \boldsymbol{I} + k_e \boldsymbol{M}(s) = \boldsymbol{N}_s^{-1}(s) \tag{3.60}$$

$$\boldsymbol{R}_s(s) = \frac{s^2 \boldsymbol{I} + s k_e \boldsymbol{T}_R + \omega^2 \boldsymbol{I} - k_e \omega \boldsymbol{T}_J}{s^2 + \omega^2} \tag{3.61}$$

The IFR and IFC blocks could be placed either before or after the controller. Usually the placement before the controller is preferred for the notch filter and the placement after the controller for the resonator [1]. The latter has in both cases the advantage that the controller input is free from the synchronous component, as long as IFR and IFC converge. That is, the controller does not try to control the synchronous component since this is handled either by IFC or IFR. The observer should not have as inputs the plant input and output anymore, the plant is considered as being augmented by IFR or IFC. This has again the advantage that the observer does not observe the synchronous component, as long as IFR and IFC converge. The placement of IFR and IFC in the closed loop controller is shown in Figure 3.11.

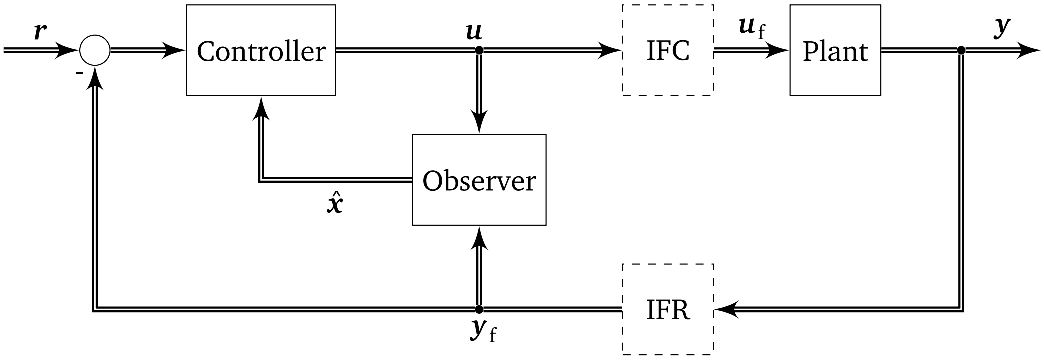

**Figure 3.11.:** Synchronous filtering in the closed loop

As the synchronous filtering strategy is adequately formulated, the control design for the CBM is complete, a simulation should be next tried to evaluate the designed controllers.

# 4 Simulation

The simulation of the control structures designed for the CBM has several objectives. First of all, an initial tuning of the controllers can be done, especially for LQG, where trial and error is the common approach to select the quadratic weights. Secondly, the control performance against disturbances and noise can be evaluated. Furthermore, since the control complexity increases with the additional IFR and IFC control strategies, several parameter combinations for the controller and synchronous filtering can be evaluated. Generally, having a simulation structure considering most of the phenomena occurring in the real plant, a lot of control ideas can be easily tried out obtaining reliable results. Trying every new idea to the real plant is a laborious work, even if systems that enable rapid control prototyping, like RTAI, are used.

## 4.1 Closed Loop Control Structure

A simplified block diagram representing the simulated closed loop structure is displayed in Figure 4.1. The inputs $\boldsymbol{w}$ and $\boldsymbol{v}$ denote uncorrelated, zero mean, white noise for the process and measurement respectively. The input $\boldsymbol{d}$ denotes the process disturbances and is fed by constant loads, step disturbances and synchronous disturbances (imbalance forces). The IFR and IFC blocks are dashed to denote that they can be turned on or off. When IFR and IFC are turned off, the process signals pass unaffected though them. It is evident that IFR and IFC must not be simultaneously turned on, only one imbalance control strategy can be applied at each time. The observer is connected before IFC and IFR, for the reasons explained in Section 3.5. The reference-output comparison implies that the controller provides integral action. The ZOH block discretizes the continuous plant output, so that discrete observers and controllers can be tested.

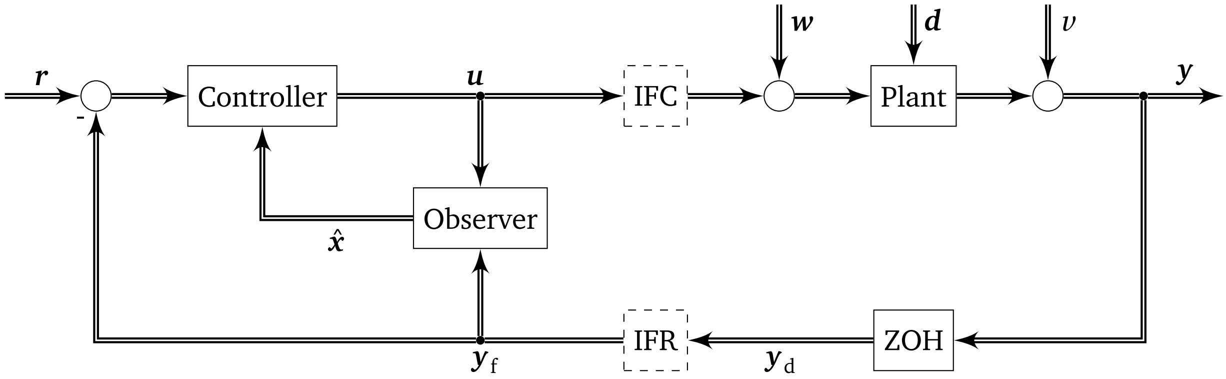

**Figure 4.1.:** Simulation block diagram

The control structure displayed in Figure 4.1 was the guide to generate the Simulink model `cbm_control`. Every block presented in Figure 4.1 can be independently designed as a subsystem in Simulink. This provides the flexibility to test several controller and observer combinations with the same plant. For example a controller based on pole placement can be tried with a Luenberger observer and subsequently with a Kalman filter, without changing any other block.

In this work, pole placement, LQG and MPC structures were simulated. The CBM with rotor-2 was used as a plant, the plant data were drawn from file `motor2`. A continuous solver was used for the simulation but the plant output was discretized with the sampling period $T_s = 64\,\mu\text{s}$. Consequently, only discrete time controllers were simulated. A separate block, having as input the angular speed and the assumed static and dynamic imbalance, was designed to simulate the imbalance forces. The simulation results will be presented in the next section.

## 4.2 Closed Loop Control Evaluation

In this section, the simulation results for the pole placement controller with the closed loop poles given in Table 3.1 and the state observer poles given in Table 3.2 are presented. Equivalent results, which are not presented here, were obtained for LQG control. Although the CBM was successfully controlled by MPC in simulation, the results are not presented here due to their limited practical relevance (see Section 3.4).

The axial or radial position response to a step reference is of minor importance because the reference remains constant. Instead the system response to step disturbances is of greater importance. An initial condition response succeeded by a disturbance rejection for the $y$-axis of the DE at zero speed is presented in Figure 4.2.

It can be observed that about 15 ms are required for the $y_{\mathrm{sDE}}$ to move from the initial position of $-150\,\mu\mathrm{m}$ to its nominal position, while about 25 ms are required for the rejection of a $-2$ N step disturbance. The current is bounded initially at the limitation of 10 A and finally converges to the bias-current of 2.9 A, i.e. the current required to hold the rotor weight. At the time the step disturbance is applied, the current starts to increase until it successfully rejects the disturbance and $y_{\mathrm{sDE}}$ returns to its nominal position.

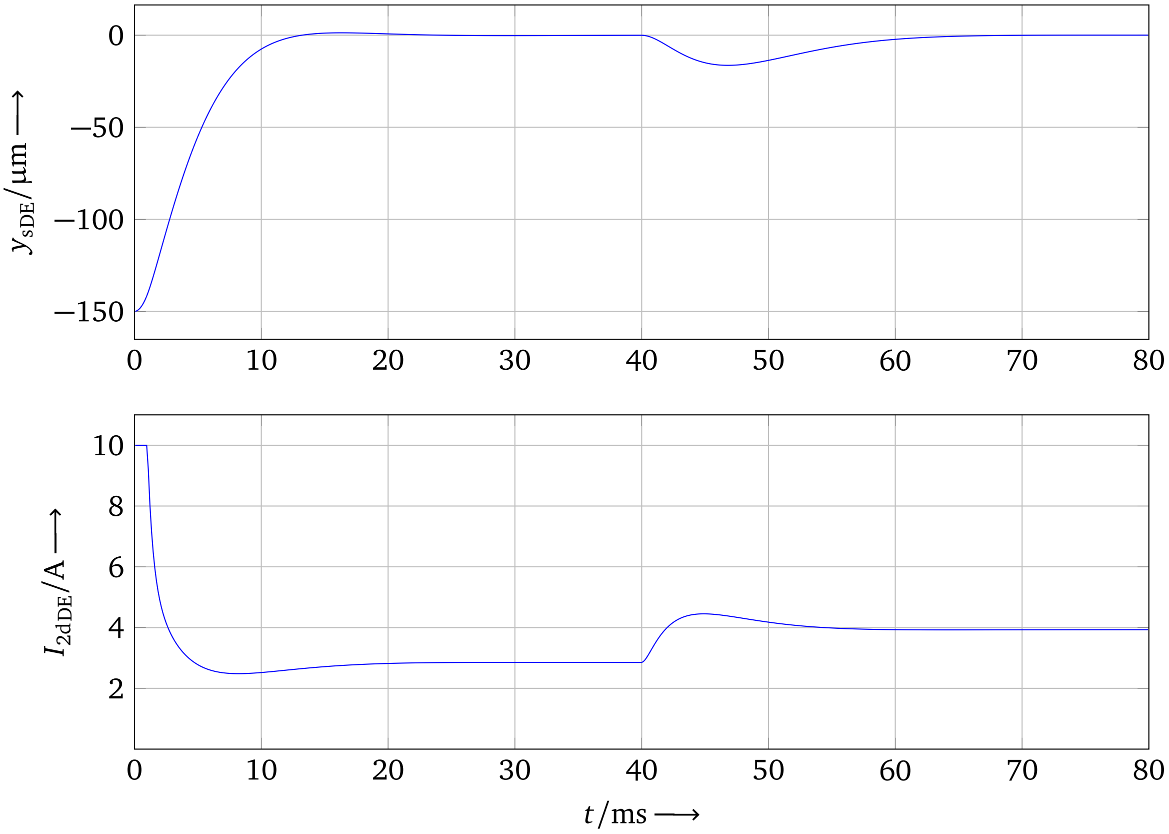

**Figure 4.2.:** Initial condition and disturbance response for $y_{\mathrm{DE}}$ and $I_{2\mathrm{d}_{\mathrm{DE}}}$ at zero speed

Simulation results for IFC and IFR application at certain angular speeds are presented in Figure 4.3 and Figure 4.4 respectively. Both IFC and IFR are triggered at 30 ms. It can be seen in Figure 4.3 that the displacement $x_{\mathrm{sDE}}$ converges to zero after certain time and the corresponding current $I_{2\mathrm{dDE}}$ is decreased.

In Figure 4.4, it can be observed that $I_{2\mathrm{dDE}}$ converges to zero after certain time and the corresponding displacement $x_{\mathrm{sDE}}$ is reduced. Although the synchronous displacement elimination after IFC application was expected, the corresponding current reduction was not. Similarly, the reduction of the synchronous displacement after IFR application was not expected. In Section 5.3, IFC and IFR will be applied to the real CBM and the simulation results presented in Figure 4.3 and Figure 4.4 will be verified. An explanation of the unexpected side effect of current reduction for IFC and orbit reduction for IFR will be also given.

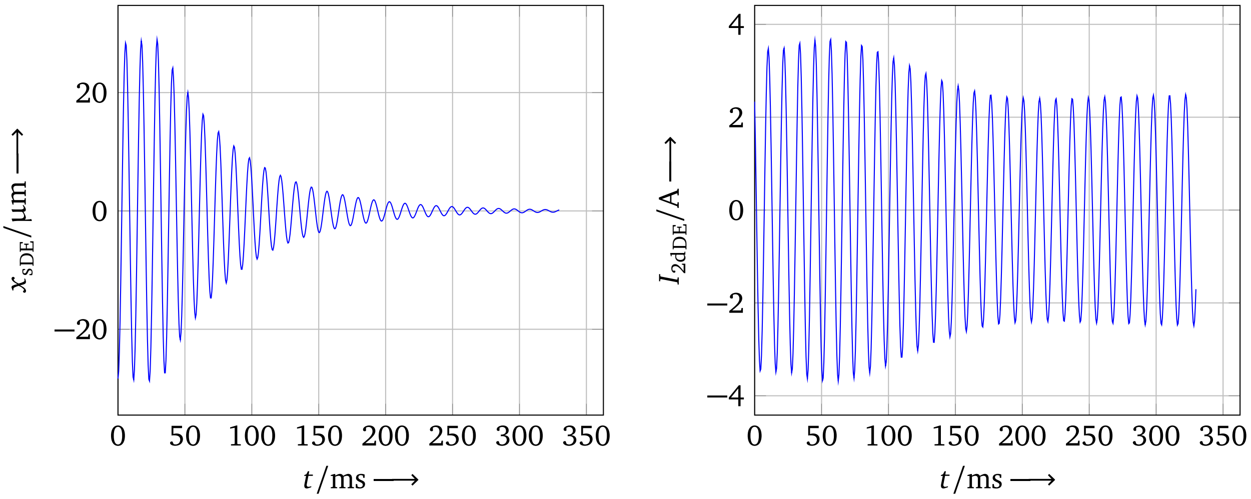

**Figure 4.3.:** Simulated IFC application at 5000 rpm

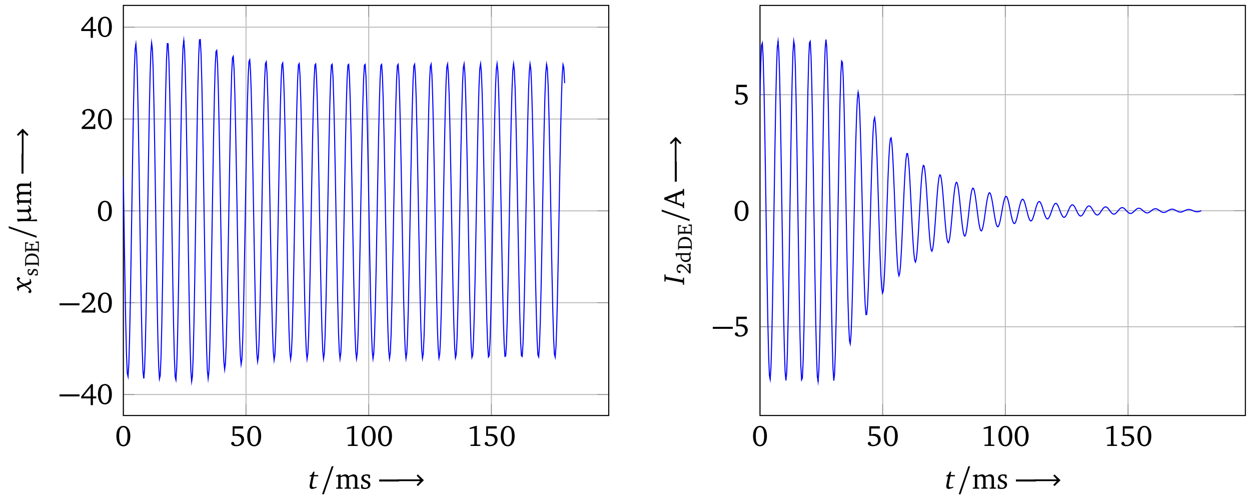

**Figure 4.4.:** Simulated IFR application at 9000 rpm

# 5 Implementation

In order to test the designed control structures in the real CBM, additional hardware and software are needed. For this reason a test bench, which will be subsequently described, was built. First of all, a computer having Linux as operating system is used to run the control applications, from now on *application computer*. A FPGA, which is attached to one of the PCI bus slots of the application computer, is responsible for the signal processing, current control and voltage modulation [4]. The position and speed control run in the processor of the application computer. Since the control of the CBM is a time constrained application, the *Real Time Application Interface* (RTAI) is used. The control algorithm, by means of C-code, is uploaded to the application computer, compiled and executed in the Linux user space. The RTAI ensures that the application runs in real time. In order to handle the control parameters and acquire data during control execution, a second computer is used, from now on *user computer*. The communication between the user and application computer is done via *Local Area Network* (LAN). Control applications can be conveniently designed by means of Simulink block diagrams, then translated into C-code by the Matlab Coder and finally uploaded to the application computer. The Simulink model from which the C-code was generated can be used as a user interface during application execution. That is, parameter handling and data acquisition can be done relatively easy using Simulink. An overview of the control process is given in Figure 5.1. The signals $\boldsymbol{y}_{\text{ref}}$ and $\boldsymbol{y}_{\text{real}}$ stand for the desired and real rotor mechanical position and speed. The signal $\boldsymbol{i}_{\text{ref}}$ denote the reference currents on $dq$ reference frame, whereas $\boldsymbol{i}_{\text{abc}}$ the measured phase currents. The control signals for the inverter switches are indicated by $v_{\text{sw}}$, whereas the phase voltages by $\boldsymbol{u}_{\text{abc}}$. The position and speed control sampling frequency equals $f_{\text{s}} = 15.625\,\text{kHz}$, the FPGA runs at $f_{\text{FPGA}} = 8f_{\text{s}} = 125\,\text{kHz}$, while the inverter switching frequency equals $f_{\text{sw}} = 4f_{\text{s}} = 62.5\,\text{kHz}$.

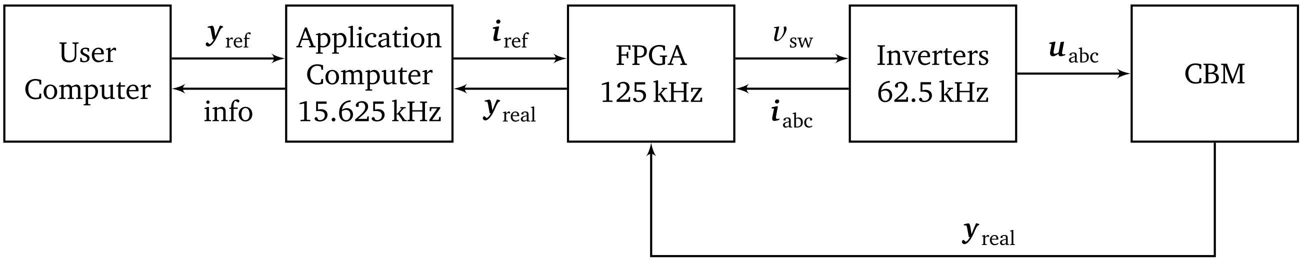

**Figure 5.1.:** Overview of the control process

## 5.1 Feedback Signal Conditioning

The CBM supports five eddy current position sensors for the radial and axial displacements. The absolute rotor angular position is provided by a two-axis Hall sensor. More information about the commissioning of the sensors in the CBM can be found in [3]. A detailed presentation of the working principle of eddy current and Hall sensors can be found in [27]. In order to make the controller less susceptible to noise, all the radial and axial position signals are filtered after the discretization using an *Infinite Impulse Response* (IIR) filter with a cutoff frequency close to 2 kHz. As the designed dynamics of the closed loop are around 50 Hz the extra poles coming from the filter are not further considered.

The rotor angle is not directly the feedback needed for the speed control. A first idea would be to place a discrete time differentiator preceding by a low pass IIR filter to derive the speed. However, as the rotor angle signal is the output of the `atan2` function it lies in the range $(-\pi, \pi]$. This obviously introduces a discontinuity of the angle signal exactly at the time the angle equals $\pi$. Although the angle feedback is discretized, the aforementioned discontinuity would create an unwanted behavior of the differentiator in case the angle passes the value $\pi$ between two subsequent time steps. For this reason an algorithm that observes and compensates the passing through $\pi$ is designed in [4]. However, using this algorithm only speeds up to one fourth of the sampling frequency can be observed (5.1).

$$n_{\max} = 15 f_{\mathrm{s}} \tag{5.1}$$

For the used sampling frequency ($f_{\mathrm{s}} = 15\,625\,\mathrm{Hz}$), the limit is $n_{\max} = 234\,375$ rpm. This corresponds to a speed that is about 13 times higher than the designed nominal speed of the rotor. For noise suppression an IIR filter is added after the differentiator with a cutoff frequency close to 200 Hz. The dynamics of the closed loop speed controller are designed close to 10 Hz. As done for the position signals the extra pole introduced by the speed filtering is not further considered.

## 5.2 Position Sensor Calibration

Although an elaborate calibration method for the position sensors was developed in [28], a simplified approach that produces reliable results in short time is described here. The position sensors should be calibrated after the calibration of the offset angles for the levitation currents [4]. That is, the $d$ and $q$ levitation currents of both conical motors should be able to produce a pure horizontal and vertical force respectively. Then, producing pure horizontal or vertical forces, the rotor is positioned to the most remote position on the $x$ and $y$ axes. Subsequently, the signal values being proportional to the differential voltage of the eddy current sensors are captured. Furthermore, a value corresponding to the excitation voltage of the eddy current sensors is captured. Obtaining the ratio of the differential voltage over the excitation, the measurement becomes independent of the excitation voltage fluctuations. Capturing the maximum $s_{\max}$ and minimum $s_{\min}$ value for each sensor, the displacement range (5.2) and the mid-range (5.3) for each axis can be calculated.

$$R_{\mathrm{s}} = s_{\max} - s_{\min} \tag{5.2}$$

$$M_{\mathrm{s}} = \frac{s_{\min} + s_{\max}}{2} \tag{5.3}$$

Subsequently, using the measured mechanical play, i.e. the difference $d_{\mathrm{a}}$ between the diameters of the auxiliary bearings and the rotor, a gain converting the position sensor signal to µm (5.4) and a zero offset (5.5) are calculated.

$$G_{\mathrm{c}} = \frac{d_{\mathrm{a}}}{R_{\mathrm{s}}} \tag{5.4}$$

$$S_{\mathrm{off}} = M_{\mathrm{s}} G_{\mathrm{c}} \tag{5.5}$$

The $z$-axis position signal was calibrated first and the zero was placed exactly at the mechanical middle. Afterward, the signals on the $x$ and $y$ axes were calibrated, keeping the $z$ position signal zero. The Matlab script `calibration` (Appendix B) was developed for the position sensor calibration. The development of an *auto-calibration* method, so that the mechanical play is the only input needed, would be a useful tool to be developed in a future work.

## 5.3 Control Performance

The designed and simulated pole placement controller was tested successfully on the real motor. The resulting closed loop was stable without performing any tuning action. In case specific requirements for the dynamic response are given, additional tuning can be applied. The Simulink model `cbm_development` was used as an interface to test the designed controllers. An additional Simulink model `cbm_exhibition` with fixed control parameters providing an adequate performance was stored, in order to have a reference control loop for future investigations. In order to evaluate the control performance and verify whether the control characteristics are close to that designed, the system frequency response is captured. The Simulink model `cbm_measurements` was used for the measurements.

The measurement of the system frequency response has several benefits [1]. Firstly, the measurement of the plant transfer function aims to verify the plant model used for the control design. Secondly, the measurement of the closed loop transfer function can justify whether the desired closed loop characteristics are met. Furthermore, having the sensitivity transfer function measured, provides a straightforward way to evaluate the system response to harmonic disturbances. Additionally, the measurement of the sensitivity function opens the way to assess the control robustness against system uncertainties. The frequency response should be measured while the rotor is levitating, by means of a stable closed loop controller as displayed in Figure 5.2. Then the excitation signal $\boldsymbol{r}$ is given as reference and the system response is measured. The corresponding plant $\boldsymbol{G}_\mathrm{p}(s)$, closed loop $\boldsymbol{G}_\mathrm{w}(s)$ and sensitivity $\boldsymbol{G}_\mathrm{s}(s)$ transfer matrices are described by (5.6).

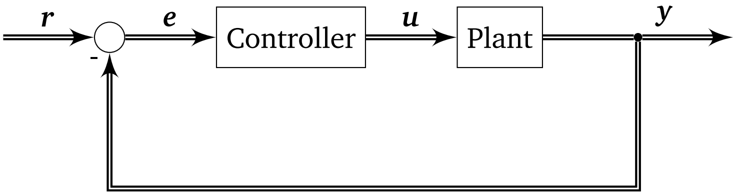

**Figure 5.2.:** Closed loop system for frequency response measurement

$$\boldsymbol{y}(s) = \boldsymbol{G}_\mathrm{p}(s)\boldsymbol{u}(s) \qquad \boldsymbol{u}(s) = \boldsymbol{G}_\mathrm{w}(s)\boldsymbol{e}(s) \qquad \boldsymbol{e}(s) = \boldsymbol{G}_\mathrm{s}(s)\boldsymbol{r}(s) \tag{5.6}$$

The frequency response measurements follow the ISO 14893-3 [29] methodology, as described in [1]. The measurements are performed in a MIMO system, such that of Figure 5.2, but only the diagonal components of the transfer matrices are considered. In order to capture the frequency response of common mode on the $x$-$z$-plane unaffected form the others modes, the excitation $\boldsymbol{r}_\mathrm{Cx}(t)$ is given as reference to the closed loop. Similarly, the excitation $\boldsymbol{r}_\mathrm{Dx}(t)$ is used to excite the differential mode (5.7). The signal $r(t)$ can be freely chosen, e.g. a sine or a square waveform.

$$\boldsymbol{r}_\mathrm{Cx}(t) = \begin{pmatrix} 1 \\ 1 \\ 0 \\ 0 \\ 0 \\ 0 \end{pmatrix} r(t) \qquad \boldsymbol{r}_\mathrm{Dx}(t) = \begin{pmatrix} 1 \\ -1 \\ 0 \\ 0 \\ 0 \\ 0 \end{pmatrix} r(t) \tag{5.7}$$

If the response signals $x_\mathrm{sDE}(t)$, $e_\mathrm{DE}(t)$ and $u_\mathrm{DE}(t)$ are measured, the desired transfer functions can be calculated applying *Fast Fourier Transform* (FFT). If only the common mode on the $x$-$z$-plane is excited and the response is measured, the corresponding plant, closed loop and sensitivity transfer functions are given by (5.8).

$$G_{\mathrm{pCx}}(s)=\frac{x_{\mathrm{sDE}}(s)}{u_{\mathrm{DE}}(s)} \qquad G_{\mathrm{wCx}}(s)=\frac{r(s)}{x_{\mathrm{sDE}}(s)} \qquad G_{\mathrm{sCx}}(s)=\frac{e_{\mathrm{DE}}(s)}{r(s)} \tag{5.8}$$

Equivalently, if only the differential mode on the $x$-$z$-plane is excited and the response is measured, the corresponding plant, closed loop and sensitivity transfer functions are given by (5.9).

$$G_{\mathrm{pDx}}(s)=\frac{x_{\mathrm{sDE}}(s)}{u_{\mathrm{DE}}(s)} \qquad G_{\mathrm{wDx}}(s)=\frac{r(s)}{x_{\mathrm{sDE}}(s)} \qquad G_{\mathrm{sDx}}(s)=\frac{e_{\mathrm{DE}}(s)}{r(s)} \tag{5.9}$$

A chirp signal is a sinusoidal signal with linearly increasing frequency. The chirp signal function with the linearly increasing frequency of (5.10) is given in (5.11), where $f_0$ is the initial frequency, $k$ the rate of frequency increase, $A$ the signal amplitude, and $\varphi_0$ the initial phase. If the signal is applied for a certain time $t_1$, the final frequency would be $f(t_1)=f_0+kt_1$.

$$f(t)=f_0+kt \tag{5.10}$$

$$x(t)=A\sin\left[\varphi_0+2\pi\left(f_0t+\frac{k}{2}t^2\right)\right] \tag{5.11}$$

Chirp signals are injected to obtain the system frequency response. Since the built-in chirp signal source of Matlab was not resettable and thus not appropriate for the measurements, an additional more flexible chirp signal generator is developed (Appendix B). The model `cbm_measurements` is used as an interface to accomplish the measurements and the data are stored in `mat` files (Appendix B). The excitation $r(t)$ and the measured signals $u_{\mathrm{DE}}(t)$ and $y_{\mathrm{DE}}(t)$ are object of FFT. Consequently, the transfer functions of (5.8) can be calculated by an element-wise division of the FFT results. Smoothing algorithms were used to obtain smooth transfer functions plots. The measured frequency responses and the calculated transfer functions for the pole placement with the closed loop eigenvalues given in Table 3.1 are presented in the following graphs.

The measured and calculated common mode plant transfer functions on the $xz$-plane are shown in Figure 5.3. There is an obvious difference of about 6 dB between the measured and calculated dc-gain. The main reason for this discrepancy is presumably the large deviation of the calculated negative stiffness $k_{\mathrm{sr}}$ from the real value. Theoretically the phase shift introduced by the plant should be always $-180°$ due to the unstable pole. However, additional phase delay is introduced due to the underlying current control loop which was neglected in the CBM modeling. Moreover, the time delay introduced by the inverters leads to an exponential decreasing phase with frequency. That is, the plant phase rolls off at higher frequencies. The same behavior will be observed later for the closed loop transfer function. The low value of the plant dc-gain, almost $-90$ dB, comes from the fact that the rotor displacements are in µm range but the plant output is scaled in m. At higher frequencies the measured transfer function converges to the calculated one, i.e. they both expose a decrease rate of 40 dB per decade.

The measured and calculated common mode closed loop transfer functions on the $x$-$z$-plane are presented in Figure 5.4. The closed loop phase should theoretically converge to $-270°$, due to the three stable closed loop poles. However, as already described for the plant transfer function, the closed loop phase rolls off at high frequencies, because of the time delay introduced by the inverters.

The measured and calculated common mode sensitivity function on the $x$-$z$-plane is presented in Figure 5.4. The peak of the sensitivity function is about 3.75 dB, which is considered adequate with respect to the control robustness. Another peak of the sensitivity function is expected at the first rotor *bending mode* but the motor is not designed to reach this speed (about 60 000 rpm). The same procedure was followed for the differential mode on the $x$-$z$-plane, the corresponding plots are attached in Appendix C.

In order to visualize the results of IFC and IFR application on the real system, the transients after IFC at 4000 rpm and IFR at 6000 rpm are presented in Figure 5.6 and Figure 5.7 respectively. The signals

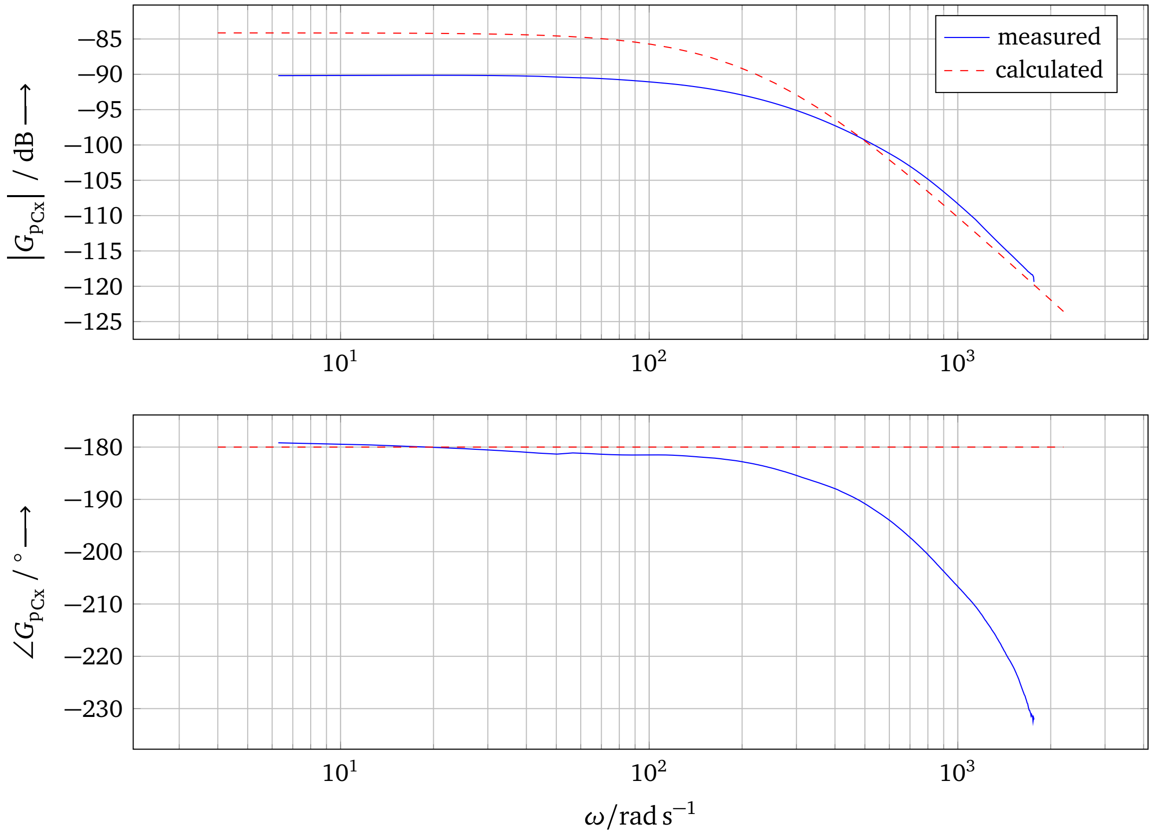

**Figure 5.3.:** Common mode plant frequency response on the $x$-$z$-plane $G_{\mathrm{P_{Cx}}}(j\omega)$

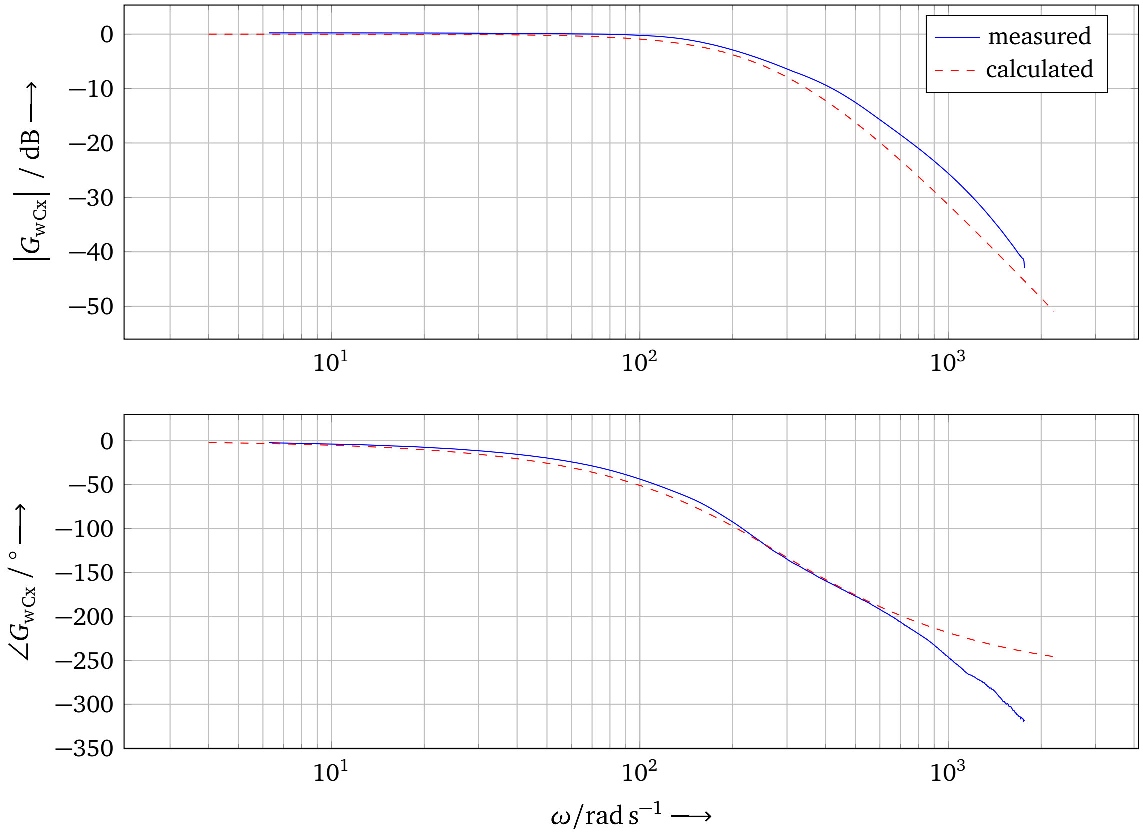

**Figure 5.4.:** Common mode closed loop frequency response on the $x$-$z$-plane $G_{\mathrm{wCx}}(j\omega)$

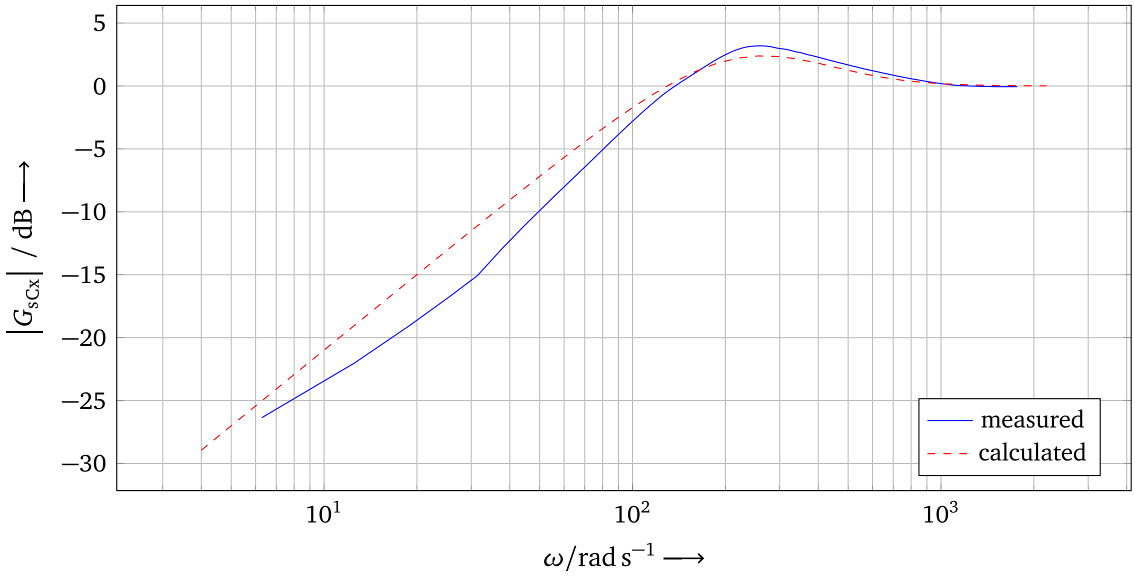

**Figure 5.5.:** Common mode sensitivity frequency response on the $x$-$z$-plane $G_{\mathrm{sCx}}(j\omega)$

presented in Figure 5.6 are the displacement $x_{\mathrm{sDE}}$ as measured at the sensor plane and the corresponding levitation current $I_{2\mathrm{dDE}}$ as measured at the IFC output (see Figure 4.1). The IFC is triggered at 64 ms; it can be observed that the rotor orbits vanish about 300 ms or 20 periods after the triggering. The convergence time is controllable by the gain $k_{\mathrm{e}}$, which was introduced in Section 3.5. As soon as the system converges, the rotor orbits are at the range of 1 µm and they contain mainly higher order harmonics. That is, the synchronous component caused by the imbalance forces is compensated. An interesting result, which is not so intuitive at first glance, is the reduction of the current amplitude. Someone would expect that more current is required to compensate the imbalance forces so that the rotor is forced to rotate around a fixed axis. This is true, but the effect of the *negative stiffness* should be also taken into account. In normal operation without IFC, the controller itself cannot fully compensate the imbalance forces and the rotor is displaced from its nominal axis. Then, additional forces due to the negative stiffness having the same direction as the rotor displacement act on the rotor. The controller tries to compensate for both forces, but the generated control current lags in phase. After IFC application the rotor orbits vanish and so do the forces due to the negative stiffness. The latter leads to the current amplitude reduction. The current amplitude which was initially 5 A is reduced to 3 A after IFC application.

The IFR application at 6000 rpm is presented in Figure 5.7. The IFR is triggered at 32 ms; it can be observed that the levitation current converges to an average of about −0.6 A about 300 ms or 30 periods after the triggering. It is also observed that the synchronous current component vanish completely and only higher harmonics remain. An interesting result is the reduction of the rotor orbits. Someone would expect that the orbits increase because the control makes no effort to compensate the imbalance forces. However, whether the orbits become smaller or larger after IFR application depends on the closed loop *sensitivity function* $G_{\mathrm{s}}(j\omega)$. The disturbance attenuation due to a feedback controller with respect to the open loop response is analyzed in [30]; disturbances with frequencies $\omega$ such that $|G_{\mathrm{s}}(j\omega)| > 1$ are amplified by a feedback controller, whereas disturbances with frequencies such that $|G_{\mathrm{s}}(j\omega)| < 1$ are attenuated. The lowest frequency at which the sensitivity function equals unity is called *sensitivity crossover frequency* $\omega_{\mathrm{sc}}$. In case of IFR application, a synchronous notch filter is active on the feedback loop (see Figure 4.1), which eliminates the synchronous feedback component. Therefore, the influence of the synchronous disturbances on the feedback loop is also eliminated and the controller does not react at all to synchronous disturbances. In other words, the closed loop system response to synchronous disturbances will be identical with the plant (open loop) response. Considering the connection between the sensitivity crossover frequency and disturbance attenuation, it follows that the rotor orbits will be increased after IFR application if the motor is driven below $\omega_{sc}$ and decreased at higher speeds.

This phenomenon is also described in [1] but it is connected with the rigid body resonance band; applying IFR at speeds inside the resonance band eliminates the control effort at the synchronous speed and consequently suppresses the resonance. However, if the damping is high enough, no resonance band will exist, which is actually the case for the designed controller (see Figure 5.4). For this reason the phenomenon can be better explained by the sensitivity function, which is directly connected with disturbance attenuation. It is evident that the magnitude of the sensitivity function is higher than unity near resonances, though, the sensitivity function can be higher than unity even if the closed loop has no resonance band. The sensitivity crossover frequency read in Figure 5.5 is about 138 rad/s, which corresponds to 1320 rpm. Hence, orbit reduction is expected applying IFR at speeds higher than 1320 rpm. The measurements of Figure 5.7 confirm the theoretical investigation; after IFR application at 6000 rpm the rotor orbits are decreased form 50 μm to 30 μm.

The rotor orbits and the corresponding levitation currents at 18 000 rpm are presented in Figure 5.8 and Figure 5.9. The measurements are done under IFR; otherwise, there is no chance to drive the motor to 18 000 rpm without leading the actuator to its limits. Orbits of about 25 μm are observed on the DE, while orbits of about 12 μm are registered on the NDE. The orbits are close to circular, i.e. the phase difference between the displacements on $x$ and $y$ axes is about 90° and their amplitudes are about equal. Furthermore, there is a phase shift between the DE and NDE orbits, which exposes the presence of dynamic imbalance.

The levitation currents of the DE (Figure 5.9) are near to the expected ones; the average $I_{2\mathrm{dDE}}$ current is about zero, wheres the average $I_{2\mathrm{q_{DE}}}$ current is close to 2.5 A, as it should be to compensate for the rotor load (2.9 A was calculated in Section 2.3). The levitation currents for the NDE are less anticipated; the average $I_{2\mathrm{dNDE}}$ is close to 1 A and the the average $I_{2\mathrm{q_{NDE}}}$ is about 3 A but unexpectedly noisy. Considering that the position sensor calibration is reliable, the reason for the non-zero average of $I_{2\mathrm{dNDE}}$ is probably a misalignment of the stator and auxiliary bearing centers causing a non-rotating single sided magnetic pull. The reason for the higher $I_{2\mathrm{q_{NDE}}}$ average is that the rotor center of mass is shifted towards the NDE due to the attachment of the axial position sensor measurement surface. The noisy $I_{2\mathrm{q_{NDE}}}$ current can be explained in conjunction with the noisy $y_{\mathrm{sNDE}}$ signal, which can be observed in Figure 5.8. The reason for the noisy $y_{\mathrm{sNDE}}$ signal is presumably a bad placement of the NDE position sensor mounting plate.

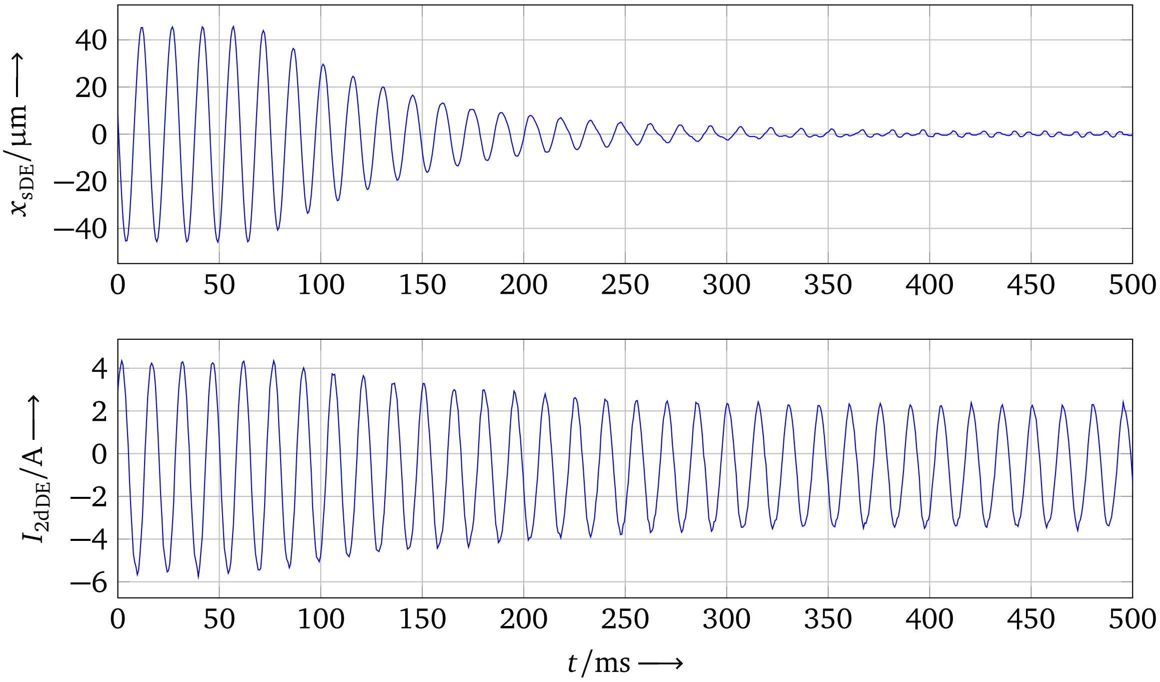

**Figure 5.6.:** Application of IFC at 4000 rpm: **Top**: position synchronous component vanishes; **Bottom**: levitation current synchronous component decreases

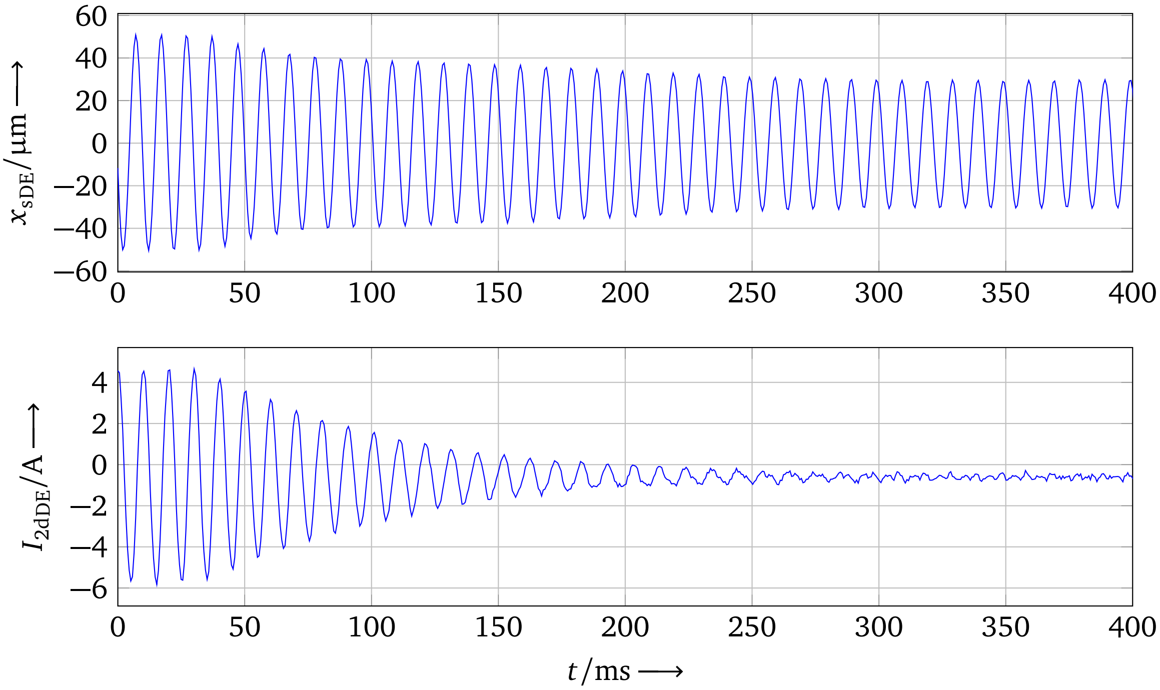

**Figure 5.7.:** Application of IFR at 6000 rpm: **Top**: position synchronous component decreases; **Bottom**: levitation current synchronous component vanishes

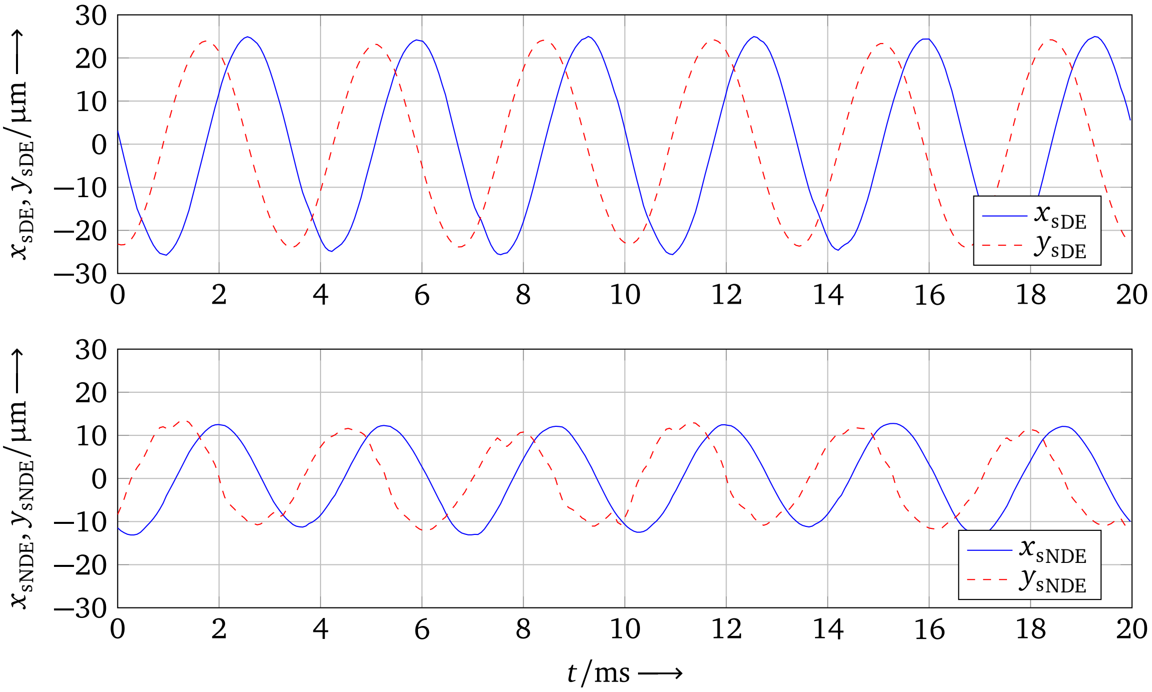

**Figure 5.8.:** Measured rotor orbits at 18000 rpm under IFR: **Top**: horizontal and vertical displacement at DE; **Bottom**: horizontal and vertical displacement at NDE

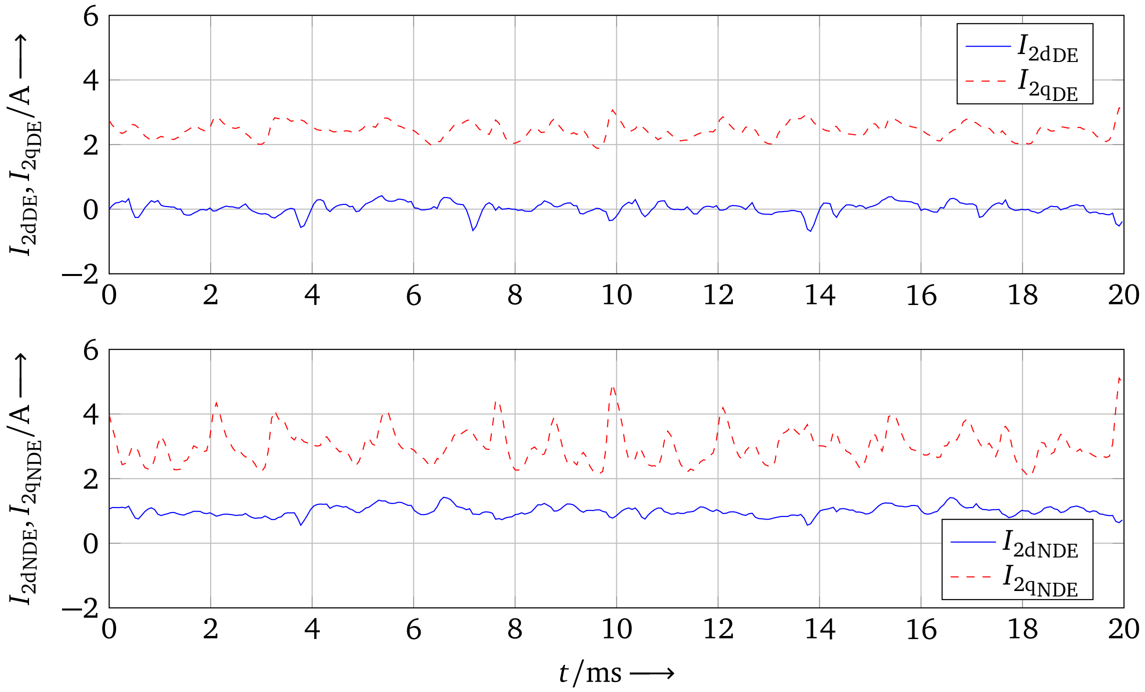

**Figure 5.9.:** Measured levitation currents at 18000 rpm under IFR: **Top**: levitation currents for the DE; **Bottom**: levitation currents for the NDE with increased $I_{2\mathrm{q}_{\mathrm{NDE}}}$ effort due to the noisy position sensor feedback $y_{\mathrm{sNDE}}$

# 6 Conclusion

The accomplishments of this work are summarized in this chapter. A short comparison with control approaches used in previous works is also done. At last, advices for future work in the control design and testing of the CBM are given.

## 6.1 Accomplishments

The scope of this work is the design of modern control approaches for drive and suspension of the double conical bearingless motor. The first step before the control design is the derivation of an adequate motor mathematical model. For this reason, after reasonable assumptions for the magnetic field distribution, the air gap flux density is analytically calculated. Using the derived air gap flux density and the Maxwell stress tensor, the forces acting on the rotor are analytically calculated. For the forces that are controllable by Field Oriented Control, the corresponding force-current coefficients are calculated. In this context, a force-displacement coefficient, the so-called axial negative stiffness, which constitutes a specific property of the double conical bearingless motor, is calculated. An elaborate model of the magnetically levitated rotor is presented in this work. In contrast to the simplified models used in previous works [3, 4, 28], the new model considers the non-collocation of position sensors and levitation windings and takes into account the presence of angular motion. The differential equations of motion are transformed into a state space representation, which enables the use of modern control approaches.

Three different control approaches are designed and simulated. The first approach comprises a state controller augmented with integral action, with which the closed loop dynamics are freely defined after pole placement. The Full Modal Synthesis method is used to place the poles and decouple the dynamics of the angular and translational motion. In order to obtain a full state feedback, a reduced order state observer is designed. The Linear Quadratic Gaussian control is the object of the second approach; a Linear Quadratic Regulator augmented with integral action and a Kalman-filter are designed to implement LQG control. Finally, a Model Predictive Control approach is designed, which however lacks of practical relevance, due to the relatively low sampling period used for the control of the CBM.

The control algorithm based on pole placement was uploaded to the application computer, by means of C-code, and tested on the real CBM motor successfully. However, the motor could not overcome the limit of 10 000 rpm because of the inverter current limitation. Sinusoidal disturbance forces with the rotational frequency were identified as the cause of the increased control effort. The reason for the synchronous disturbance forces is mainly the rotor mass imbalance. The Imbalance Force Rejection strategy was designed to reject the control action against the synchronous disturbance forces, providing levitation currents free from synchronous components. Consequently, the motor could be driven at higher speeds, since the current limitation problem is solved. Speeds up to 18 000 rpm have been reached with rotor-2. Higher speeds were not tried because at 18 000 rpm the motor back-EMFs were already close to the maximum phase voltage the inverters could supply.

A second problematic for the CBM operation was that the rotor orbits were relatively high already at low speeds. This would not be acceptable in precision applications. For this reason the Imbalance Force Compensation strategy was designed. The IFC control strategy compensates for the synchronous disturbance forces, eliminating the synchronous component from the rotor orbits. Using IFC, the rotor displacement from the nominal position was diminished to less than 1 $\mu$m. Additionally, the synchronous vibrations of the stator frame vanish, providing an almost silent motor operation. However, the limit of 10 000 rpm could not be exceeded with IFC due to the inverter current limitation.

An interesting side effect of Imbalance Force Rejection application at relative high speeds is that not only the current synchronous component is eliminated, but also the rotor orbits are decreased. Similarly, after IFC application not only the rotor orbits are reduced, but also the levitation currents are decreased. These side effects are in accordance with theory and were explained in Section 5.3.

Although similar filters were used to drive the rotor at high speed or reduce the rotor orbits in [3], the filter design was hidden and the implementation was proprietary. In other words, those filters could be used only in conjunction with the corresponding commercial inverter.

An interesting result coming from the control implementation is that the synchronous filtering is critical to levitate the rotor at high speed, since the controller can not do much at such high frequencies. Even a rotor with major construction deficiencies, as rotor-2, can be driven under high precision at low speed (using IFC) and with low power losses at high speed (using IFR). These control strategies can save commissioning cost, since less effort could be given in rotor balancing. Furthermore, both filters and especially IFR reduce the current peaks and therefore decrease the inverter ratings.

The frequency response measurement of a bearingless motor is a powerful tool to evaluate the closed loop system behavior. The measurement of the sensitivity function provides a straightforward way to evaluate the system response to harmonic disturbances. The importance of the frequency response is clarified, considering that a synchronous disturbance force is always present in rotating machinery. Separate equipment is not required to apply forced vibrations to the bearingless rotor, since the levitation windings can accomplish this task. The system response is measured by the already available position sensors. In this work, the measurement handling and data acquisition is done by use of Matlab Simulink and FFT is applied later to obtain the frequency response plots.

In order to calculate the CBM model parameters and design the different controllers, several Matlab functions were developed. The functions related to the control design have a wider application area and can be used in future works. Furthermore, Simulink models were designed to simulate the CBM operation as well as to operate the real motor in conjunction with Real Time Application Interface. All files related to Matlab-Simulink are listed in Appendix B.

## 6.2 Future Work

Several additional investigations can be made on the CBMs control design. In this work, no mention of control robustness was made, except for the measurement of the sensitivity peak. However, the control robustness against uncertainties is a very important issue for industrial applications. Control approaches with a direct connection to robustness like $H_\infty$ and $\mu$-synthesis can be also tried to the CBM.

The pole placement control approach and the IFR and IFC filters were successfully implemented with rotor-2, whose significant construction deficiencies cause increased synchronous disturbance forces that require advanced and accurate control. It would be interesting to try the same control strategies on rotor-1 and compare the results.

In this work, the motor operation under different loading conditions was not investigated. In contrast to AMBs, the coupling of driving and levitation fields in bearingless motors generates additional radial disturbance forces. The latter is shown by analytical calculations in Section 2.2. However, at low torques the coupling effect is less severe, since the torque generating current $I_{1q}$ is low. Consequently, the motor should be loaded with higher torques to investigate the coupling effect.

The effect of radial loading at the rotor DE would be interesting for future investigations. The latter has practical relevance because in real applications accessories are mounted on the rotor DE and radial forces may be applied there. In order to obtain quantitative results from this investigation, a controllable load is needed. Ideally a magnetic bearing could be mounted on the rotor DE to apply specific radial load profiles.

# A Motor Parameters

**Table A.1.:** Stator parameters

| **Parameter** | **Symbol** | **Value** | **Unit** |
|---|---|---|---|
| Stator cone angle | $\gamma_\mathrm{s}$ | 10 | deg |
| Stator slot count | $Q_\mathrm{s}$ | 12 | |
| Stator iron length | $l_\mathrm{Fe}$ | 40 | mm |
| Minimum stator bore diameter | $d_\mathrm{simin}$ | 32 | mm |
| Stator outer diameter | $d_\mathrm{so}$ | 95 | mm |
| Mechanical air gap length | $\delta_0$ | 1 | mm |

**Table A.2.:** Levitation and driving winding parameters

| **Parameter** | **Symbol** | **Value** | |
|---|---|---|---|
| | | Driving winding | Levitation winding |
| Number of phases | $m$ | 3 | 3 |
| Pole pair count | $p$ | 1 | 2 |
| Number of slots per pole and phase | $q$ | 2 | 1 |
| Number of winding turns per phase | $n_\mathrm{s}$ | 30 | 20 |
| Number of winding parallel branches | $\alpha_\mathrm{a}$ | 1 | 1 |
| Parallel strands per turn | $\alpha_\mathrm{i}$ | 4 | 3 |

**Table A.3.:** Rotor parameters

| **Parameter** | **Symbol** | **Value** | | **Unit** |
|---|---|---|---|---|
| | | Rotor-1 | Rotor-2 | |
| Permanent magnet cone angle | $\gamma_{\mathrm{r}_\mathrm{PM}}$ | 10 | 10 | deg |
| Back iron cone angle | $\gamma_{\mathrm{r}_\mathrm{Fe}}$ | 10 | 0 | deg |
| Minimum rotor back iron diameter | $d_\mathrm{romin}$ | 20 | | mm |
| Minimum magnet height | $h_\mathrm{Mmin}$ | 3 | | mm |
| Carbon fiber bandage height | $h_\mathrm{B}$ | 2 | | mm |
| Rotor total length | $l_\mathrm{r}$ | 310 | | mm |
| Rotor mass (measured) | $m_\mathrm{r}$ | 1.12 | 1.079 | kg |
| Polar moment of inertia (Ansys) | $J_z$ | 141.22 | 139.2 | $\mathrm{kgmm}^2$ |
| Transverse moment of inertia (Ansys) | $J_x, J_y$ | 4657.12 | 4279.5 | $\mathrm{kgmm}^2$ |
| PM Remanence flux density at 20 °C | $B_\mathrm{R20}$ | 1.117 | | T |
| PM Remanence flux density at 150 °C | $B_\mathrm{R150}$ | 1.024 | | T |
| Coercive field strength at 20 °C | $H_\mathrm{CB20}$ | 919 | | kA/m |
| Coercive field strength at 150 °C | $H_\mathrm{CB150}$ | 764 | | kA/m |

# B Matlab files

## B.1 Developed Matlab Functions

CALCMOT conical bearingless motor coefficients.

k = calcmot(filename) computes a struct k containing important coefficients of the conical bearingless motor using the motor design parameters specified in filename.

SSMOT state space conical bearingless motor model.

sys = ssmot(filename) returns a state space model sys for the conical bearingless motor using the motor design parameters specified in filename and the function calcmot.

PREFILTER feedforward matrices.

[F, Fx, Fu] = prefilter(sys, K) returns a prefilter matrix F, a state feedforward matrix Fx and an input feedforward matrix Fu, for a LTI system sys with a state feedback matrix K. The system sys can be continuous or discrete, but it must not contain any feedthrough. The system sys must have the same number of inputs-outputs.

FMS pole placement with full modal synthesis.

[K, V] = fms(A, B, e, P) calculates a state-feedback matrix K such that the eigenvalues of A-BK are those specified in the vector e. The columns of the matrix P are parameter vectors and the columns of matrix V are the eigenvectors of A-BK. The parameter vectors of matrix P influence the directions of the eigenvectors of matrix V. If A and B describe a discrete system the eigenvalue vector e should be mapped to the z-plane.

DECFMS decoupling with full modal synthesis.

[K, P, V] = decfms(sys, e) calculates a state feedback matrix K for the plant sys such that the inputs-outputs of the closed loop system are decoupled. The desired closed loop eigenvalues are given in the cell array e. Each cell of e contains the desired eigenvalues for each input-output in increasing order. The pole placement is done by the function fms. The resulting parameter vector matrix P and the eigenvector matrix V are also provided as output.

REDOBSV reduced order state observer.

[estim, L] = redobsv(sys, e, P) calculates a discrete or continuous reduced order state observer estim for the discrete or continuous plant sys using the eigenvalue vector e and the parameter vector matrix P. The fms function is used for the pole placement. The output estim and the input sys are LTI systems. The observer gain matrix L is also provided as output.

## B.2 Matlab Scripts

motor1

The design parameters of the double conical motor equipped with rotor-1 are defined and saved to the file mot1.mat.

motor2

The design parameters of the double conical motor equipped with rotor-2 are defined and saved to the file mot2.mat.

current_loop

The inverter and current loop parameters are defined and saved to the file curlp.mat.

calibration

The measured minimum and maximum of the eddy current position sensor signals, the sensor excitation signal as well as the diameters of the auxiliary bearings in um are given as inputs. Subsequently, a coefficient Gconv, which converts the eddy current position sensor signals in um, and a zero offset Soff are computed and saved in the file calib.mat.

## B.3 Simulink Models

cbm_control

Control structure of the conical bearingless motor used for the Linear Quadratic Gaussian and pole placement control design. Different controllers, observers as well as imbalance force compensation and rejection strategies can be simulated. Sinusoidal and step disturbances as well as noise can be applied to the motor model.

cbm_mpc

Control structure of the conical bearingless motor used for the Model Predictive Control.

cbm_development

Control structure of the conical bearingless motor used to test the controllers on the real plant.

cbm_measurements

Control structure of the conical bearingless motor used for data acquisition including frequency response measurements.

cbm_exhibition

Reference control structure of the conical bearingless motor providing adequate control performance.

synchronous_filtering

Simulation of the modulation block used for the synchronous filtering.

chirp_gen

Resettable chirp signal generator block.

## B.4 Measurement Data Files

ParX System response under common mode chirp signal excitation on the x-z-plane.

ConX System response under differential mode chirp signal excitation on the x-z-plane.

IFC_4000 System response under imbalance force compensation application at 4000 rpm.

IFR_6000 System response under imbalance force rejection application at 4000 rpm.

orbits_18000 Rotor orbits and levitation currents at 18000 rpm.

# C Additional measurements

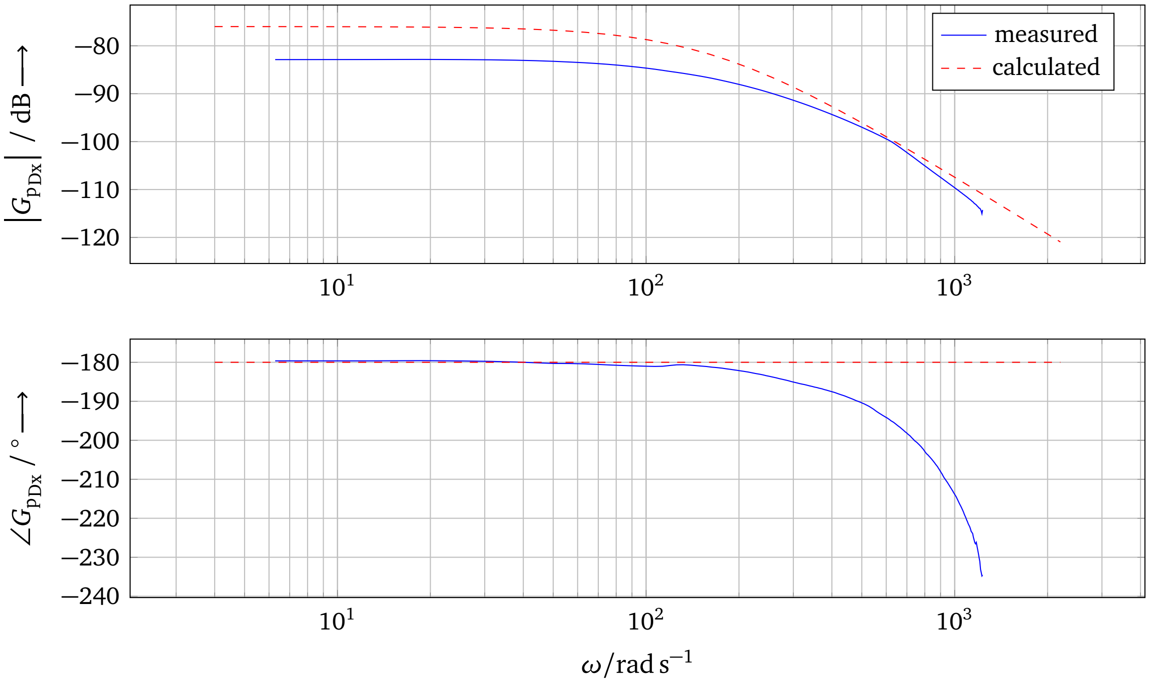

**Figure C.1.:** Differential mode plant frequency response on the $x$-$z$-plane $G_{\mathrm{PDx}}(j\omega)$

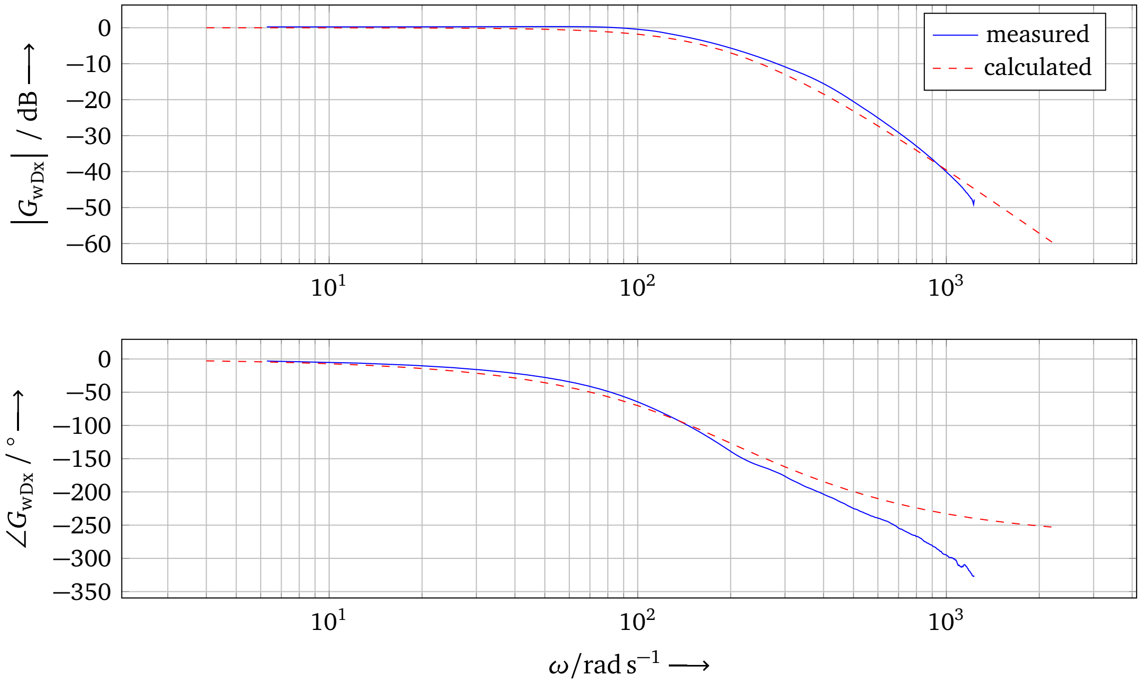

**Figure C.2.:** Differential mode closed loop frequency response on the $x$-$z$-plane $G_{\mathrm{wDx}}(j\omega)$

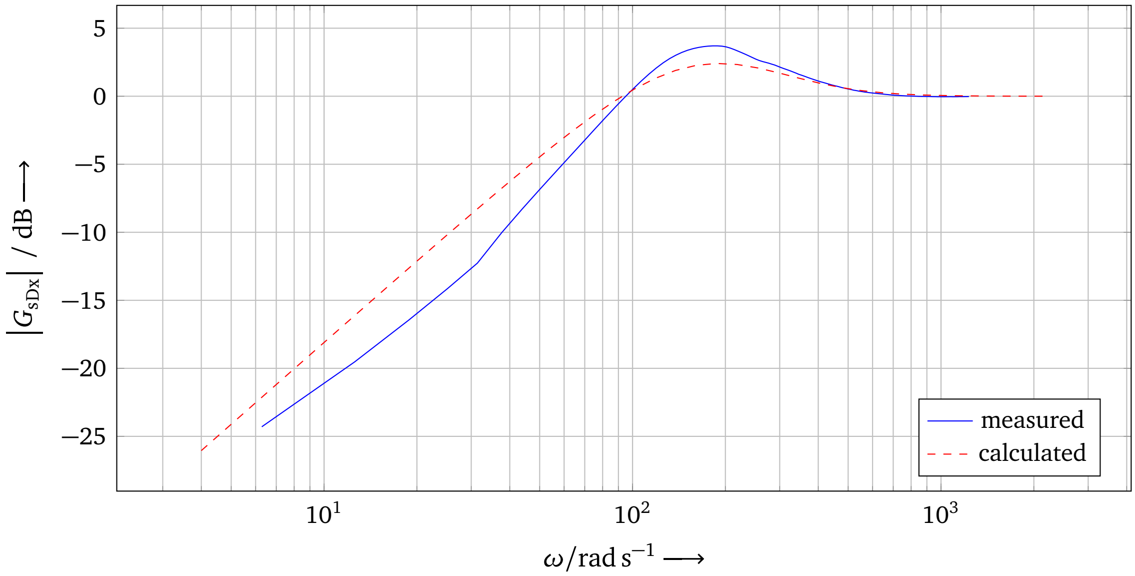

**Figure C.3.:** Differential mode sensitivity frequency response on the $x$-$z$-plane $G_{\mathrm{sDx}}(j\omega)$

# Bibliography

[1] G. Schweitzer, E. H. Maslen *et al.*, *Magnetic bearings: Theory, design, and application to rotating machinery*. Berlin Heidelberg: Springer, 2009.

[2] A. Chiba, T. Fukao, O. Ichikawa, M. Oshima, M. Takemoto, and D. G. Dorrell, *Magnetic bearings and bearingless drives*. Oxford: Elsevier, 2005.

[3] G. Munteanu, "Five-Axis Rotor Magnetic Suspension with Bearingless PM Motor Levitation Systems", Ph.D. Dissertation, Institut für Elektrische Energiewandlung, TU Darmstadt, 2013.

[4] P. Kappes, "Control Design and Implementation of a Double Conical Bearingless PMSM on a Real-time System", Master's Thesis, Institut für Elektrische Energiewandlung, TU Darmstadt, 2013.

[5] O. Föllinger, *Regelungstechnik*, 11th ed. Berlin Offenbach: VDE, 2013.

[6] G. Roppenecker, *Zeitbereichsentwurf linearer Regelungen: Grundlegende Strukturen und eine allgemeine Methodik ihrer Parametrierung*, ser. Methoden der Regelungs- und Automatisierungstechnik. München: Oldenbourg, 1990.

[7] B. Lohmann, *Vollständige und teilweise Führungsentkopplung im Zustandsraum*, ser. Fortschritt-Berichte VDI, Reihe 8: Mess-, Steuerungs- und Regelungstechnik, Nr. 244. Düsseldorf: VDI, 1991.

[8] A. Binder, *Elektrische Maschinen und Antriebe: Grundlagen, Betriebsverhalten*. Berlin Heidelberg: Springer, 2012.

[9] D. J. Griffiths, *Introduction to Electrodynamics*. Upper Saddle River, New Jersey: Prentice Hall, 1999.

[10] F. Irgens, *Continuum Mechanics*. Berlin Heidelberg: Springer, 2008.

[11] T. Schneider, J. Petersen, and A. Binder, "Influence of pole pair combinations on high-speed bearingless permanent magnet motor performance", in *4th IET Conference on Power Electronics, Machines and Drives (PEMD)*, York, England, 2-4 April 2008, pp. 707–711.

[12] G. Müller, K. Vogt, and B. Ponick, *Berechnung elektrischer Maschinen*, 6th ed. Weinheim: Wiley, 2008.

[13] R. Gasch, R. Nordmann, and H. Pfützner, *Rotordynamik*, 2nd ed. Berlin Heidelberg: Springer, 2002.

[14] R. L. Williams and D. A. Lawrence, *Linear State-Space Control Systems*. Hoboken, New Jersey: Wiley, 2007.

[15] E. Hendricks, O. Jannerup, and P. H. Sorensen, *Linear Systems Control: Deterministic and Stochastic Methods*. Berlin Heidelberg: Springer, 2008.

[16] K. Ogata, *Modern Control Engineering*, 5th ed. Upper Saddle River, New Jersey: Prentice Hall, 2009.

[17] J. Lunze, *Regelungstechnik 2: Mehrgrößensysteme, Digitale Regelung*. Berlin Heidelberg: Springer, 2013.

[18] K. J. Aström and B. Wittenmark, *Computer-Controlled Systems: Theory and Design*, 3rd ed. Upper Saddle River, New Jersey: Prentice Hall, 1996.

[19] G. F. Franklin, J. D. Powell, and M. L. Workman, *Digital Control of Dynamic Systems*, 3rd ed. Menlo Park, California: Addison-Wesley, 1997.

[20] P. Dorato, C. Abdallah, and V. Cerone, *Linear Quadratic Control: An Introduction*. Malabar, Florida: Krieger Publishing Company, 2000.

[21] B. D. O. Anderson and J. B. Moore, *Optimal Control: Linear Quadratic Methods*. Englewood Cliffs, New Jersey: Prentice Hall, 1989.

[22] J. Adamy, *Nichtlineare Regelungen*. Berlin Heidelberg: Springer, 2009.

[23] R. Haber, R. Bars, and U. Schmitz, *Predictive Control in Process Engineering*. Weinheim: Wiley, 2011.

[24] E. F. Camacho and C. Bordons, *Model Predictive Control*, 2nd ed., ser. Advanced Textbooks in Control and Signal Processing. London: Springer, 2007.

[25] A. Bemporad, M. Morari, and L. Ricker, *Model Predictive Control Toolbox, User's Guide, R2013b*, Mathworks, Natick, Massachusetts, 2013.

[26] R. Herzog, P. Bühler, C. Gähler, and R. Larsonneur, "Unbalance compensation using generalized notch filters in the multivariable feedback of magnetic bearings", *IEEE Transactions on Control Systems Technology*, vol. 4, no. 5, pp. 580–586, 1996.

[27] J. Fraden, *Handbook of Modern Sensors: Physics, Designs, and Applications*, 4th ed. New York: Springer, 2010.

[28] Y. C. Devisscher, "Enhancement of the Control of a RTAI Based Conical Bearingless Permanent Magnet Synchronous Motor", Bachelor's Thesis, Institut für Elektrische Energiewandlung, TU Darmstadt, 2013.

[29] ISO 14839-3, *Mechanical vibration, Vibration of rotating machinery equipped with active magnetic bearings, Part 3: Evaluation of stability margin*, International Organization for Standardization, Geneva, Switzerland, 2006.

[30] K. J. Aström and T. Hägglund, *Advanced PID Control*. Research Triangle Park, North Carolina: Instrumentation, Systems, and Automation Society (ISA), 2005.